Development of a technique for measuring atmospheric dry deposition and its application to mineral dust

Submitted in fulfilment of the requirements for the degree of

Doctor rerum naturalium (Dr. rer. nat.)

Dissertation by Andebo Abesha Waza

At the Institute of Applied Geosciences

Department of Materials and Earth Sciences

TU Darmstadt - D17

TECHNISCHE UNIVERSITÄT DARMSTADT

1. Examiner: Professor Dr. Konrad Kandler

2. Examiner: Dr. Sergio Rodriguez

Development of a technique for measuring atmospheric dry deposition and its application to mineral dust

By

Andebo Abesha Waza

At the Institute of Applied Geosciences

Department of Materials and Earth Sciences

Technische Universität Darmstadt

Year of publication in TUprints: 2020

Defense held on: January 23, 2020

Darmstadt 2019

In memory of my father

Abesha Waza

Declaration of Authorship

I, Andebo Abesha Waza, hereby declare that I am the sole author of this Dr. rer. nat, thesis and exclusively under the denoted literature. This Dr. rer. nat. thesis has so far not been used in any exam. Prior to the submission of this dissertation, part of the work has been published as described in the relevant chapter herein.

Darmstadt Andebo Abesha Waza

Curriculum Vitae

Personal Data

Name: Andebo Abesha Waza

Sex: Male

Date of Birth: 27 September 1983

Place of Birth: Arbaminch, Ethiopia

Marital Status: Married

Nationality: Ethiopian

Educational Background

Undergraduate: BSc Degree, Physics, Dilla University (Ethiopia), 2005-2008

Postgraduate: MSc Degree, Environmental science, Wageningen University (Netherlands), 2009-2011

Postgraduate: MSc Degree, Atmosphere-Biosphere studies, University of Eastern Finland, 2013-2014

Terminal Degree: Ph.D. (Dr. rer. nat.), 01.04.2016-23.01.2020

Technical University of Darmstadt

Institute of Applied Geosciences

Aerosol Research Group

Title of the Thesis: Development of a technique for measuring atmospheric dry deposition and its application to mineral dust

Supervisor: Prof. Dr. Konrad Kandler

Contents

List of Figures

List of Tables

List of Abbreviations and Symbols

SEM	Scanning electron microscopy
MWAC	Modified Wilson and Cooke
BSNE	Big Spring Number Eight
PM_{10}	Particulate matter 10 micrometers or less in diameter,
CFD	Computational fluid dynamics
HNLC	High- nitrate low-chlorophyll
CO_2	Carbon dioxide
HNO_3	Nitric acid
HCl	Hydrochloric acid
H_2SO_4	Sulfuric acid
H_2CO_3	Carbonic acid
EDX	Energy Dispersive X-ray
PBL	Planetary Boundary Layer
QLS	Quasi-Laminar Sublayer
UNC	University of North Carolina
FWI	Free wing impactor
OPC	Optical Particle Counter
BSE	Back Scattered Electron
d_g	Projected area diameter
B	Area covered by the particle
S_v	Volumetric shape factor
d_v	Volume-equivalent diameter
d_a	Aerodynamic diameter
S_d	Aerodynamic shape factor
P	Perimeter
A	Projected area of the particle
ρ_p	Particle density
ρ_0	Unit density
C_w	Window correction

d_p	Particle size
k	Complex refractive Index
m	Complex refractive index
n_λ	Real part of complex refractive index
k_λ	Imaginary parts of complex refractive index
λ	Wavelength
C	Concentration
μ	Dynamic viscosity of air
V	Kinematic viscosity
V_{ts}	Terminal settling velocity
V_d	Deposition velocity
u_*	Friction velocity
u	Wind speed
EC	Eddy covariance
LoW	Law of the wall
Re	Reynolds number
X	Distance from the lower plate edge to the center of the sampling stub
E	Collection efficiency
V_{imp}	Impaction velocity
Eff_{in}	Inlet efficiency
Stk	Stokes number
T_i	Turbulent intensity
K	Turbulence kinetic energy
A_d	Deposition area

Development of a technique for measuring atmospheric dry deposition and its application to mineral dust

Andebo Abesha Waza

ABSTRACT

Frequently, passive dry deposition collectors are used to sample atmospheric dust deposition. However, there exists a multitude of different instruments with different, usually not well-characterized sampling efficiencies. As a result, the acquired data might be considerably biased with respect to their size representativity, and as a consequence, also composition. In this study, individual particle analysis by automated scanning electron microscopy coupled with energy-dispersive X-ray was used to characterize different, commonly used passive samplers with respect size-resolved chemical and physical properties of mineral dust aerosol particles. In addition, computational fluid dynamics simulations were conducted to predict the deposition of particles on to different passive samplers and thereby to achieve deposition velocities from a theoretical point of view.

Scanning electron microscopy (SEM) calculated deposition rate measurements made using different passive samplers show a disagreement among the samplers. Modified Wilson and Cooke (MWAC) and Big Spring Number Eight (BSNE) - both horizontal flux samplers - collect considerably more material than Flat plate and the Sigma-2, which are vertical flux samplers. The collection efficiency of MWAC increases for large particles in comparison to Sigma-2 with increasing wind speed, while such an increase is less observed in the case of BSNE. A positive correlation is found between deposition rate and PM_{10} concentration measurements by an optical particle spectrometer. The results indicate that a BSNE and Sigma-2 can be good options for PM_{10} measurement, whereas MWAC and Flat plate samplers are not a suitable choice. A negative correlation was observed in between dust deposition rate and wind speed. Deposition velocities calculated from different classical deposition models do not agree with deposition velocities estimated using computational fluid dynamics simulations (CFD). The deposition velocity estimated from CFD was often higher than the values derived from classical deposition velocity models. Moreover, the modeled deposition velocity ratios between different samplers do not agree with the observations.

Results also show that mineral dust is found to be the dominating mineral particle type during this campaign, comprising of different classes of classes of silicates, quartz-like, calcite-like, dolomite-like and gypsum-like particles. In addition, the analysis clearly indicates that the composition of dust aerosol particles remains largely unaffected by the sampler type.

By using the relative abundance of the particle groups, size-resolved complex refractive index of dust particles is calculated. It is found that average refractive index is mainly wavelength dependent. The calculated real part of refractive index varied in between 1.71 and 1.53 for wavelengths ranging from 370 to 950 nm. Likewise, the imaginary part of refractive index is calculated for iron oxide particles and is varied in between $3.28*10^{-4}$ to $7.11*10^{-5}$ for wavelengths in the range of 250-1640 nm. Additionally, the refractive index values have shown a slight decrease with particle size.

In the study, the potential for buffering of dust aerosol particles on the acid mobilization of iron particles is also analyzed. From analysis, it is found that the buffering potential depends on the environmental conditions and time. Moreover, by analyzing the ratio of sulfate mass to the total mass of dust of individual particles with the particle sizes, the mixing state of sulfate particles in the total dust particles were investigated. The analysis indicates that the finer dust particles were associated with higher content of sulfur, while the coarse dust particles corresponds to lower sulfur contents revealing only fine mode sulfate is internally mixed with mineral dust aerosol particles.

Overall, the results show that passive sampling techniques coupled with an automated single particle analysis could be a good option to assess physical and chemical properties of atmospheric mineral dust particles.

Entwicklung einer Technik zur Messung der atmosphärischen Trockenablagerung und ihre Anwendung auf Mineralstaub

Andebo Abesha Waza

KURZFASSUNG

Um atmosphärische Staubdeposition zu untersuchen, werden häufig passive Sammler verwendet. Von diesen Sammlern gibt es eine Vielzahl unterschiedlicher Instrumente mit unterschiedlichen, in der Regel nicht gut charakterisierten Kollektor-Wirkungsgraden. Als Konsequenz können die erfassten Daten in Bezug auf ihre Größenrepräsentativität und infolgedessen auch die Zusammensetzung erheblich verzerrt sein. In dieser Studie wurden mittels automatisierter Einzelpartikel-Rasterelektronenmikroskopie in Verbindung mit energiedispersiver Röntgenspektroskopie verschiedene häufig verwendete passive Kollektoren hinsichtlich ihrer Effizienz charakterisiert. Hierbei wurden die größenaufgelösten chemischen und physikalischen Eigenschaften von Mineralstaub-Aerosolpartikeln untersucht. Zusätzlich wurden Strömungssimulationen durchgeführt, um die Deposition von Partikeln auf verschiedenen passiven Kollektoren vorherzusagen und damit theoretische Depositionsgeschwindigkeiten zu erhalten.

Die basierend auf diesen Daten berechneten berechneten Messungen der Abscheideraten verschiedener passiver Kollektoren zeigen Unterschiede in den Kollektor-Wirkungsgraden. Der modifizierte Wilson & Cooke (MWAC) und der Big Spring Number Eight (BSNE) Sammler - beides Sammler für horizontalen Fluss - sammeln erheblich mehr Material als der Flat Plate und der Sigma-2, bei denen es sich um Kollektoren für den vertikalen Fluss handelt. Der Wirkungsgrad des MWAC steigt zu großen Partikeln hin an. Beim Sigma-2 zeigt sich eine positive Abhängigkeit zur Windgeschwindigkeit. Beim BSNE zeigen sich kaum Abhängigkeiten von den atmosphärischen Parametern. Messungen eines optischen Partikelspektrometers zeigen eine positive Korrelation zwischen Abscheideraten- und PM10-Konzentrationsmessungen. Die Ergebnisse zeigen, dass BSNE und Sigma-2 gute Optionen für die PM10-Messung sind, während MWAC- und Flat-Plate-Kollektoren eher ungeeignet sind. Eine negative Korrelation wurde zwischen Staubdepositionsrate und Windgeschwindigkeit beobachtet. Depositionsgeschwindigkeiten, die aus verschiedenen klassischen

Depositionssmodellen berechnet wurden, stimmen nicht mit Ablagerungsgeschwindigkeiten überein, die mithilfe von CFD-Simulationen (Computational Fluid Dynamics Simulations) bestimmt wurden. Die durch CFD berechnete Abscheidungsgeschwindigkeit war häufig höher als die aus klassischen Depositionsgeschwindigkeitsmodellen abgeleiteten Werte. Darüber hinaus stimmen die modellierten Abscheidungsgeschwindigkeitsverhältnisse zwischen verschiedenen Probenehmern nicht mit den Beobachtungen überein.

Die Ergebnisse dieser Experimente zeigen auch, dass Mineralstaub, aus verschiedenen Klassen von Silikaten, quarzartigen, calcitartigen, dolomitartigen und gipsartigen Partikeln, in Izana der dominierende mineralische Partikeltyp ist. Darüber hinaus zeigt die Analyse deutlich, dass die Zusammensetzung der gesammelten Staubpartikel vom Kollektor weitgehend unabhängig ist.

Unter Verwendung der relativen Häufigkeit der Partikelgruppen wird der größenaufgelöste komplexe Brechungsindex von Staubpartikeln berechnet. Es zeigt sich, dass der durchschnittliche Brechungsindex hauptsächlich wellenlängenabhängig ist. Der berechnete Realteil des Brechungsindex variierte zwischen 1,71 und 1,53 für Wellenlängen im Bereich von 370 bis 950 nm. Eine vergleichbare, aber deutlich stärker ausgeprägte Abhängigkeit zeigt der Imaginärteil des Brechungsindex, der aus den Eisengehalten abgeschätzt wird, im Bereich von 250-1640 nm (zwischen $3{,}28*10^{-4}$; und $7{,}11*10^{-5}$). Zusätzlich zeigen die Brechungsindexwerte eine leichte Abnahme mit der Partikelgröße.

In dieser Studie wird schließlich auch ein Potenzial für die Pufferung von Staubaerosolpartikeln bei der Säuremobilisierung von Eisen in Partikeln untersucht. Aus der Analyse geht hervor, dass das Potential zur Pufferung von den Umgebungsbedingungen und der Zeit abhängt. Darüber hinaus wurde durch Analyse des Verhältnisses von Sulfatmasse zu Gesamtstaubmasse einzelner Partikel mit den Partikelgrößen der Mischungszustand von Sulfatpartikeln in den Gesamtstaubpartikeln untersucht. Die Analyse zeigt, dass die Feinstaubpartikel einen höheren Schwefelgehalt aufwiesen, während die gröberen Staubpartikeln einen geringeren Schwefelgehalt enthielten, was zeigt, dass nur feinmodiges Sulfat intern mit Mineralstaub-Aerosolpartikeln gemischt ist.

Insgesamt zeigen die Ergebnisse, dass passive Probenahmeverfahren in Verbindung mit einer automatisierten Einzelpartikelanalyse eine gute Möglichkeit zur Beurteilung der physikalischen und chemischen Eigenschaften von atmosphärischen Mineralstaubpartikeln darstellen könnten.

Acknowledgements

The completion of this doctoral dissertation has been one of the most significant academic challenges I have had to face. Without the guidance, support and patience of the following people, it would not have been possible for me to complete this study at all.

First and foremost, my utmost heartfelt gratitude to my PhD supervisor Prof. Dr. Konrad Kandler who accepted me and trusted in me for this great scientific intent to be realized. it was a great honor and pleasure to have the opportunity to work with him. He guided me properly and encouraged me to exercise the scientific attitude freely that gave me the opportunity to develop confidence for independent thinking. Most importantly, throughout this work, no matter how many times I came into his office without any appointment, I cannot remember a single day that he said, "Sorry, I am busy." I am extremely lucky to have him as my supervisor.

I owe sincere and earnest thankfulness to Prof. Dr. Stephan Weinbruch and Prof. Dr. Martin Ebert, you both have encouraged me to finish my work on time. Thank you also for all questions, answers at the work-group seminars.

I would also like to take this opportunity to thank all the staff members of Izana Global Atmospheric Watch Observatory for helping me in maintenance of the sampling equipment. Here, I particularly thank Dr. Sergio Rodríguez (who is also one of the members of my supervisory committee) for his help during my stay at the observatory. I also acknowledge Dr Roger Funk from Leibniz-Centre for Agricultural Landscape Research for providing me some of passive samplers.

I must also thank my colleagues Thomas Dirsch for all his technical support. To Kilian Schneiders, thank you for your help with the field measurements, SEM analysis. I must also thank Dr. Nathalie Benker for her help with the setup of the samplers in Izana. Nathalie, I benefited a lot from your experience in the field work. A special thanks goes to Ms. Astrid Kern, thank you so much for your continued administrative interventions whenever needed. A very special gratitude goes to my colleagues and former colleagues, Dr. Aryasree Sudharaj, Mr. Agnesh Panta, Mr. Johannes Heuser, Ms. Stephanie Rettig, Ms. Michelle Erba, Dr. Mark Scerri, Dr. Anette Worringen, Dr. Stine Eriksen Hammer and Dr. Katharina Schütze. I cherish the time we spent together.

I owe my special thanks to Jan May (also coauthor) for helping me with the CFD part of the work. Jan, you also helped me a lot at times when I was having some trouble with matlab code, many thanks!

My deepest gratitude and appreciation goes to my kids (Leul Andebo, Anasmos Andebo and Eliana Andebo) and my wife Birtukan Tulo, who showed relentless patience and endurance in taking care of the kids and encouraging me to concentrate on my work.

I acknowledge the Deutsche Forschungsgemeinschaft (DFG, German Research Foundation) – 264907654, 264912134, 416816480 (KA 2280) for financial support. Prior to the submission of this dissertation, part of the thesis, in which the author of this thesis is the main author, has been published. I acknowledge support for the Article Processing Charge by the Open Access Publishing Fund of Technische Universität Darmstadt.

Above all, my greatest thanks go to the omnipresent God for giving me strength and determination to complete this study successfully.

1 About the thesis

This is a monograph PhD thesis and is based on one publication, in which the author of this thesis is the main author.

The thesis deals with the development of a technique for measuring atmospheric dry deposition and its application to mineral dust deposition measurement. It consists of two main parts: the methodological part (Chapter 1-8) and the atmospheric measurement part (Chapter 9 and 10).

In the methodological section, individual particle analysis by automated scanning electron microscopy coupled with energy-dispersive X-ray was used to characterize different, commonly used passive samplers with respect to their size-resolved deposition rate and concentration. The study focuses on the microphysical properties, i.e. the aerosol concentration and deposition rates as well as the particle size distributions. In addition, computational fluid dynamics modeling is used in parallel to achieve deposition velocities from a theoretical point of view.

In the measurement section, the results of atmospheric measurements are presented. Also, in this section, the methods for atmospheric measurements are briefly discussed.

Finally, from deposition measurement presented in this thesis, the understanding about collection properties of different deposition and other passive samplers is greatly improved. Moreover, the study has contributed to increasing knowledge about how passive sampling techniques coupled with an automated single particle analysis can be used to assess physical and chemical properties of atmospheric mineral dust particles.

The work presented in this thesis has been conducted at the Institute of Applied Geoscience, Technical University of Darmstadt within the period of April 2016 to January 2020.

2 Introduction

The atmospheric carbon dioxide concentration and, thus, Earth's climate is predominantly controlled by the carbon dioxide exchange between atmosphere and ocean (Falkowski et al., 2000; Krishnamurthy et al., 2009). A study (Hannah, 2014) indicates that approximately 90 Gt of carbon moves back and forth between the atmosphere and the oceans every year. This exchange, the exchange of carbon dioxide between the atmosphere and ocean, is in turn controlled by the bio-productivity in the ocean surface water. Different studies (Bristow et al., 2017; Harrison and Cota, 1991) prove that nutrient supply controls the bio-productivity in the ocean surface. While those close to the continent, nutrients are usually delivered by riverine input (Cotrim da Cunha et al., 2007), the vast majority of ocean areas depends on atmospheric input (Ridgwell, 2002).

Mineral dust aerosol particles refer to a tiny suspended soil-constituting particles which come mainly from arid and dry regions, predominantly from deserts and their margins, and believed to have a global source strength of about 2500 $Tgyr^{-1}$ (Ramachandran, 2015). They form the single largest component of global atmospheric aerosol mass budget, contributing about one third of the total natural aerosol mass annually (Penner et al., 2001). Depending on their size, these particles can be transported over distances of thousands of kilometers (Grousset et al., 2003; Mahowald et al., 2005).

Mineral dust aerosol in the climate system has received considerable scientific attention mainly due to its direct effect on the radiative budget and indirect one on cloud microphysical properties (Arimoto, 2001; Huang et al., 2010). Chemical composition is one of an important parameters in determining the radiative forcing of deposited mineral dust aerosol particles (Axson et al., 2016; Di Biagio et al., 2019). However, still there exists very large uncertainties in the assessment of the dust infrared radiative effect (Balkanski et al., 2007; Bierwirth et al., 2009) and poor knowledge of the dust optical properties is believe that one of the main reasons for the uncertainty (Wang et al., 2006). The presence of iron (Fe) particles in mineral dust aerosol is of wide scientific interest in climate studies mainly because of its radiative impacts (Mahowald et al., 2005). Iron oxides particles are one of a major dust aerosol components that is known to affect the ability of mineral dust particles to absorb sunlight at short wavelengths (Alfaro et al., 2004; Derimian et al., 2008) and therefore play a major role in the overall climate forcing caused by dust mineral dust aerosol particles (Zhang et al., 2015). Mineral dust particles

also play a key part with respect to gas phase chemistry by providing a reaction surface e.g. ozone depletion (Nicolas et al., 2009; Prospero et al., 1995).

Dust aerosol also plays an important role in biogeochemical cycles by supplying important and limiting nutrients to ocean surfaces (Jickells et al., 2005); consequently, dust deposition process can modulate the carbon cycle in between Earth and Atmosphere (Shao et al., 2011a). Regions that have high nutrients concentration are often identified by high concentrations of chlorophyll in surface waters (Mahowald et al, 2005). However, there are still large areas of the world ocean where the concentrations of nutrients are high yet bio productivity (chlorophyll) is found to be low. This region is commonly known as High- nitrate low-chlorophyll (HNLC) areas of the oceans (Boyd et al., 2007), where there is high macro-nutrient (nitrate) concentrations but bioproductivity low are of particular interest for the mineral dust deposition into oceans. Atmospheric mineral deposition is a most important source of micronutrients, especially iron, to this High- nitrate low-chlorophyll (HNLC) areas of the oceans (Barraqueta et al., 2019; Stockdale et al., 2016). Atlantic ocean is one of these high-nitrogen low-chlorophyll (HNLC) areas, where bio-productivity (phytoplankton growth) is believed to be limited by the micronutrient iron (Fe) supply (Fung et al., 2000; Okin et al., 2011; Zahariev et al., 2008). Therefore, deposition of iron to these high-nitrogen low-chlorophyll (HNLC) areas has important associations for the CO_2 budget. This is because, an increase in iron deposition to the surface of oceans could increase productivity and thus decrease of atmospheric carbon dioxide concentration (Mahowald et al., 2005). As a result, recently scientific interest has grown regarding atmospheric deposition of Fe particles to surface ocean (Jeong and Achterberg, 2014). For terrestrial ecosystems, particularly for those nutrient-poor tropical ones, mineral dust particles also serve as an important nutrient source for compounds necessary for plant growth like potassium, calcium and magnesium (Boy and Wilcke, 2008; Swap et al., 1992).

Atmospheric processing of airborne dust aerosol particles by acid gases (e.g., HNO_3, HCl, H_2SO_4, H_2CO_3) play an important role in transforming an insoluble iron particle to soluble forms (Ito and Feng, 2010; Nenes et al., 2011). However, dust aerosol particles could also play a pivotal role in neutralizing the acidic species in atmosphere due to the alkaline buffer ability of carbonate aerosol minerals (e.g., $CaCO_3$) which are commonly found in mineral dust particles (Ito and Feng, 2010). There are some studies (Ingall et al., 2018; Meskhidze et al., 2003; Pósfai et al., 2013) that assume that Ca^{2+} from carbonate aerosol buffers acid gases in atmosphere and thereby restricts iron dissolution. There are also reports that on a single particle

basis, dust particles which are internally mixed with carbonate aerosol minerals would be buffered (Gao and Anderson, 2001).

Finally, exposure to such dust particles, particularly in the lower part of the atmosphere, can be a cause for visibility degradations and other harmful health impacts (Malm et al., 2003; Rodrıguez et al., 2001). To sum up, mineral dust aerosol particles play an important role in Earth's climate, biogeochemistry and human health. The schematic diagram demonstrating the interactions between mineral dust aerosol, biogeochemistry and climate is shown in Figure 1.

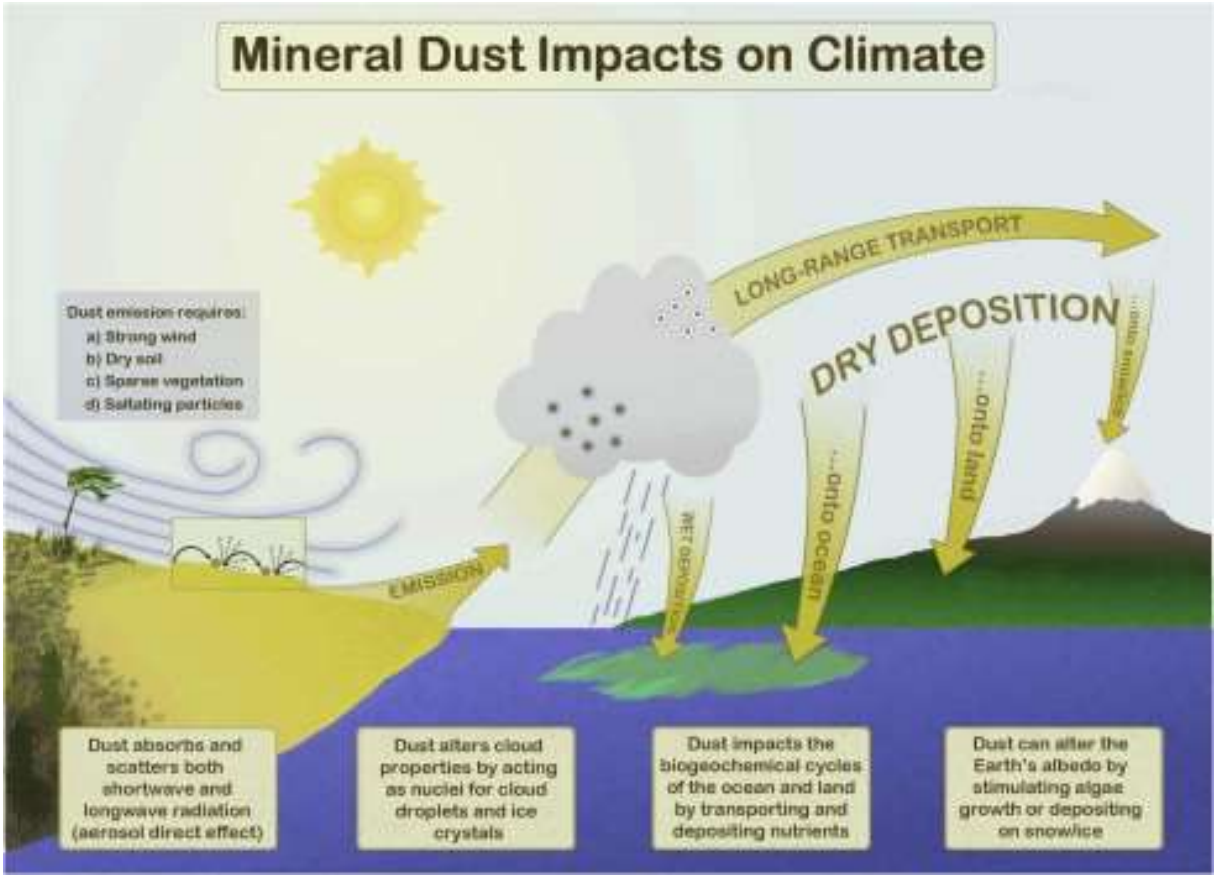

Figure 1*:* Schematic diagram showing interactions between mineral dust aerosol, biogeochemistry and climate, taken from Mahowald et al. (2014).

Deposition measurement data of mineral dust are useful to validate numerical simulation models and to improve our understanding of deposition processes. However, long-term observations of deposition rates measurements of mineral dust particles to the ocean are limited in number (Mahowald et al., 2005). The scarcity and the limited representativity of the deposition measurement data for validation pose a major challenge to assess dust deposition at regional and global scales (Schulz et al., 2012; WMO, 2011). This is in part linked to the uncertainties evolving from the use of different and non-standardized measurement techniques.

In most cases, the physical and chemical properties of mineral dust particles were studied on the basis of bulk samples (Schütz and Sebert, 1987; Stuut et al., 2005). However, dust aerosol includes widespread individual particles with different physical and chemical properties. Furthermore, Dall'Osto et al. (2010) also suggested that performing bulk chemical analysis is not sufficient to fully understand different aerosol properties including transport and transformations, and sources characterization. As a consequence, quantification of global impacts of aerosol particles requires information on single particle properties in the atmosphere. In this perspective the characterization of mineral dusts by in single particle analysis combining scanning electron microscopy (SEM) provides simultaneous information on several particle properties such as article size distribution, composition and estimated density, particle shape and internal mixing state on single particle level and therefore, the approach becomes an important tool to get size resolved information (Chou et al., 2008; Kandler et al., 2007; Kandler et al., 2011). Moreover, by using automation procedures, it is possible to study a large of numbers of single particles with high statistical significance (Kandler et al., 2007).

The thesis primarily describes the work in instrument development and dry deposition measurements. The measurements were carried out in Tenerife (Canary Islands) at Izaña Global Atmospheric Watch observatory (Bergamaschi et al., 2000; Rodríguez et al., 2015) (28.3085ºN, 16.4995ºW) from July to August 2017. The main objective of this study is to assess the particle collection properties of different deposition and other passive samplers based on single particle measurements and their agreement with theory. From the available data, also relations of the collected particle microphysics and chemical composition i.e. the aerosol concentration and deposition rates, optical properties as well as the particle size distributions and composition homogeneity between the samplers will be presented, which can be used as estimators for the comparability of previous literature data based on the different techniques. Elements of high optical and biogeochemical importance (e.g., iron and Ca particles) are of particular interest in the study). In this context a special focus is given to: (1) deposition rate of Fe particles, (2) optical properties (refractive index) of mineral dust (particularly iron oxides particles) and (3) impact of dust alkalinity (e.g., CaCO3) on the acid mobilization of iron particles (otherwise known as dust aerosol potential buffering). To the best of my knowledge, this is the first study to analyze dry deposition measurements collected using passive samplers by means of a single-particle SEM-EDX Analysis approach (particularly in the size fraction larger than 10 μm).

3 General dust properties (size distribution, composition, sources and transport patterns)

3.1 Size distribution

A major source of uncertainty in quantifying the impact of dust aerosol on Earth's climate is due to the inconsistency in representation of dust size distribution by models (Liu et al., 2011; Mahowald et al., 2014). The particle size distribution defines the emission and deposition fields for mineral dust particles. Furthermore, it also affects the life time of dust particles and interaction of dust with radiation, clouds, and water droplets (Denjean et al., 2016). The size of dust aerosol particles can range from 100 nm to ~100 µm in diameter (Ryder et al., 2013; Weinzierl et al., 2009) (see also Figure 2).

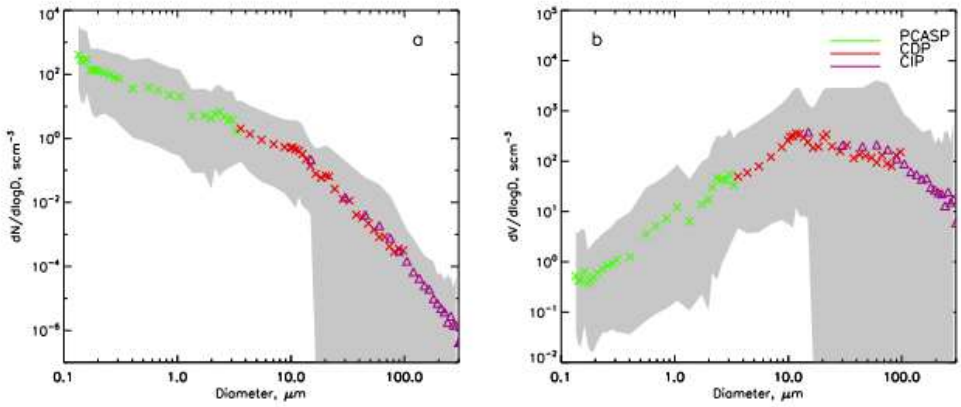

Figure 2: Mineral dust size distributions measured by different instruments for number distribution (a) and volume distribution (b). Grey shading represents minimum and maximum values measured, taken from Ryder et al. (2013).

3.2 Composition of atmospheric dust aerosols

Chemical composition is one of the most important parameters in determining the radiative forcing of deposited mineral dust aerosol particles (Axson et al., 2016). Mineral dust aerosol particles are consisting of a complex mixture of different minerals groups, mainly clays, quartz, feldspars, calcite (mainly gypsum and dolomite) and iron oxides (Kandler et al., 2007; Klaver et al., 2011). The abundance of different constituent can depend on different factors such as: the region of dust origin, the way how it is mobilized, and chemical and physical transformation

processes happening during dust transport in atmosphere (Jaszczur et al., 2019; Kandler et al., 2007; Langmann, 2013).

3.3 Prominent dust sources

Knowledge of the particular sources and hotspots of mineral dust particles at different geographic and time scales is very important for improving the forecast accuracy of dust events by numerical models of Earth's climate and air quality (Heinold et al., 2016; Wang et al., 2012). Previous studies (Gao et al., 2001; Prospero et al., 2002) has shown that there is a temporal and spatial variability of mineral dust transport over ocean. Most of active dust sources are mainly located in arid and semi-arid regions at sub-tropical latitudes in which dry climate prevail and the subsiding air masses stabilize the atmosphere (Schepanski et al., 2014).

The Sahara Desert and the Sahelian region in North Africa, the Gobi and Taklamakan deserts in Asia, the Australian and South American deserts and the Arabian Peninsula are regions identified to be the prominent dust source regions (Prospero et al., 2002). Because of its greater dust emission flux and the number of dust emission events, the Sahara Desert is regarded to be the largest dust source at global scale (Schepanski et al., 2014). Figure 3 shows major global dust sources and locations of dust records.

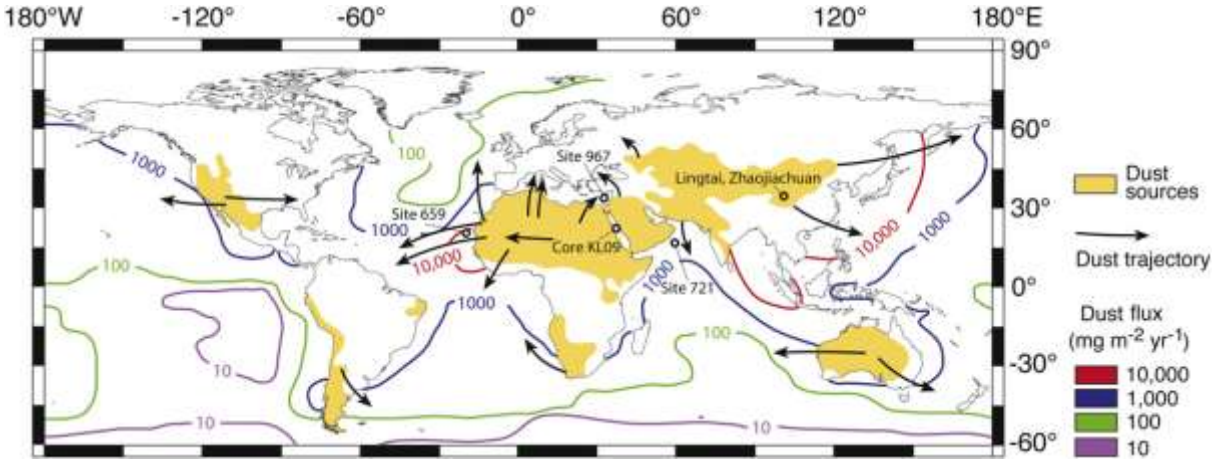

Figure 3: Major global dust sources and locations of dust records, taken from Roberts et al. (2011)

4 Theory

In this section, the basic concepts associated with dust deposition is discussed. In this perspective, atmospheric dust cycle, deposition steps, mechanisms of deposition, different deposition models described and different experimental techniques are assessed.

4.1 The Atmospheric Dust Cycle

The motion of mineral dust in the Earth system commonly referred as atmospheric dust cycle (Schepanski, 2018) and it generally consists of emission, transport and deposition processes (see Figure 4). Dust emission is based on complex interactions between the wind and the soil surface from which the dust is originating (Kok et al., 2012; Schepanski, 2018). Similarly dust transport, is the phenomena in the air, where the suspended dust particles are carried over within the atmospheric wind flow (Schepanski, 2018). Atmospheric dust deposition is a third process in atmospheric dust cycle in which dust particles are transported from the atmosphere onto Earth's surface (Osada et al., 2014; Seinfeld and Pandis, 2006). Different factors such as proprieties of the airborne dust particles, atmospheric flow conditions and the underlying surface characteristics are known to affect dust deposition process (Knippertz and Stuut, 2014; Schepanski, 2018). With respect to dust removal mechanisms, wet and dry pathways are the two mechanisms for atmospheric deposition to occur. Dry deposition refers to the removal of particles from atmosphere to surface through different mechanical processes such as diffusion, turbulent and Brownian transfer and by gravitational settling processes while through wet processes, particles are deposited on the earth's surface mainly by means of rain snow or mist (Lovett, 1994; Osada et al., 2014; Vivanco et al., 2017). Dry deposition is believed to be the major deposition mechanism for mineral dust aerosol due to its mass is dominated by large particles (Textor et al., 2007), though the importance may vary depending on the local climate conditions (Prospero et al., 2010; Stuut et al., 2009). Globally, dry deposition contribute 65–80% of the total dust deposition (Textor et al., 2007). Surface wind speeds and local land surface characteristics (e.g. soil texture, soil moisture, and vegetation cover) are among the factors known to affect the dust uplift and entrainment in the atmosphere (Schepanski et al., 2014).

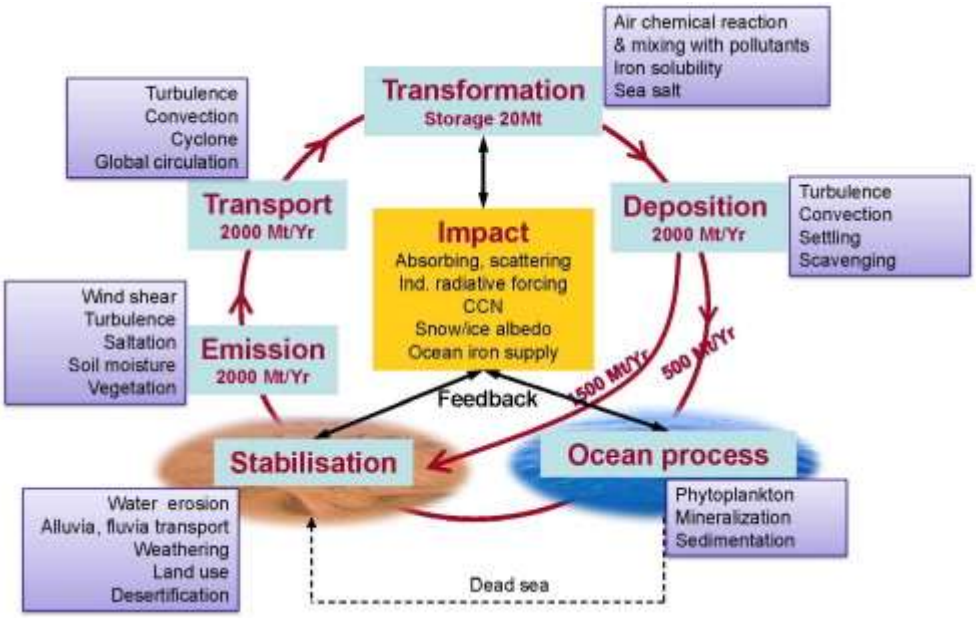

Figure 4: Schematic diagram of the dust cycle in the Earth system and related feedback mechanisms, taken from Shao et al. (2011b)

4.2 The deposition process

According to Wu et al. (1992), dust deposition process can be shortly explained in three steps.

1. Aerodynamic transport (transport due to atmospheric turbulence in the low layer of the Planetary Boundary Layer, PBL)

In this step, particle deposition process is independent of the physical and chemical nature of the particle, but it depends only on turbulent movement of air.

2. Boundary layer transport (transport in the Quasi-Laminar Sublayer, QLS)

In the laminar layer, turbulence becomes suppressed and in turn the Brownian diffusion (for small particles) and gravity (for heavier particles) get dominant and become the main factors for driving the deposition process.

3. Transfer to the ground (uptake by receptor)

This is the final step in deposition process, where the particles are collected by the receptor surface due to impaction, interception and Brownian motion. This deposition process exhibits a pronounced dependence on the surface type with which the particles interact with. Depending on the surface and particle properties, the deposited particles can either be retained to or rebounded from the surface.

4.3 Mechanisms of dust dry deposition

In the present work, the major focus lies on the third step, which is however considerably influenced by the second one.

When the dust moves and be close to the surface, it will hit and be captured by the surface commonly known as surface collection process via several mechanisms, including gravitational settling, impaction, interception and Brownian motion. In addition, the deposited dust on surface may bounce from the surface or become re-emitted in favorable wind conditions, which is so called resuspension.

4.3.1 Gravitational settling (sedimentation)

This is the process by which dust particles (especially towards the large end of the size distribution) settle to the surface due to gravity. In the free atmosphere, when the gravitational force and the friction drag and buoyancy force are in balance to each other, the terminal settling velocity is reached by the particles (Hinds, 1999).

4.3.2 Impaction

Aerosol particles have a tendency to travel along with the airflow near the surface. However, when there is a bend in the airway system, large particles (such as dust aerosol particles), do not turn with the air, rather, they collide or stick with a surface along the original path. And such a process is known as impaction. The impaction process may depend on particle mass and air velocity. For example, Droppo (2006) reported that particles with a diameter larger than 2 μm can be efficiently collected by impaction process. When a dust particle release from the eddy because of the inertia and collide with the surface, then this kind of a particular process may be termed as turbulent impaction, which could occur over in smooth or rough surfaces (Zhang, 2013).

4.3.3 Interception

Interception is another mechanism of dust deposition. This process takes place for particles of small inertia, which are able to follow the streamlines of the airflow, but are stopped because of the distance between the center of particle and the surface is smaller than the radius of the particle itself (Fuchs, 1964). Interception is often believed to be the main collection mechanism for the particles in the size range between 0.2 to 2 μm (Droppo, 2006).

4.3.4 Diffusion

Diffusion, which results in mixing or mass transport, is considered to be one of the important mechanisms for transport of dust particles without involving bulk motion (Kouznetsov and Sofiev, 2012; Zhang, 2013). The diffusion process may further split into Brownian diffusion or turbulent diffusion.

4.3.5 Rebound (resuspension)

Particle 'rebound', following deposition, is another process that takes place after particle-surface collision. This phenomenon could be primarily related to the kinetic energy of the incident particle. It can also depend on the adhesive conditions of the colliding surface (Zhang, 2013). According to Chamberlain (1975), the rebound process is believed to have strong influence on deposition of coarse particles, particularly in the size range larger than 5 μm, decreasing the effective deposition velocity.

4.4 A short review on various dry deposition velocity models

Deposition velocity (V_d) is an important concept in dust deposition parameterizations and it often defines the velocity a particle or a particle population experiences by the process of deposition (Niedermeier, 2014). It is a key concept to understand the deposition process. Several deposition models, from which deposition velocity can be calculated, are reported in the literature (Aluko and Noll, 2006; Noll and Fang, 1989; Noll et al., 2001; Piskunov, 2009; Slinn and Slinn, 1980; Wagner and Leith, 2001a). These models differ considerably in particle transport mechanism they consider and as a result, they yield different deposition velocity results (Kandler et al., 2018; Wagner and Leith, 2001a; Waza et al., 2019). For example, Slinn and Slinn (1980) developed a deposition velocity model for particle deposition on surface of water. The model considers the removal of particles from free atmosphere by means of eddy diffusion and sedimentation, and then followed by transport of particles through the viscous layer by means of Brownian diffusion, inertial impaction and sedimentation processes. Wagner and Leith (2001a) developed a deposition model that classifies the deposition velocity in to two components i.e. the ambient deposition velocity and the 'mesh factor'. The ambient deposition component describes the deposition velocity of a particle would have when depositing on horizontal flat plate smooth surface and it considers turbulent forces and gravity. The second component, the 'mesh factor' is an empirical correction meant to account for the effect of the

sampler and the sampler's mesh. Similarly, Noll and Fang (1989) developed a dry deposition velocity model from measurements of deposition of particles to surrogate surfaces. The model considers gravity and friction velocity to estimate deposition velocity. The Piskunov (2009) deposition model considers sedimentation and turbulent impaction to calculate deposition velocity for particles in supermicron particle size range.

4.5 Dust deposition measurement methods

Dry deposition has got considerable attention from the scientific community mainly due to its impacts on the environment; and consequently, significant work has been conducted to evaluate dry deposition using different techniques (Mohan, 2016). Dust deposition measurements are particularly a problem, for which a variety of methods has been developed (Dämmgen et al., 2005; Zhang et al., 2014). These methods can be roughly divided into the general categories of direct and indirect methods (Seinfeld and Pandis, 2012). While the direct method, dust deposition flux is measured by collecting dust deposited on the surface, the indirect approaches measure deposition flux by measuring quantities such as atmospheric dust concentration (Goossens, 2008; Zhang, 2013).

4.5.1 Direct method

4.5.1.1 'Surrogate' collecting surfaces

In this method, dust deposition flux is obtained by quantifying the amount of dust particles collected by a natural or surrogate surface. Surrogate surface is normally used to collect deposited dust directly and be combined with weight method to quantify collected dust. In the past, a wide variety of surrogate surfaces (Einstein et al., 2012; Goossens and Offer, 1994; Waza et al., 2019; Yamamoto et al., 2006) have been suggested. However, these surrogate surfaces are artificial acceptor surfaces and as a result and cannot mimic their complexity, they have a major representativity problem (Dämmgen et al., 2005). Another disadvantage of such a surrogate surfaces is that, any instrument in a natural air flow is an obstacle, and a result, it can change the air flow and, consequently, the deposition patterns around the surface. In this sense, the local turbulence induced by the surrogate instruments (size and shape of the instruments) is of a particular problem; and therefore different approaches (Franz et al., 1998; Huang et al., 2011; Munn and Bolin, 1971) have been suggested to minimize such turbulence impacts.

4.5.2 Indirect method

4.5.2.1 Micrometeorological eddy covariance/accumulation and gradient methods

Both eddy covariance/accumulation and gradient methods are micro- meteorological methods for measuring deposition fluxes (Businger, 1986; Dämmgen et al., 2005; Hicks, 1986). In these methods, deposition flux is expressed as the covariance of particle velocity and dust concentration; in addition, for these methods, the instantaneous wind velocity and particle concentration has to be simultaneously sampled (Zhang, 2013). High time resolution and independence from the surface properties is of advantage of these methods. However, these techniques have restricted use as they do measure fluxes until close to the surface, but not exactly on the surface itself. Furthermore, a considerable financial and maintenance resources is needed and are, therefore, they are less appropriate for deposition measurements involving longer time series (Hicks, 1986; Vandenberg and Knoerr, 1985). The flux gradient method involves measuring particle concentration at different heights and then calculating the deposition using the flux-gradient relationship (Businger, 1986; Zhang, 2013). Moreover, the dust diffusivity constant used in this calculation has large uncertainties (Cellier and Brunet, 1992).

4.5.2.2 Inferential methods

Inferential methods are yet another approach widely used for determining the atmospheric dust deposition. In this approach, deposition rate (DR) is calculated as the product of particle concentration (C) and deposition velocity (V_d) (Goossens, 2008; Junge, 1963; Kandler et al., 2018; Waza et al., 2019). The deposition velocity, which is often used to quantify the deposition process, is a complex parameter that depends on dust concentration, atmospheric properties, characteristics of the dust and deposition surface (Kandler et al., 2018; Zhang and Shao, 2014). However, the limitation of this method is that it can be a resource-intensive and may not be a good option for measurements involving longer time series.

5 Field comparison of dry deposition samplers for collection of atmospheric mineral dust: results from single-particle characterization

5.1 Introduction

Commonly, deposition is measured by passive techniques, which provide an acceptor area for depositing atmospheric particles. The advantage of these passive samplers is that they operate passively, resulting in simple and thus cheaper instruments, so that many locations can be sampled at a reasonable cost (Goossens and Buck, 2012). The usual lack of a power supply allows also for unattended remote setups. However, the most important disadvantage is that collection efficiency and deposition velocity is determined by the environmental conditions not under operator control, and in remote setups also frequently also unknown. That implies, in addition, that the sampler shape can have a strong and variable impact of the collection properties.

While there is previous work describing and modeling single samplers (Einstein et al., 2012; Wagner and Leith, 2001a, b; Yamamoto et al., 2006) and a few comparison studies (Goossens and Buck, 2012; Mendez et al., 2016), most previous studies (Goossens and Buck, 2012; López-García et al., 2013) only compare total mass, thereby neglecting size dependence and potential comparison biases. Also, a systematic assessment of the impact of wind conditions is not commonly carried out, but for example Mendez et al. (2016) showed that the efficiency of the BSNE and MWAC samplers for collecting PM_{10} varies with wind speed, and Goossens and Buck (2012) found that PM_{10} concentrations from BSNE and DustTrak samplers have comparable values for wind speeds from 2–7 m/s.

5.2 Sampling location and time

Sahara and Sahel provide large quantities of soil dust, resulting in a westward flow of mineral dust particles over the North Atlantic Ocean accounting for up to 50% of global dust budget (Goudie and Middleton, 2001; Schütz and Sebert, 1987). Because of its proximity to the African continent, the Canary Islands are influenced by dust particles transported from the Sahara and Sahel regions. Hence, Tenerife is one of the best locations study dust flux and consequently the

mineralogical composition and potential source regions of dust aerosol particles (Cordoba-Jabonero et al., 2016).

For this study, a two month (July to August 2017) aerosol collection and dry deposition sampling campaign at Izaña Global Atmospheric Watch Observatory (Bergamaschi et al., 2000; Rodríguez et al., 2015) (28.3085ºN, 16.4995ºW) has been conducted. Sampling inlet were placed at a height of 2 m above ground, on top of a measurement installation. The installation was made on a 160 m^2 flat concrete platform. The trade wind inversion, which is a typical meteorological feature of the station, shields most of the time the observatory from local island emissions (García et al., 2016). Therefore, the Izaña Global Atmospheric Watch Observatory is an ideal choice for in-situ measurements under “free troposphere” conditions (Bergamaschi et al., 2000; García et al., 2016).

6 Materials and Methods

6.1 Particle sampling

Samples were collected from different, commonly used samplers, namely Big Spring Number Eight (BSNE) (Fryrear, 1986), Modified Wilson and Cooke (MWAC) (Wilson and Cook, 1980), Sigma-2 (VDI2119, 2013) and Flat plate (UNC-derived) (Ott and Peters, 2008). In addition, the free-wing impactor (FWI) (Kandler et al., 2018) was used to collect coarser particles. The BSNE, MWAC, FWI and Filter Sampler were mounted on wind vanes to align them to the ambient wind direction. Samples were collected continuously, and substrates were exchanged at intervals of 24 hours. The sampling duration for FWI (12 mm Al-stub) was 30 min only to avoid overloading. The sampling duration for filter sampler was set to be one hour. It has to be noted that the PM_{10} from optical measurements for this particular 0.5 or 1 hour only deviates by 2 % and 0.2 % respectively from the 24-h-average.

6.2 Dust deposition samplers

6.2.1 Flat plate sampler

The Flat plate sampler used in this work was taken from the original Flat plate geometry used in Ott and Peters (2008). Briefly, the geometry contains two round brass plates (top plate diameter 203 mm, bottom plate 127 mm, thickness 1 mm each) mounted in a distance of 16 mm. Unlike the original design, the geometry of the current work has a cylindrical dip in the lower plate, which recedes the sampling substrate – a SEM stub with a thickness of 3.2 mm – from the airflow, thereby reducing the flow disturbance. A preliminary study with the modified and original setup side-by-side in a rural environment had shown that this recession approximately doubles the collection efficiency for large particles. In this design, larger droplets (> 1 mm) are prevented by this setup from reaching the SEM stub surface at the local wind speeds Ott and Peters (2008). As described in Wagner and Leith (2001a); (Wagner and Leith, 2001b), the main triggers for particle deposition on the substrates for this sampler are diffusion, gravity settling, and turbulent inertial forces, of which only the latter two are relevant in our study.

6.2.2 Upward-downward deposition rate sampler

It is important to compare the upward and downward rates to understand the turbulent and the gravitational share in aerosol deposition rate measurement. Following an approach by Noll and Fang (1989), it was assumed that turbulent transport is the main mechanism for upward-directed deposition rate while turbulent transport and sedimentation are the mechanism of for the downward one. Therefore, a sampler with an upward- and a downward-facing substrate in analogy to the Flat plate sampler was designed. Air is flowing between two circular steel plates thick 1 mm with a diameter of 127 mm. In the centers of the plates, two substrates are mounted opposite to each other. The substrate holders are recessed, so that their adhesive collection surface is in plane with the steel surface. The construction is mounted into a frame with a distance of 16 mm between the plates / substrates.

6.2.3 Sigma-2 sampler

The Sigma-2 sampling device is described in Dietze et al. (2006); (Schultz, 1989; VDI2119, 2013). Briefly, the geometry consists of a cylindrical sedimentation tube with a height of about 27 cm made of antistatic plastic, which is topped by a protective cap with diameter of 158 mm. At its top, the cap has four rectangular inlet windows (measuring 40 mm x 77 mm, all at the same height) at its side providing away for passive entrance of particles to the collection surface. Once entered the tube, particles are assumed to settle down to the collection surface due to gravitation (Stokes' law) (VDI2119, 2013). The samplers designed in a way that it protects the sample from direct radiation, wind and precipitation.

6.2.4 The Modified Wilson and Cooke (MWAC) sampler

The MWAC sampler is based on an original design developed by Wilson and Cook (1980). The sampler consists of a closed polyethylene bottle, serving as settling chamber, to which an inlet tube and an outlet tube have been added. The MWAC sampling bottles are 95 mm long with a diameter of 48 mm. The two inlet and outlet plastic tubes with inner and outer diameter 8 and 10 mm respectively, pass air through the cap into the bottle and then out again. The large volume of the bottle relative to the inlet diameter makes the dust particles entering the bottle to be deposited in the bottle due to the flow deceleration the total bottle area, and due to impaction below the exit of the inlet tube. The air then discharges from the bottle via the outlet tube.

MWAC is one of the most commonly used samplers (Goossens and Offer, 2000) and has a high sampling efficiency for large particles (Mendez et al., 2016).

6.2.5 The Big Spring Number Eight (BSNE) sampler

The BSNE sampler, originally designed by Fryrear (1986), is intended to collect airborne dust particles from the horizontal flux (Goossens and Offer, 2000). Briefly, the particle laden air passes through a rectangular inlet (21 mm wide and 11 mm high, with a total area of 231 mm^2). Once inside the sampler, air speed is reduced by continuous cross section increase (angular walls) and the particles settle out on a collection surface. Air discharges through a mesh screen.

6.3 Free-wing impactor (FWI)

A free rotating wing impactor (Jaenicke and Junge, 1967; Kandler et al., 2018; Kandler et al., 2009) was used to collect particles larger than approximately 5 µm. A FWI has a sticky impaction surface attached to a rotating arm that moves through air; particles deposit on the moving plate due to their inertia. The rotating arm is moved at constant speed by a stepper motor, which is fixed on a wind vane, aligning the FWI to wind direction. The particle size cut-off is defined by the impaction parameter, i.e. by rotation speed, wind speed and sample substrate geometry. Details of working principle of FWI can be obtained from Kandler et al. (2018).

6.4 Filter sampler

A filter sampler with Nucleopore filters (Whatman® Nuclepore™ Track-Etched Membranes diam. 25 mm, pore size 0.4 µm, polycarbonate) mounted on a wind vane was used for iso-axial particle collection. An inlet nozzle of 6 mm was used to achieve pseudo-isokinetic conditions. Sample flow (0.75 m^3/h volumetric at ambient conditions) was measured by a mass flow meter (MASS-STREAM, M+W instruments, Leonhardsbuch, Germany). The filter sampler was operated at least two times a day.

6.5 Ancillary Aerosol Data

Additional information regarding the aerosol particle size distributions has been obtained by using an optical particle counter (OPC, GRIMM, Ainring, Germany), which is operationally

available at the Izaña Global Atmospheric Watch observatory (Bergamaschi et al., 2000; Rodríguez et al., 2015).

6.6 Wind measurements

An ultra-sonic anemometer (Young model 81000, R. M. Young Company, Traverse City, MI, USA) was installed at approximately 2 m height above the ground to obtain the 3-D wind velocity and direction. It was operated with a time resolution of 10 Hz to get basic information on turbulence structure.

6.7 SEM-Analysis

All aerosol samples (except the filter sampler) were collected on pure carbon adhesive substrates (Spectro Tabs, Plano GmbH, Wetzlar, Germany) mounted to standard SEM aluminum stubs. The filter samples were stored in standard 'Petrislides' (Merck KGaA, Darmstadt, Germany). All adhesive samples were stored in standard SEM storage boxes (Ted Pella Inc, Redding, CA, USA) in dry conditions at room temperature. Individual particle analysis by automated scanning electron microscopy (SEM; FEI ESEM Quanta 400 FEG, FEI, Eindhoven, The Netherlands; operated at 12.5 kV, lateral beam extension 3 nm approx., spatial resolution 160 nm) was used to characterize particles for size and composition. A total of 316,000 particles from six samplers was analyzed. 26 samples from BSNE (53,000 particles), 23 samples from MWAC (49,000), 23 samples from SIGMA-2 (39,000), 18 samples from Flat plate (12 mm) (24,000), 22 samples from Flat plate (25 mm) (21,000), 13 samples from Filter (80,000) and 12 samples from FWI-12 mm (50,000) were analyzed. Each sample was characterized at areas selected by a random generator, until a total of 3,000 particles with projected area diameters greater than 1 µm was reached. For particle identification, the backscattered electron image (BSE-image) has been used, as dust particles contain elements with higher atomic number than carbon and therefore appear as detectable bright spots in the BSE-image.

Chemistry information was derived by energy-dispersive X-ray analysis (EDX; Oxford X-Max 120, Oxford Instruments, Abingdon, United Kingdom). The internal ZAF-correction of the detector / software system – based on inter-peak background radiation absorption measurements for correction – was used for obtaining quantitative results.

6.8 Particle size determination

The image analysis integrated into the SEM-EDX software determines the size of particles as a projected area diameter.

$$\mathbf{d_g} = \sqrt{\frac{4B}{\pi}} \qquad \textbf{(1)}$$

Where **B** and $\boldsymbol{d_g}$ are the area covered by the particle on the sample substrate and the projected area diameter respectively.

Following Ott et al. (2008), the volumetric shape factor, $\boldsymbol{S_v}$ is determined from the count data as:

$$\boldsymbol{S_v} = \frac{P^2}{4\pi A} \qquad \textbf{(2)}$$

Where P and A are the perimeter and the projected area of the particle respectively.

The volume-equivalent diameter (sphere with the same volume as the irregular shaped particle) is then, calculated from the projected area diameter via the volumetric shape factor (Ott et al., 2008) and is expressed by particle projected area and perimeter as

$$\boldsymbol{d_v} = \frac{4\pi B}{P^2}\boldsymbol{dg} = \frac{1}{P^2}\sqrt{64\pi B^3} \qquad \textbf{(3)}$$

The aerodynamic diameter (d_a) is calculated from projected area diameter through the use of a volumetric shape factor and aerodynamic shape factor (Wagner and Leith, 2001b)

$$\boldsymbol{d_a} = \boldsymbol{d_v}\sqrt{\frac{\rho_p}{S_d \rho_0}} \qquad \textbf{(4)}$$

With $\boldsymbol{S_d}$ the aerodynamic shape factor; $\boldsymbol{\rho_p}$ and $\boldsymbol{\rho_0}$ are particle density and unit density respectively. For this work, a value of S_d = 1.41 was used (Davies, 1979). Cunningham's slip correction was neglected in this study, as all particles considered were super-micron size.

6.9 Mass and number deposition rate calculation

The mass deposition rate (MDR) and number deposition rate (NDR) are calculated from deposited particle numbers per area, individual particle size and, in case of MDR, density. The particle density was assumed to be equal the bulk material density of the dominating identified compound for each particle (Kandler et al., 2007). A window correction (Kandler et al., 2009) was applied to the particle deposition rate as:

The mass deposition rate (MDR) and number deposition rate (NDR) are calculated from deposited particle numbers per area, individual particle size and, in case of MDR, density. The particle density was assumed to be equal the bulk material density of the dominating identified compound for each particle (Kandler et al., 2007). A window correction (Kandler et al., 2009) was applied to the particle deposition rate as:

$$\boldsymbol{C_w = \frac{w_x w_y}{(w_x - d_p)(w_y - d_p)}} \qquad \textbf{(5)}$$

Where w_x and w_y are the dimensions of the analysis rectangle.

The MDR of the samples is then determined as

$$\boldsymbol{MDR = \frac{1}{Ati} \sum_k \rho\, d_p^3 C_w(d_p, k)} \qquad \textbf{(6)}$$

Similarly, the NDR of the samples is determined as

$$\boldsymbol{NDR = \frac{1}{Ati} \sum_k C_w(d_p, k)} \qquad \textbf{(7)}$$

With A is the total analyzed area, t is the sample collection time, $\boldsymbol{\rho}$ particle density and k is an index of the particle.

Size distributions for all properties were calculated for the logarithmic-equidistant intervals of 1-2 µm, 2-4 µm, 4-8 µm, 8-16 µm, 16-32 µm, and 32-64 µm.

7 Modeling atmospheric concentrations and size distributions from flux measurements

Concentrations are calculated from the deposition rate using different deposition velocity models for different samples, namely the models of Stokes and Piskunov (Piskunov, 2009). The basic relationship between concentration and deposition rate was already given by Junge (1963), as the ratio of deposition rate to concentration:

$$\boldsymbol{V_d = DR/C} \qquad \textbf{(8)}$$

With DR is deposition rate and C is concentration. Note that the formulation is independent of the type of concentration, i.e. it can be equally applied to number or mass concentrations.

All different approaches now give different formulations for the deposition velocity, based on a set of assumptions and neglections.

7.1 Stokes settling

Terminal settling velocity ($\boldsymbol{V_{ts}}$) is calculated according to Stokes' law.

$$\boldsymbol{V_{ts} = \frac{d_p^2 g(\rho_p - \rho_a)}{18\mu}} \qquad \textbf{(9)}$$

Where d_p is the particle size, g is the gravitational acceleration (9.81 m/s^2); $\boldsymbol{\rho_p}$ the density of particle; $\boldsymbol{\rho_a}$ the air density; μ is the dynamic viscosity of air (1.8*10^{-5} kg/(ms)).

7.2 Turbulent deposition and more complex deposition models

To calculate the turbulent impaction velocity, which depends on the wind speed, the friction velocity is needed. Friction velocity (u_*), which is a measure of wind generated turbulence is one the most important variables affecting deposition velocity (Arya, 1977). Mainly two different approaches have been used to estimate u_*. On one hand the momentum flux or the eddy covariance (EC) approach (Ettling, 1996), which directly estimates u_* from the correlations between the measured horizontal and vertical wind velocity fluctuation, and on the other the law of the wall (LoW) approach (Shao et al., 2011a), which estimates u_* from the wind profile. The latter can be approximated from free-stream velocity and roughness

assumptions (Wood, 1981), where the flow inside the sampler is assumed to be in the hydraulically smooth regime (Schlichting, 1968). Figure 5 shows the correlations between u_* estimated using Wood (1981) and Ettling (1996) approaches. Obviously, the approaches lead to different results, for which no clear explanation is available (Dupont et al., 2018) .

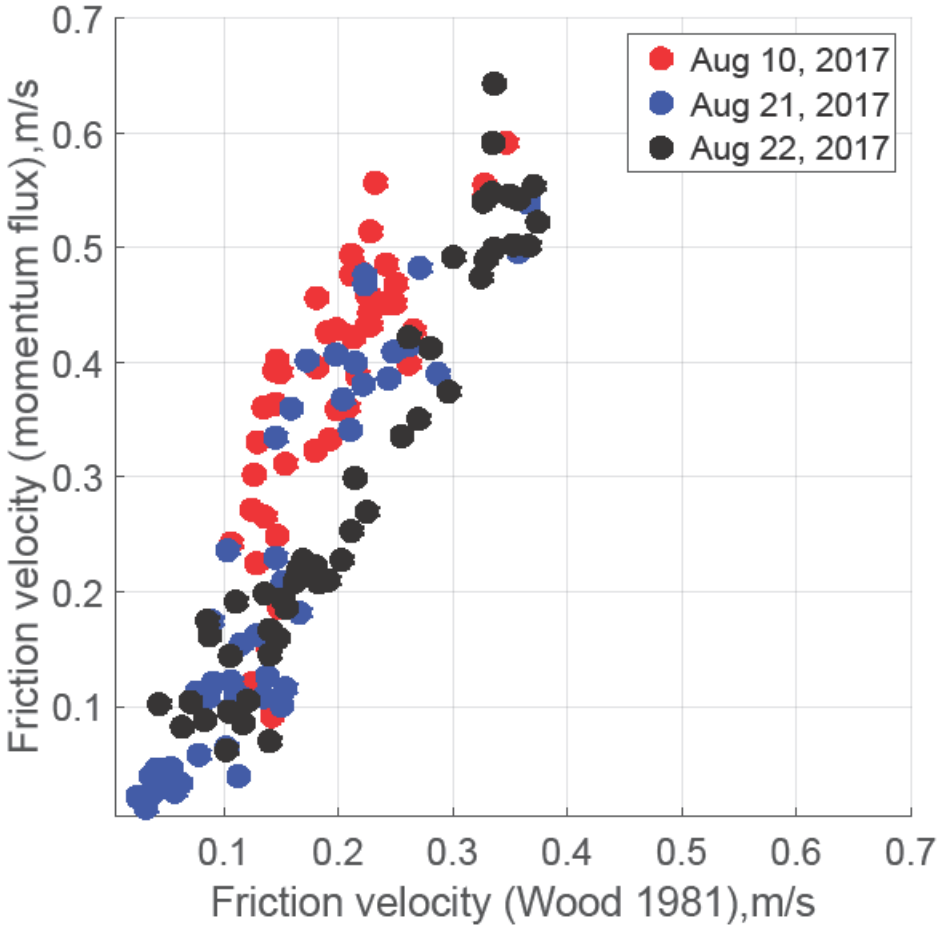

Figure 5: Comparison of the friction velocities obtained from the momentum flux and the Wood 1981 approaches for different days with different wind speeds (average wind speed =2.9 m/s, 2.1 m/s, 3.1 m/s for Aug 10, Aug 21, and Aug 22, 2017, respectively).

For the current work, the friction velocity is calculation is based on Wood (1981) approach:

$$u_* = (u/\sqrt{2})\,[(2log10(Re) - 0.65)^{-1.15}] \quad \textbf{(10)}$$

Where Re is the flow Reynolds number at the sampling stub location and is given as

$$Re = uX/V \quad \textbf{(11)}$$

X is the distance from the lower plate edge to the center of the sampling stub (6.3 cm) and V is kinematic viscosity.

The reason why Wood (1981) is selected over the Ettling (1996) approach is a) its simplicity, as it requires only average wind speeds instead of 3D high resolution ones, and therefore will be more commonly applicable; and b) the fact that the momentum approach yields sometimes uninterpretable data, in particular in case of buoyancy-driven flow. For some case studies, both approaches are compared below.

There are a variety of models estimating the particles deposition speed (Aluko and Noll, 2006; Noll and Fang, 1989; Noll et al., 2001; Piskunov, 2009; Slinn and Slinn, 1980; Wagner and Leith, 2001a) (see Figure 6). These different deposition velocity models yield different results, which could be due to the negligence of unaccounted forces (Lai and Nazaroff, 2005) or due to the way how friction velocity is determined or can be related to suppositions by different models (Kandler et al., 2018). Unless otherwise stated, the particle density used in deposition velocity calculation is 2600 kg/m^3.

It can be noted that a particular deposition model therefore may not be suitable in different cases for describing the deposition velocity precisely, so as a result concentrations derived from deposition rate measurements are likely to be biased (Giardina and Buffa, 2018; Kandler et al., 2018).

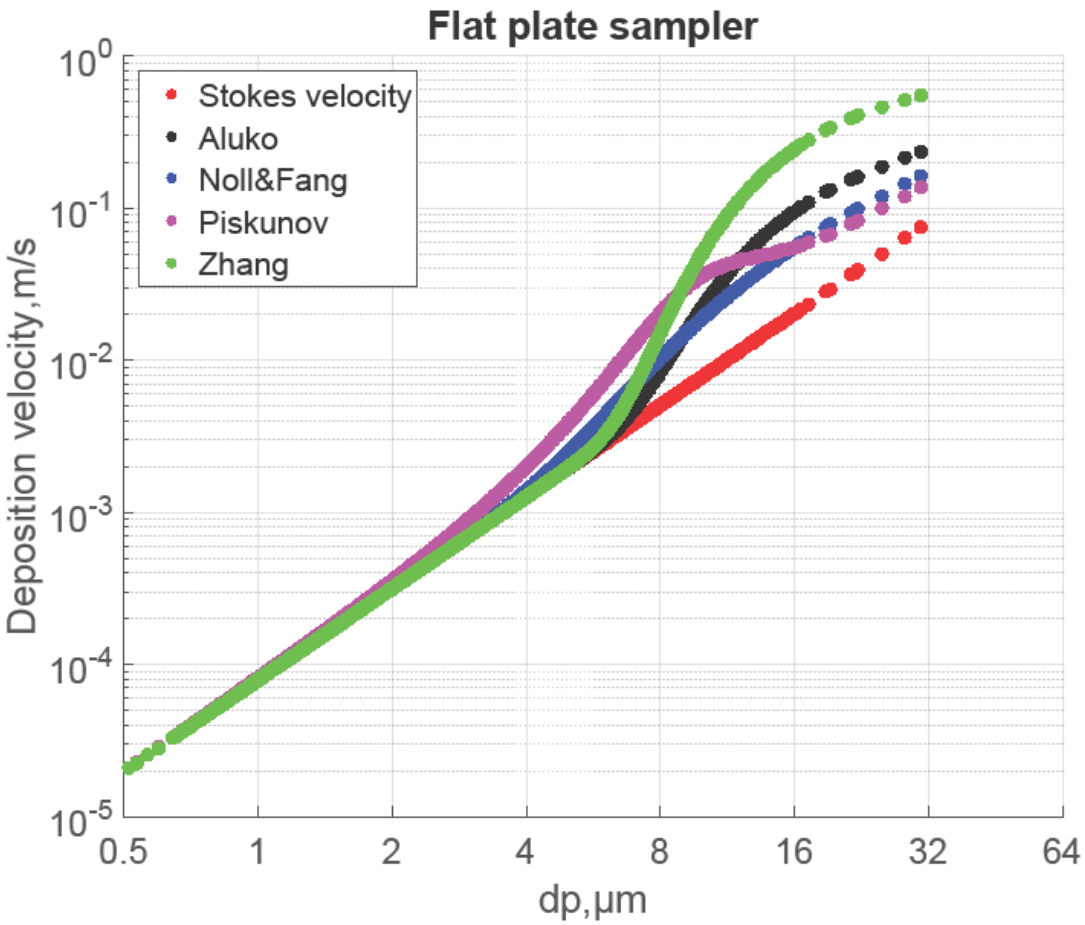

Figure 6: Deposition velocities for single particles to a smooth surface (Flat plate sampler) calculated by using a set of different classical deposition models for Tenerife samples (Aug 9, 2017; average wind speed =3.0 m/s).

7.3 Deposition models applied to the samplers

Table 1 shows the different deposition velocity models applied to the various samplers. The Piskunov deposition velocity model is made for flat surfaces, and therefore it is applied to BSNE and Flat plate, where deposition occurs to such surfaces. For the Sigma-2 sampler, it is assumed that each particle settles with the terminal settling velocity (Tian et al., 2017), and therefore Stokes' velocity was used for calculation of concentrations. In the case of MWAC, a different approach was required due to its geometry. It is internally in principle an impactor design with the incoming tube pointing at the substrate, but is operating at very low flow speed and therefore Reynolds numbers. As a result, it cannot be described by the impactor theory only. Therefore, I assumed that the deposition velocity can't become smaller than the one prescribed by the Piskunov model. As a result, I derived a velocity model based on wind speed (or a reduced wind speed) and calculated the collection efficiency assuming the MWAC to act

as impactor for particles in the range of the cut-off diameter and larger. For smaller particles, I assumed that flow is like a flow over a smooth surface, so the Piskunov deposition velocity model was applied (e.g., as soon as the deposition velocity from impactor considerations becomes smaller than the Piskunov one, the latter was used).

Table 1: A summary of different deposition velocity models applied to the samplers.

Sampler	Deposition velocity model
Sigma-2	Stokes' velocity
Flat plate	Piskunov
BSNE	Piskunov
MWAC	Combination of Piskunov and Impaction curve

7.4 Determining the size distributions for mass concentration from the free-wing impactor measurements

Considering the windows correction and the collection efficiency dependence on the impaction speed and geometry, the overall collection efficiency E is calculated according to (Kandler et al., 2018). After calculating the collection efficiency, the atmospheric concentration is calculated from deposition rate and deposition velocity as:

$$\mathbf{C} = \frac{\mathbf{DR}}{\mathbf{V_d}} = \frac{\boldsymbol{DR}}{\boldsymbol{E\,V_{imp}}} \qquad \textbf{(12)}$$

With E being the collection efficiency and v_imp the impaction velocity, calculated from ambient wind speed and rotation speed.

7.5 Determining the size distributions for mass concentration from the filter sampler measurements

Apparent number concentrations are determined from the particle deposition rate and the volumetric flow rate calculated from the mass flow for ambient conditions. The inlet efficiency ($\boldsymbol{Eff_{in}}$) – accounting for the difference in wind speed and inlet velocity - is calculated as a function of Stokes number (Stk) (Belyaev and Levin, 1974). The ambient concentration $\boldsymbol{N_{out}}$

is calculated by dividing the measured number concentration by the inlet efficiency. The effect for the regarded particles size, however, is small in comparison to the differences between the samplers.

7.6 Statistical uncertainty

Owing to the discrete nature of the particle size measurement, the uncertainty coming from counting can pose a significant contribution to the uncertainty of mass deposition rate measurement (Kandler et al., 2018). It is, therefore, important to assess the uncertainties in our mass deposition rate measurements, which is done in accordance to the previous work (Kandler et al., 2018). For the mass deposition rate, the statistical uncertainty is assessed by a bootstrap simulation approach using Monte Carlo approximation (Efron, 1979). In this work, the bootstrap simulations and the two-sided 95 % confidence intervals calculation were performed by using Matlab's bootstrap function (MATLAB R2016a (MathWorks, Inc). Here, MATLAB function uses a non-parametric bootstrap algorithm (Neto, 2015) to compute the 95% bootstrap confidence interval.

8 Computational fluid dynamics (CFD) simulation

Computational fluid dynamics (CFD) simulations were conducted to predict the deposition of particles on to different passive samplers (MWAC, Sigma-2 and Flat plate). A discrete phase model without interaction with continuous phase was used to calculate the trajectories of the particles. The CFD software ANSYS-FLUENT 18.2 was used for performing the numerical simulations.

8.1 Evaluating the mean flow field

In a first step the geometry of samplers was created using ANSYS DesignModeler. In a second step, an enclosure around the geometry was generated. To ensure that there are no large gradients normal to the boundaries at the domain boundary, the domain was created depending on the width, the height and the length of the geometries. The space in front of the geometry is two times the height of the sampler, the space behind the sampler is ten times the height, the space left and right of the geometry is five times the width of the geometry and the space below and above the sampler is five times the height.

Afterwards a mesh was created using the ANSYS Meshing program. For the enhanced wall treatment the first near-wall node should be placed at the dimensionless wall distance of y^+^≈1. The dimensionless wall distance is given by

$$\boldsymbol{y^+ = \frac{u_* y}{\nu}} \qquad \textbf{(13)}$$

With y the wall-normal distance from the wall to the cell centers, k the turbulence kinetic energy and μ the dynamic viscosity of the fluid. If Re_y> 200 the k-epsilon model is used. Re_y< 200 the one-equation of Wolfstein is employed (Chmielewski and Gieras, 2013; Fluent, 2015). The flow field was calculated by solving the Reynolds Averaged Navier Stokes's equations with the software ANSYS Fluent. Standard k-epsilon model was used to calculate the Reynolds-stresses. The boundary conditions at the sides of the domain were set to symmetric. The inlet boundary condition was set to 2, 4 or 8 m/s with air as fluid (Density: 1.225 kg/m^3, viscosity: 1.7849*10^{-5} kg/(ms)). The outlet boundary condition was set to pressure outlet.

The turbulence intensity $\mathbf{T_i}$ was calculated as

$$\mathbf{T_i} = \frac{\left(\frac{2}{3}\mathbf{k}\right)^{1/2}}{\mathbf{v}} \qquad \textbf{(14)}$$

With k the turbulence intensity and v the velocity at the inlet of the domain.

8.2 Detail of the sampler construction for CFD geometries

8.2.1 Flat plate sampler

The geometry of Flat plate sampler (left) and CFD modeling domain and velocity magnitude (right) are shown in Figure 7. The bottom part of the sampler is a cylinder with a diameter of 28.9 mm and a height of 29 mm followed by another cylinder with a diameter of 40 mm and a height of 14 mm. The first plate has a diameter of 127 mm and a thickness of 1 mm. In the middle of the area, the deposition area is defined as a circular surface with a diameter of 12 mm or 25 mm respectively. The upper plate has the same thickness but a diameter of 203.2 mm. Three columns hold the upper plate. The center of these columns is arranged on a diameter of 116 mm. The diameter of the columns is 5 mm with a height of 16 mm.

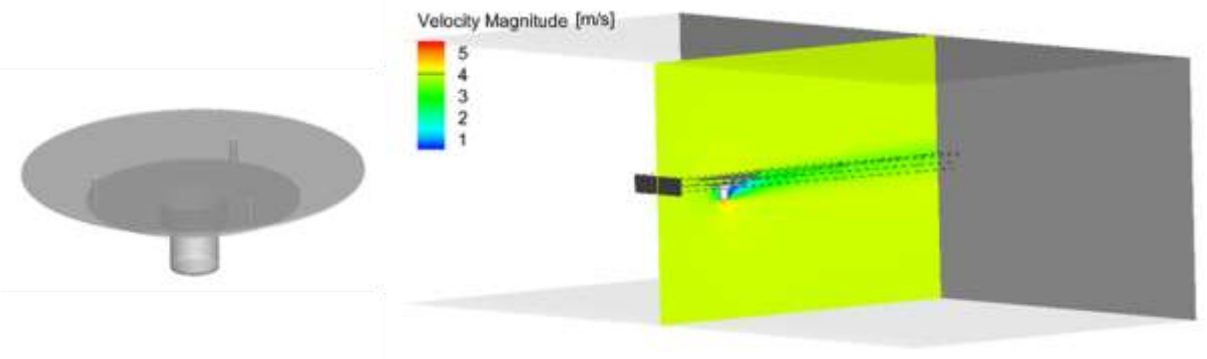

Figure 7: Geometry of Flat plate sampler (left), CFD modeling domain and velocity magnitude, inlet velocity: 4m/s (right); in addition, the injection area is shown in black (width 0.2 m, height 0.05 m) along with exemplary particle trajectories.

8.2.2 Sigma-2 sampler

The geometry of Sigma-2 sampler (left) and CFD modeling domain and velocity magnitude (right) are shown in Figure 8. At the bottom, it consists of a mounting pole with an inner

diameter of 36 mm and an outer diameter of 50 mm with a height of 32 mm. Then follows the bottom of the sampler with a diameter of 108 mm and a height of 14 mm. The wall of the geometry has an inner diameter of 104 mm and is 260 mm high. From a height of 214 mm the cover of the sampler starts. It has an inner diameter of 154 mm and an outer diameter of 158 mm. In it, there are four openings, which starts at a height of 226 mm and have a width of 40 mm and a height of 75 mm. The same openings exist in the inner radius as well however turned by 90 degrees. The collector inside the geometry has a diameter of 12 mm, a height of 13 mm and is positioned centrally at the bottom.

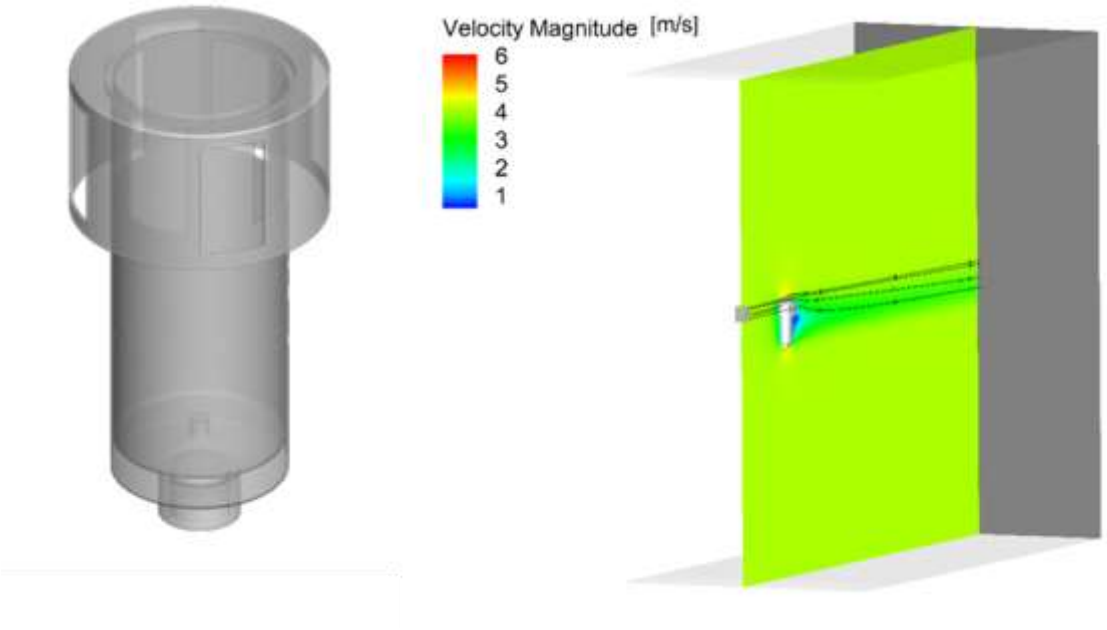

Figure 8: Geometry of Sigma-2 sampler (left), CFD modeling domain and velocity magnitude; inlet velocity: 4m/s (right); in addition, the injection area is shown in black (width 0.2 m, height 0.1 m) along with exemplary particle trajectories.

8.2.3 MWAC sampler

The geometry of MWAC sampler (left) and CFD modeling domain and velocity magnitude (right) are shown in Figure 9. The bottom diameter of the sampler is 48 mm with a thickness of 1.25 mm. Afterwards the inner diameter is 45.4 mm up to a height of 60 mm. The diameter then narrows semi circularly to 24 mm. The lid of the sampler has a diameter of 40 mm and a height of 17 mm.

The pipes have an inner diameter of 7.5 mm and a thickness of 1.25 mm. The pipe looking into the direction of the velocity inlet is longer and ends 23 mm above the bottom of the sampler.

The outgoing pipe starts 38 mm above the bottom. The collector inside the geometry has a diameter of 12 mm, a height of 13 mm and is positioned centrally at the bottom.

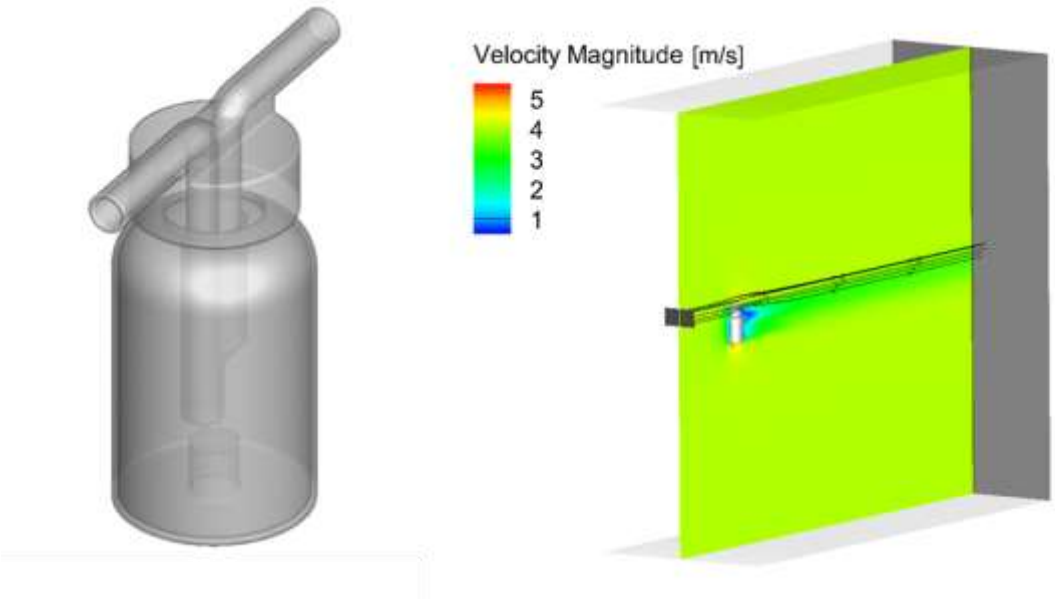

Figure 9: Geometry of MWAC sampler (left), CFD modeling domain and velocity magnitude of MWAC sampler, inlet velocity: 4m/s (right); in addition, the injection area is shown in black (width 0.1 m, height 0.05 m) along with exemplary particle trajectories.

8.3 Calculation of deposition velocity

Different cases were calculated for the Flat plate sampler (deposition area of 12 and 25 mm), for the Sigma-2 and for the MWAC (Figure 10). For the Flat plate, a mesh with 3,920,000 cells was generated, for the Sigma-2 one with 7,600,000 cells and for the MWAC one with 4,620,000. After the meshing, the flow fields were calculated. Figure 10 shows as an example the velocity magnitude in the middle of the domain for a velocity of 4 m/s at the inlet.

In the last step, particles were injected into the velocity field and their trajectories computed. For all samplers, the deposition area boundary condition was set to “trap” and the walls were defined as reflecting boundaries. Different particle sizes (1, 2.5, 5, 10, 20 and 50 µm, Stokes’ diameter) for three different wind speeds (2, 4, 8 m/s) were investigated. The particles density was set to a value of 2600 kg/m³ to match an approximate dust bulk density. The particle concentration was $4*10^8$ /m^2 in all cases, while the injection area was adjusted to the geometries (Figure 10).

The number of particles trapped in the deposition area was determined. The deposition velocity V_d was calculated by

$$V_d = \frac{N_{pt} v}{A_d C_p} \qquad \textbf{(15)}$$

with N_{pt} the number of trapped particles at the deposition area, v the velocity of the air at the inlet boundary of the domain, A_d the deposition area and C_p the particle concentration at the particle injection area (Sajjadi et al., 2016).

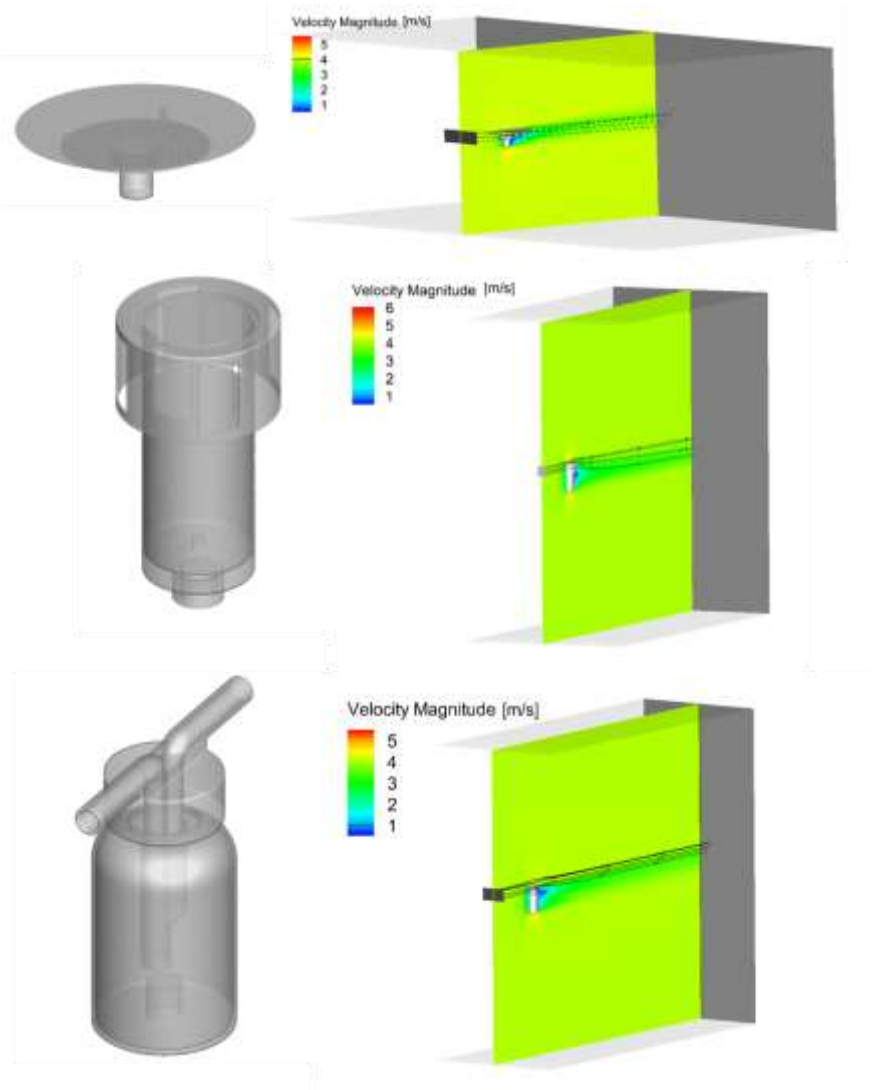

Figure 10: Geometries of Flat plate sampler (top), Sigma-2 sampler (middle), MWAC sampler (bottom). CFD modeling domain and velocity magnitude, inlet velocity: 4 m/s (right); in addition, the injection area is shown in black (Flat plate sampler: width 0.2 m,

height 0.05 m; Sigma-2-sampler: width 0.2 m, height 0.1 m; Bottle sampler: width 0.1 m, height 0.05 m) along with exemplary streamtraces.

8.3.1 Velocity contours and vectors for the samplers

8.3.1.1 Flat plate Sampler

For the Flat plate sampler, stream velocities and turbulence intensities are shown in Figure 11. The formation of the boundary layer at the wall of the sampler is clearly visible at all velocities. At the central sampling location, the flow between the plates has the same velocity as the free stream, so for the analytical deposition models, the lower plate can be treated as a single surface. The highest velocity is found at the sharp edge at the bottom of the sampler. Due to the high velocity gradients in this part there is also the highest turbulence intensity in the domain. As expected, the turbulent wake becomes smaller with increasing wind speed.

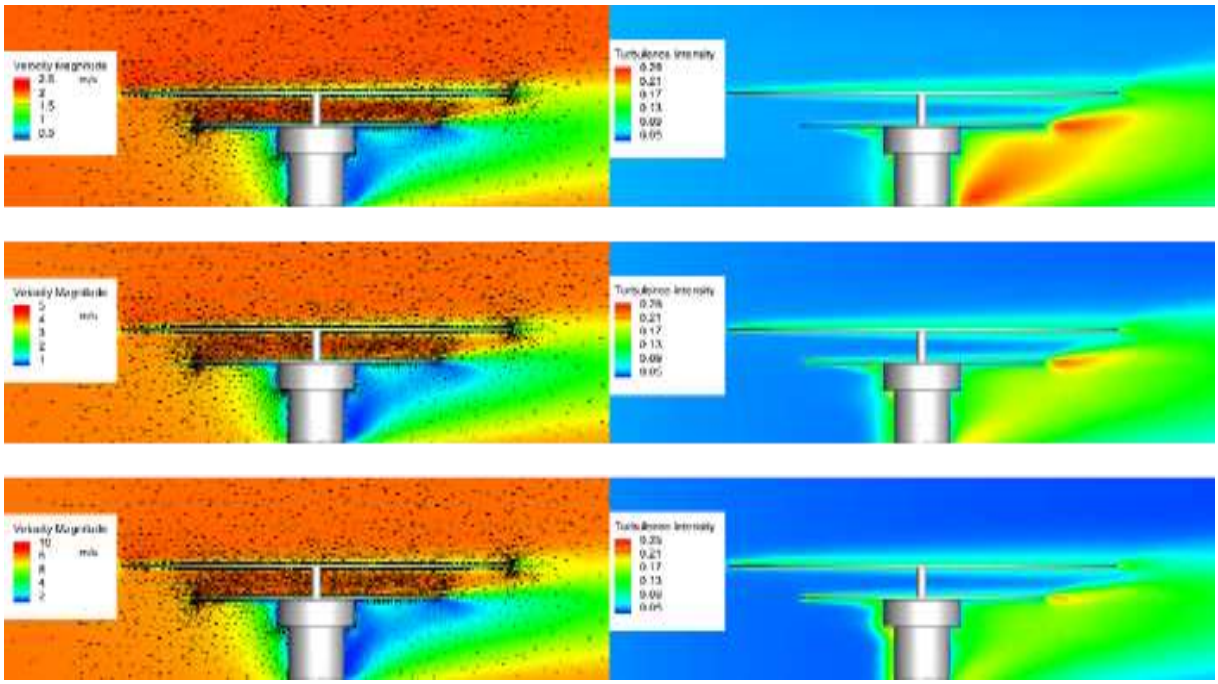

Figure 11: Flat plate Sampler: Velocity magnitude and turbulence intensity at wind speed 2 m/s (top), Flat plate Sampler: Velocity magnitude and turbulence intensity at wind speed 4 m/s (middle), Flat plate Sampler: Velocity magnitude and turbulence intensity at wind speed 8 m/s (bottom).

8.3.1.2 Sigma 2 Sampler

The cross section of the velocities for the Sigma-2 are shown for the 4 m/s case in Figure 12. Apparently the velocity magnitude inside the sampler is much smaller than outside. In the

vertical settling tube, the turbulence intensity is low, justifying the idea of Stokes settling inside. Owing to the open, but bulky geometry, there is a flow into the interior at the back. The highest velocities and turbulence intensities are found at the sharp edges at the top and bottom of the sampler.

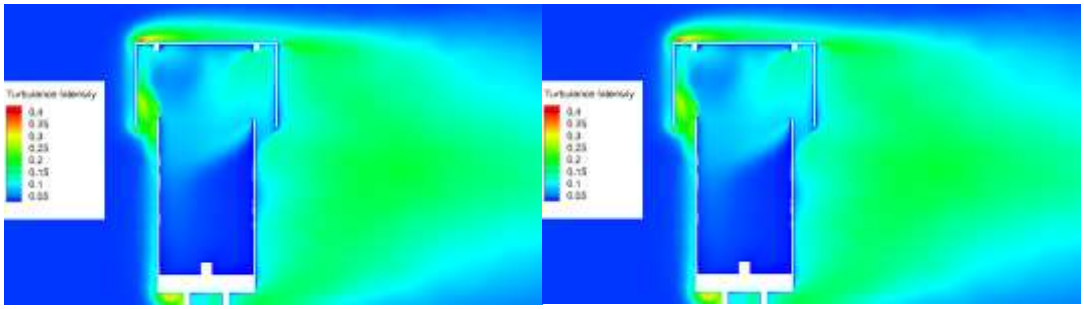

Figure 12: Sigma-2 Sampler: Velocity magnitude and turbulence intensity at wind speed 4 m/s.

8.3.1.3 MWAC sampler

Figure 13 shows the cross section of the velocities for the MWAC in the 4 m/s case. Furthermore, the velocity field and the velocity vectors in the cross sections across and along the inlet tube are shown in Figure 14. In the tubes the typical pipe flow is formed. In the figures showing the cross sections along the inlet tube a symmetrical flow over the pipe cross section is visible. Finally, Figure 15 shows the mean flow velocity in the MWAC tube is shown as a function of the outside velocity for the three cases. The fitting curve shows that the mean velocity in the pipe increases linearly with the external velocity.

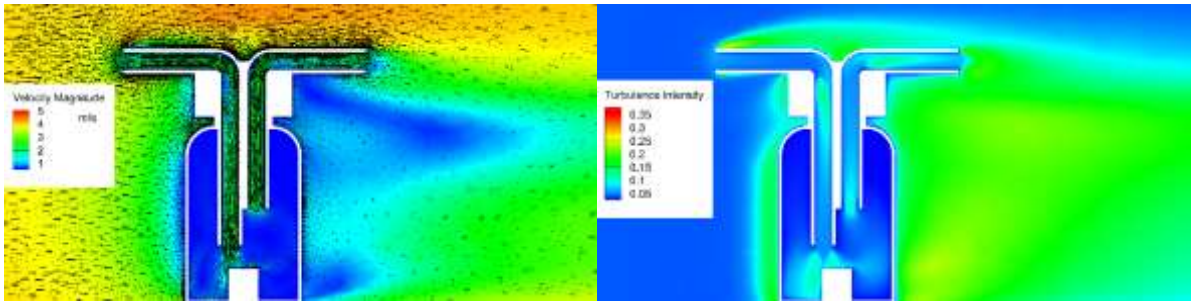

Figure 13: MWAC Sampler: Velocity magnitude and turbulence intensity at wind speed 4 m/s.

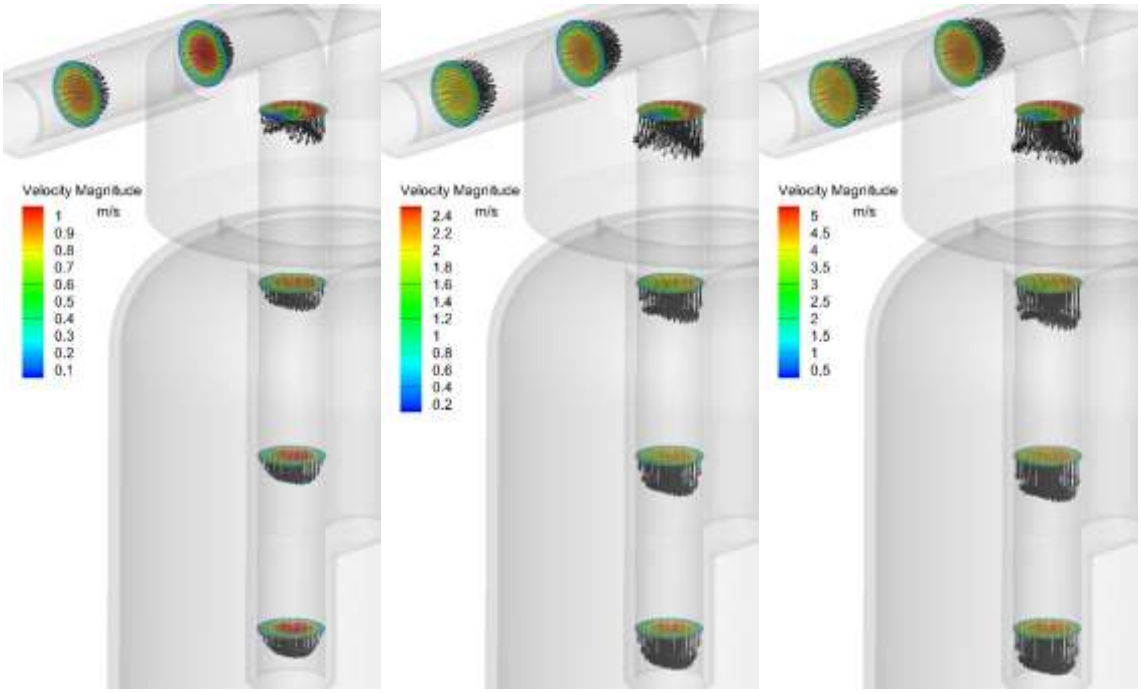

Figure 14: Velocity vectors at 2, 4 and 8 m/s (cross sections across and along the inlet tube).

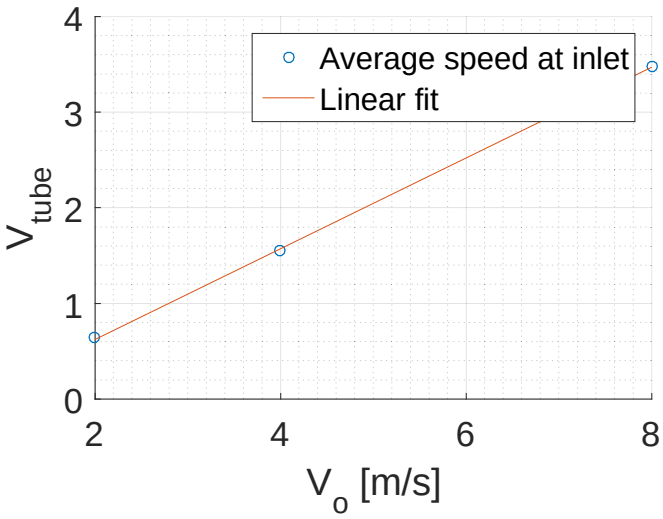

Figure 15: Mean flow velocity (V_{tube}) in the MWAC tube as a function of the outside velocity (V_O). Fitting curve: $V_{tube} = 0.47V_0 - 0.33$ for the range 2 – 8 m/s.

9 Results and Discussion- Methodical aspects

9.1 Field Measurements

9.1.1 Mass deposition rate comparison

Mineral dust was the dominating particle type during this campaign, consisting of different classes of silicates, quartz-like, calcite-like, dolomite-like and gypsum-like particles similar to previous findings for this location (Kandler et al., 2007). Therefore, hygroscopicity was not taken into account, as due to the mostly non-hygroscopic compounds and the moderate humidities, their impact was rated low. Details on the composition is reported in chapter 10.

The mass and number deposition rates (given per unit time and sample surface area) along with daily average temperature and wind speed are presented as daily values. Details for all days and all samplers are given in Table A 1, Table A 2, Table A 3, Table A 4 in the Appendix. All data shown in this section are calculated from SEM measurements. Particle sizes are reported as aerodynamic diameter, if not otherwise stated.

Figure 16 shows as example mass deposition rates for different samplers during a dust event and a non-dust event day. For all samplers, the mass deposition rate size distributions peaked in the 8-16 µm diameter interval. This result is in support of the conclusion that atmospheric dry deposition is dominated by coarse particles owing to their high deposition velocities (Davidson et al., 1985; Holsen et al., 1991). There is a considerable difference among different samplers affecting mainly the size range with the highest mass deposition rates, whereas the difference is small for smaller particles. MWAC and BSNE – both horizontal flux samplers – collect coarser material than the Flat plate and Sigma-2 samplers, which in contrary measure the vertical flux. In particular, the MWAC sampler exhibits considerably higher coarse particle mass deposition rates, probably owing to its impactor-like design.

Table 2: The campaign maximum and minimum and median mass deposition rates measured by the samplers.

Samplers	**Maximum deposition rate** (mg/ (m^2d))	**Minimum deposition rate** (mg/ (m^2d))	**Median deposition rate** (mg/ (m^2d))
MWAC	1240	0.6	4.8
BSNE	310	0.2	3.1
Flat plate	80	2.0	1.1
Sigma-2	117	1.9	1.1

As a consequence the vertical flux instruments collect much less material than the horizontal flux ones (Table 2), which is in accordance with previous findings (Goossens, 2008). In the present study, horizontal to vertical flux mass ratio is approximately between 2.8 and 4.4 (with single size intervals ranging between 2 and 50), while Goossens (2008) reported it to be in between 50 and 160. This difference in the ratio might come from the different approaches. Goossens (2008) used water as a deposition surface while in our study I used a SEM sampling substrate. Furthermore, from Figure 16, it can be clearly seen that that there is a strong variation in mass deposition rates between dust event days and non-dust event days (full dataset is shown in Figure 17). Generally, the temporal variation is higher than the difference between the samplers so a strict comparison between this and the previous study can't be done.

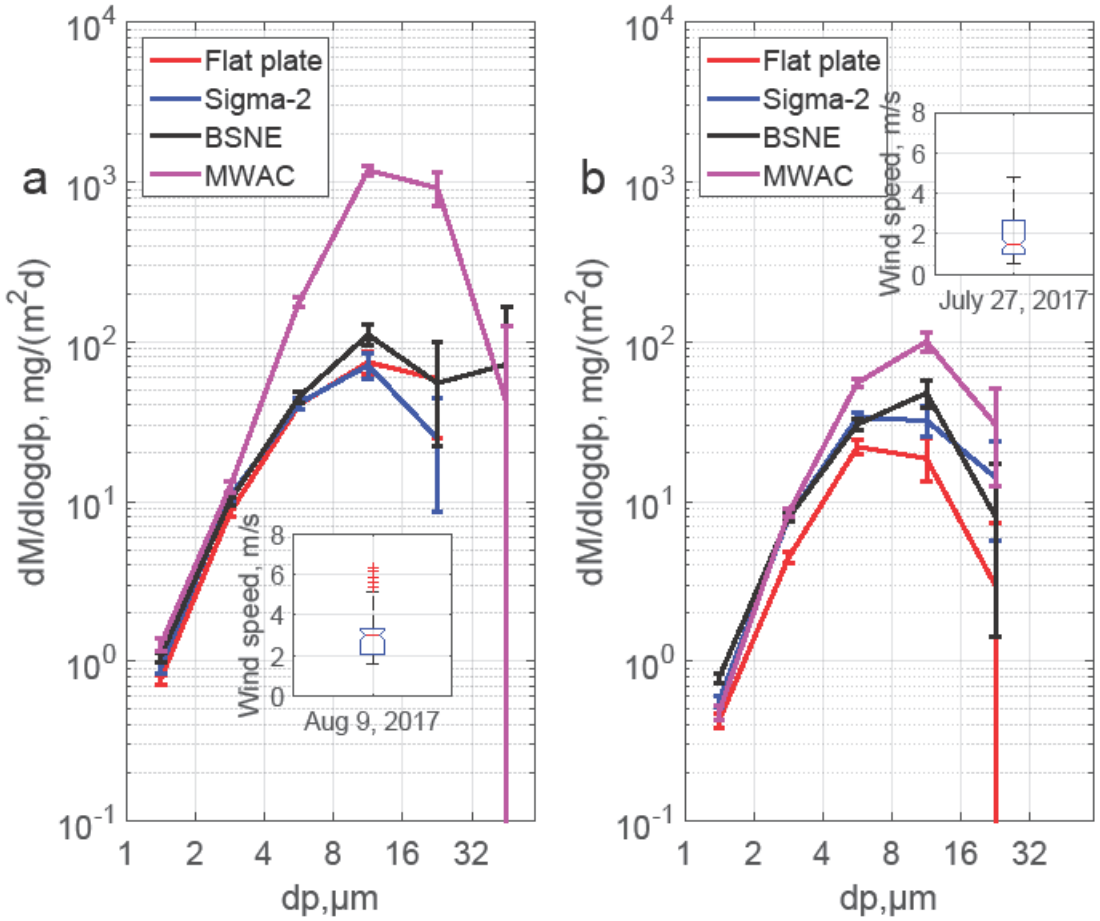

Figure 16: Size resolved mass deposition rate measured by different passive samplers: a) dust event day; b) non-dust event day. Data are derived from SEM measurements. The bars show the central 95% confidence interval of the daily variation. The inserts show box plots for the wind speed distribution based on 30-min intervals.

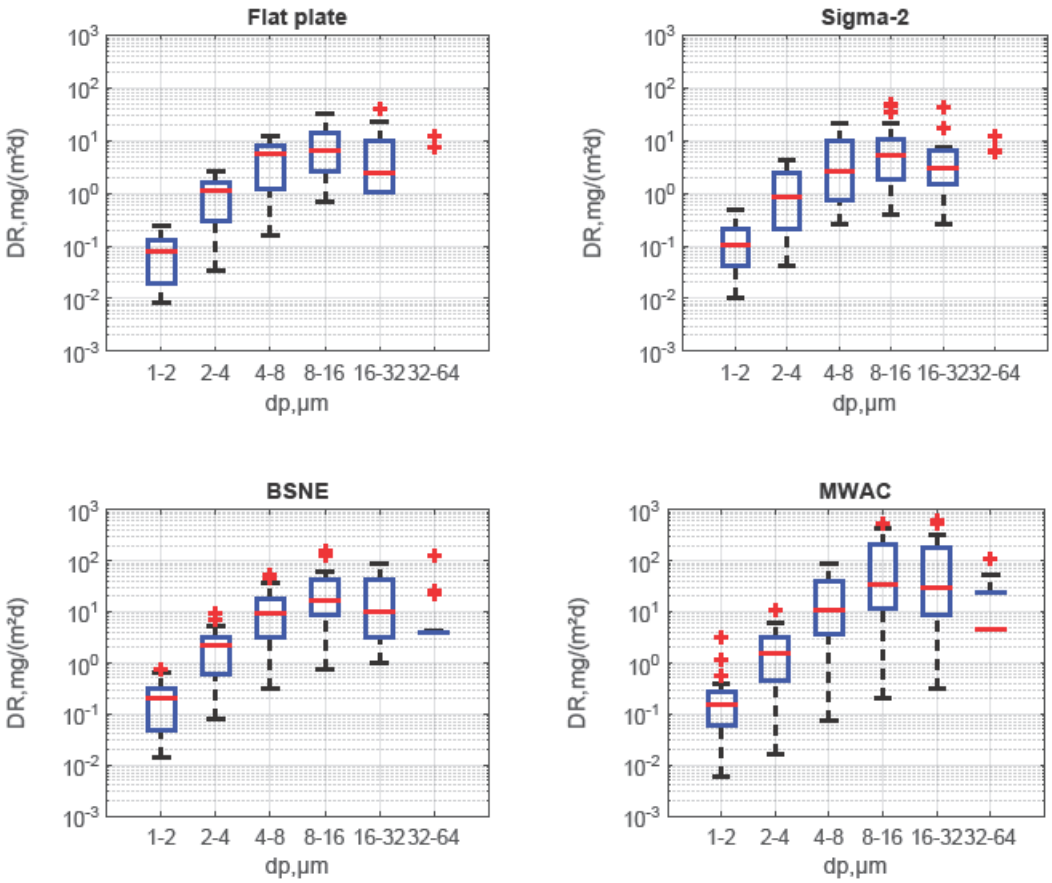

Figure 17: Box-plots of size resolved deposition rate (campaign data; Flat plate, Sigma-2, MWAC and BSNE samplers). On each blue box, the central mark is the median, the edges of the box are the 25th and 75th percentiles. The red vertical lines show the standard deviation. The median, percentiles and standard deviations shown there correspond to the variability of the whole campaign for each instrument and bin.

From the structure of the deposition models, a wind speed dependency for the deposition velocity should be expected. The average wind speed during the campaign was about 3.5 m/s with the lowest daily median around 1.5 m/s and the highest 7 m/s. A daily box-plot of 30-min averaged wind speed at Izaña is shown in Figure 18.

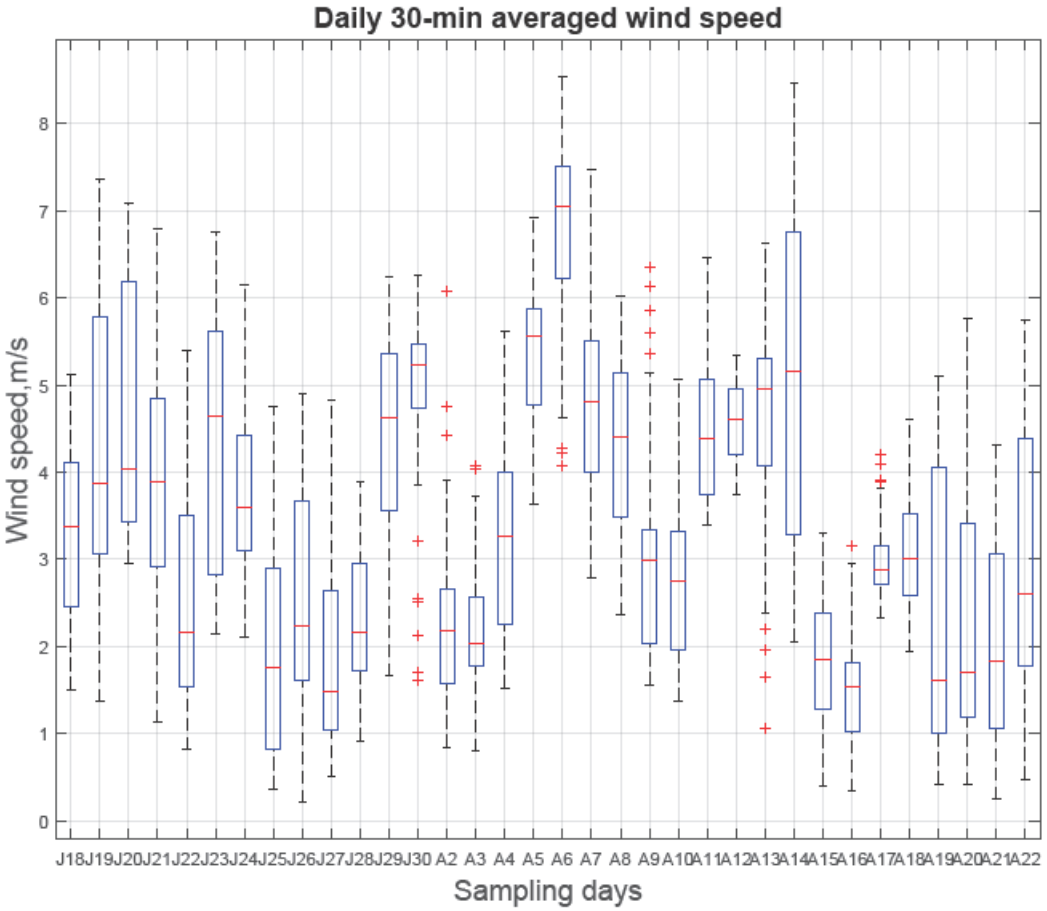

Figure 18: Daily box-plots of 30-min averaged wind speed observed at Izaña Global Atmospheric watch Observatorio from 18/July/2017 to 23/August/2017 (e.g., each day was divided in 30-minute interval averages and then the mean and standard deviation was calculated from this data). On each blue box, the central mark is the median, the edges of the box are the 25th and 75th percentiles. The black vertical lines show the standard deviation (J=July, A=August).

Figure 19 shows the mass deposition rate ratio of MWAC, BSNE and Flat plate to Sigma-2 as a function of wind speed. The Sigma-2 sampler was chosen for comparison, as due to its settling tube design, it is expected to have the least wind sensitivity. The results show highly scattered values. The collection efficiency of MWAC for large particles has an increasing tendency in comparison to Sigma-2 slightly with increasing wind speed, while there is barely a trend visible for the BSNE. Both – being horizontal flux samplers – collect considerably more material than the Sigma-2. For the Flat plate, the deposition velocity in relation to the Sigma-2 has a weak decreasing trend for higher wind speeds, but generally, the deposition speed is similar. Overall, the relation of Sigma-2 to BSNE shows the closest agreement, while the scatter is higher for the other combinations. For sake of completeness, the same comparison for the other samplers is shown in Figure 20, Figure 21, Figure 22, Figure 23, Figure 24, Figure 25, Figure 26, Figure 27 and Figure 28.

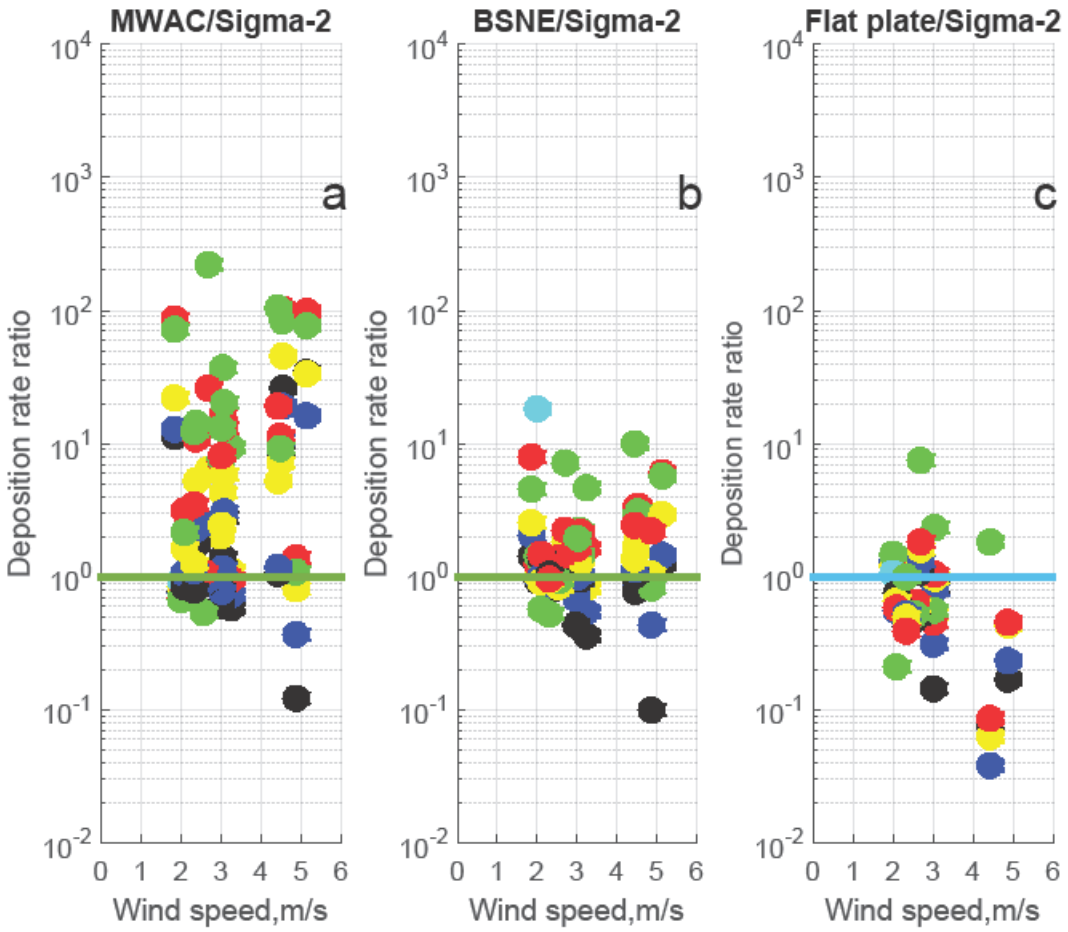

Figure 19: Deposition rate ratio as a function of wind speed for different days (MWAC/ Sigma-2 (a), BSNE/Sigma-2 (b) and BSNE/ Sigma-2 (c)). Different colors represent deposition rate measured in different size intervals (black: 1-2 µm; blue: 2-4 µm; yellow: 4-8 µm; red: 8-16 µm; green: 16-32 µm; cyan: 32-64 µm).

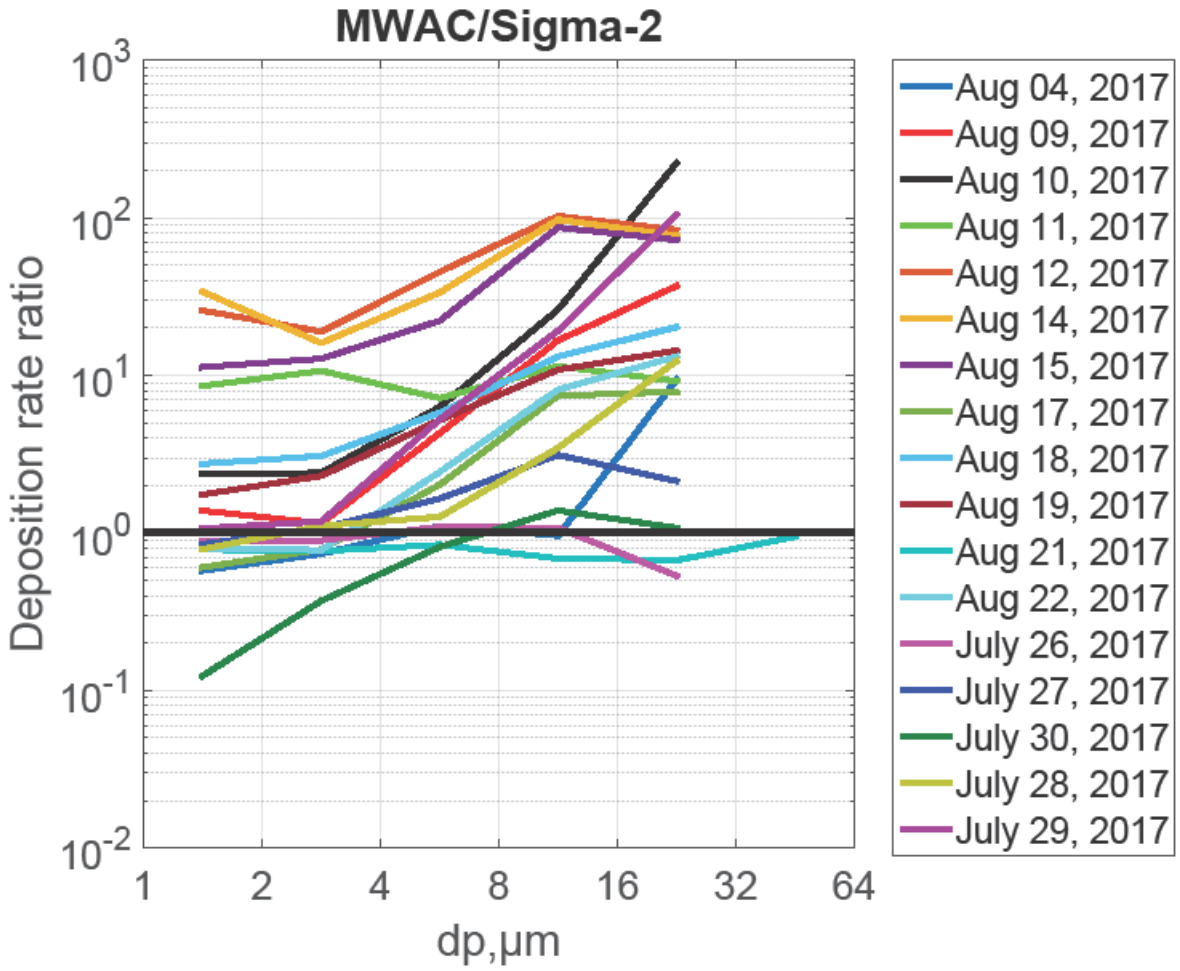

Figure 20: Deposition rate ratio as a function of particle size (MWAC/Sigma-2).

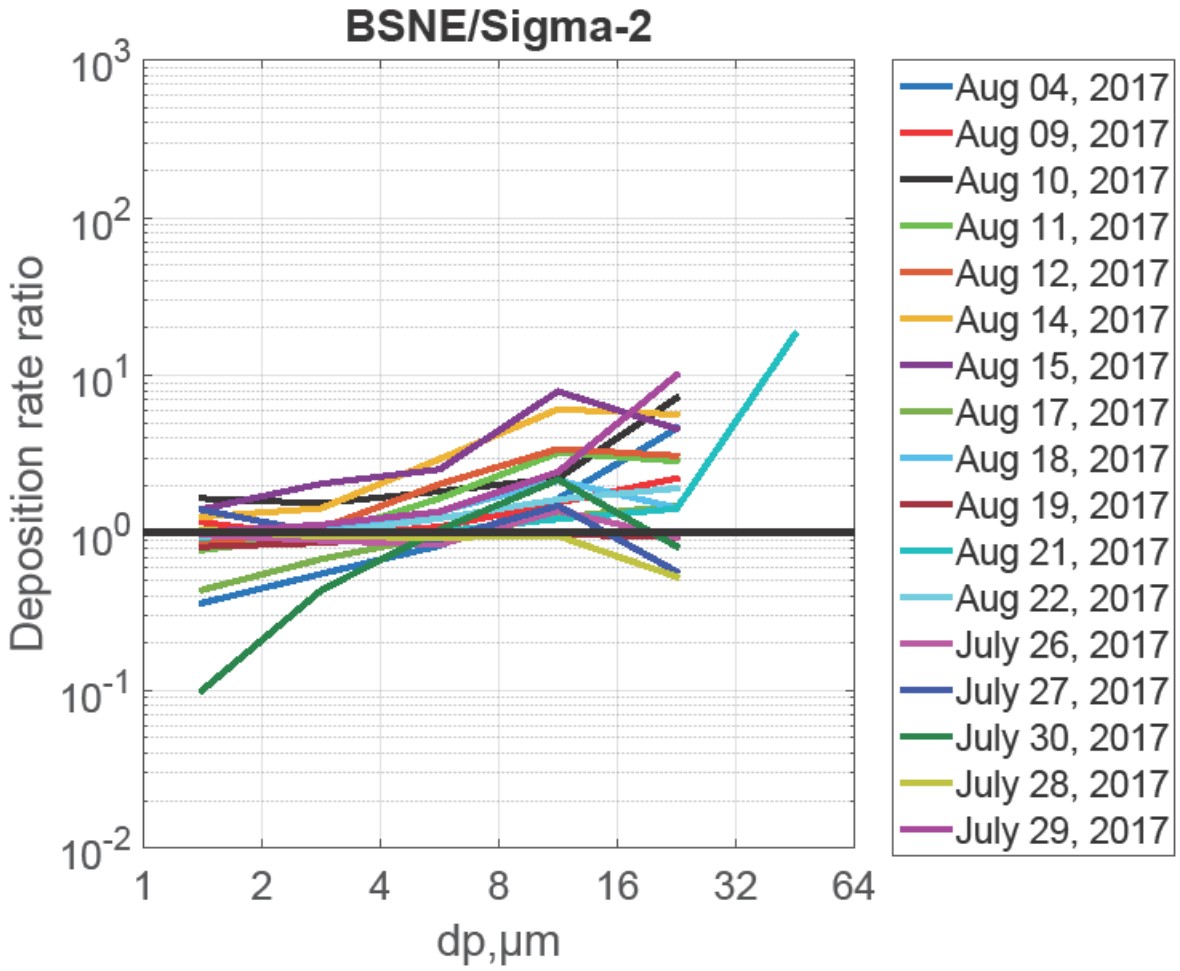

Figure 21: Deposition rate ratio as a function of particle size (BSNE/Sigma-2).

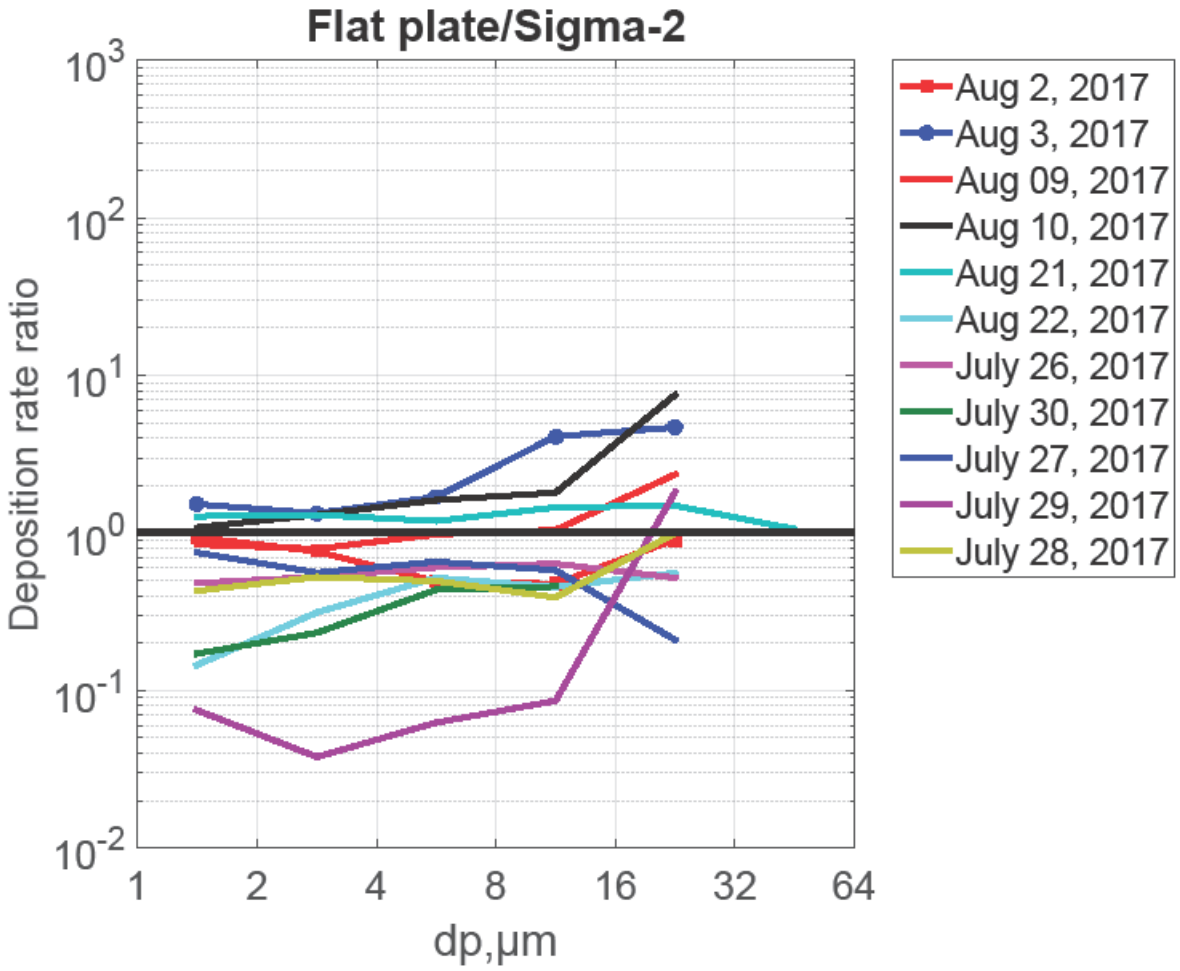

Figure 22: Deposition rate ratio as a function of particle size (Flat plate/Sigma-2).

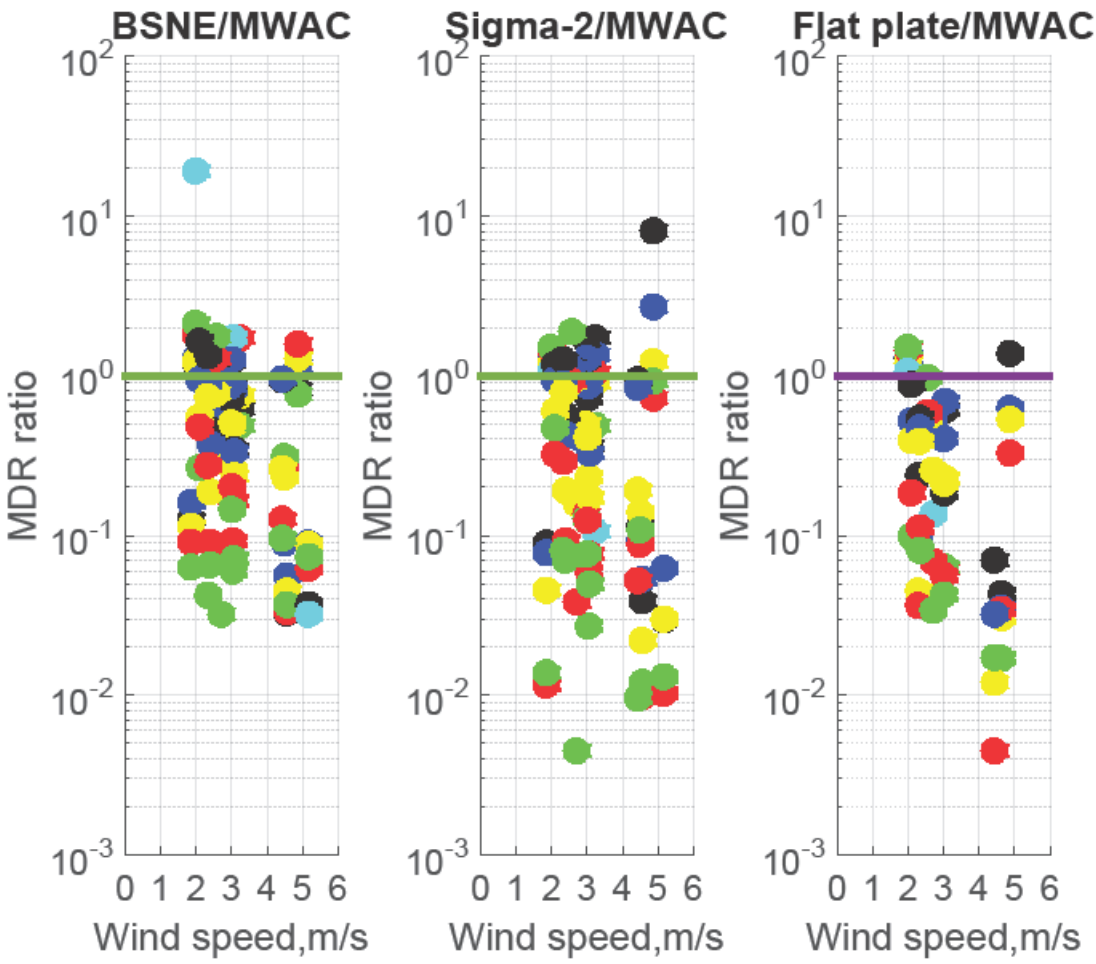

Figure 23: Mass deposition rate (MDR) ratio as a function of wind speed for different measurement days. Different colors represent deposition rates in different size intervals (black: 1-2 µm; blue: 2-4 µm; yellow: 4-8 µm; red: 8-16 µm; green: 16-32 µm; cyan: 32-64 µm).

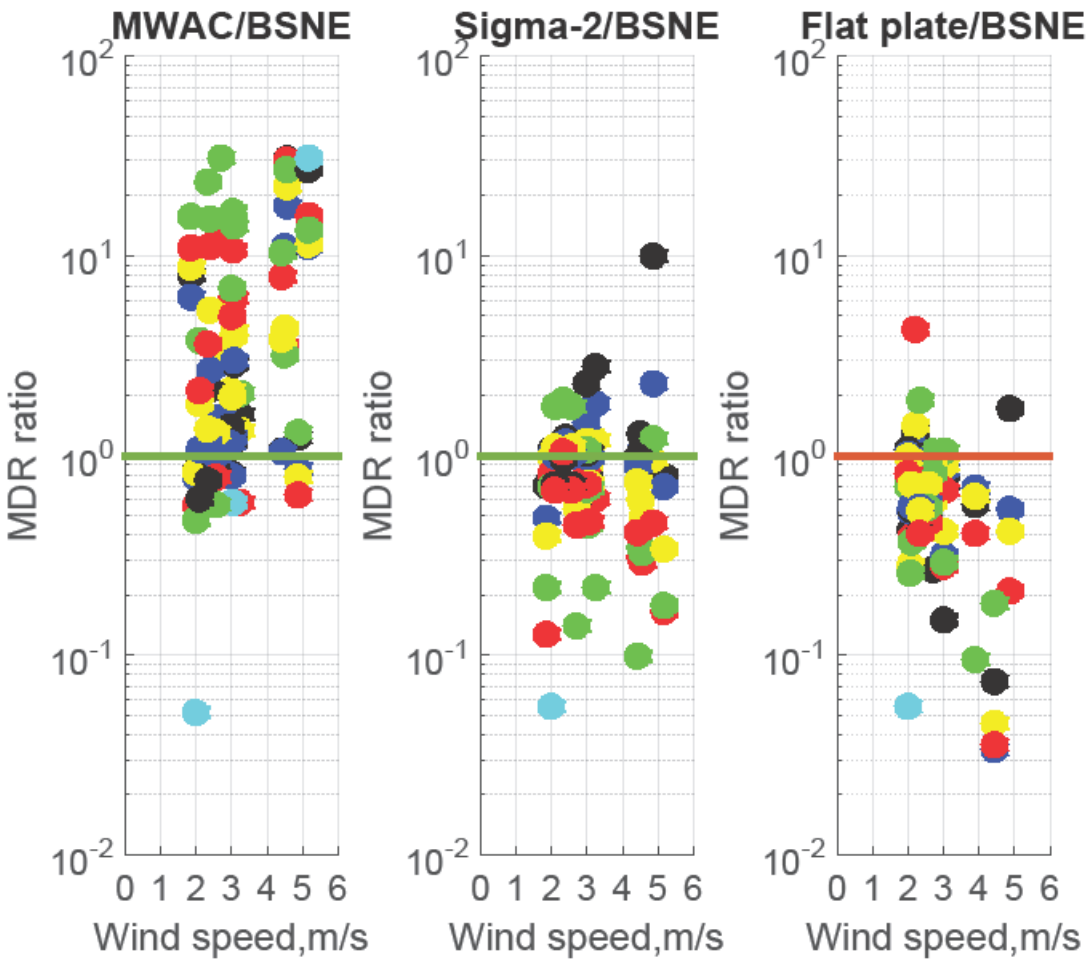

Figure 24: Mass deposition rate (MDR) ratio as a function of wind speed for different measurement days. Different colors represent deposition rates in different size intervals (black: 1-2 µm; blue: 2-4 µm; yellow: 4-8 µm; red: 8-16 µm; green: 16-32 µm; cyan: 32-64 µm).

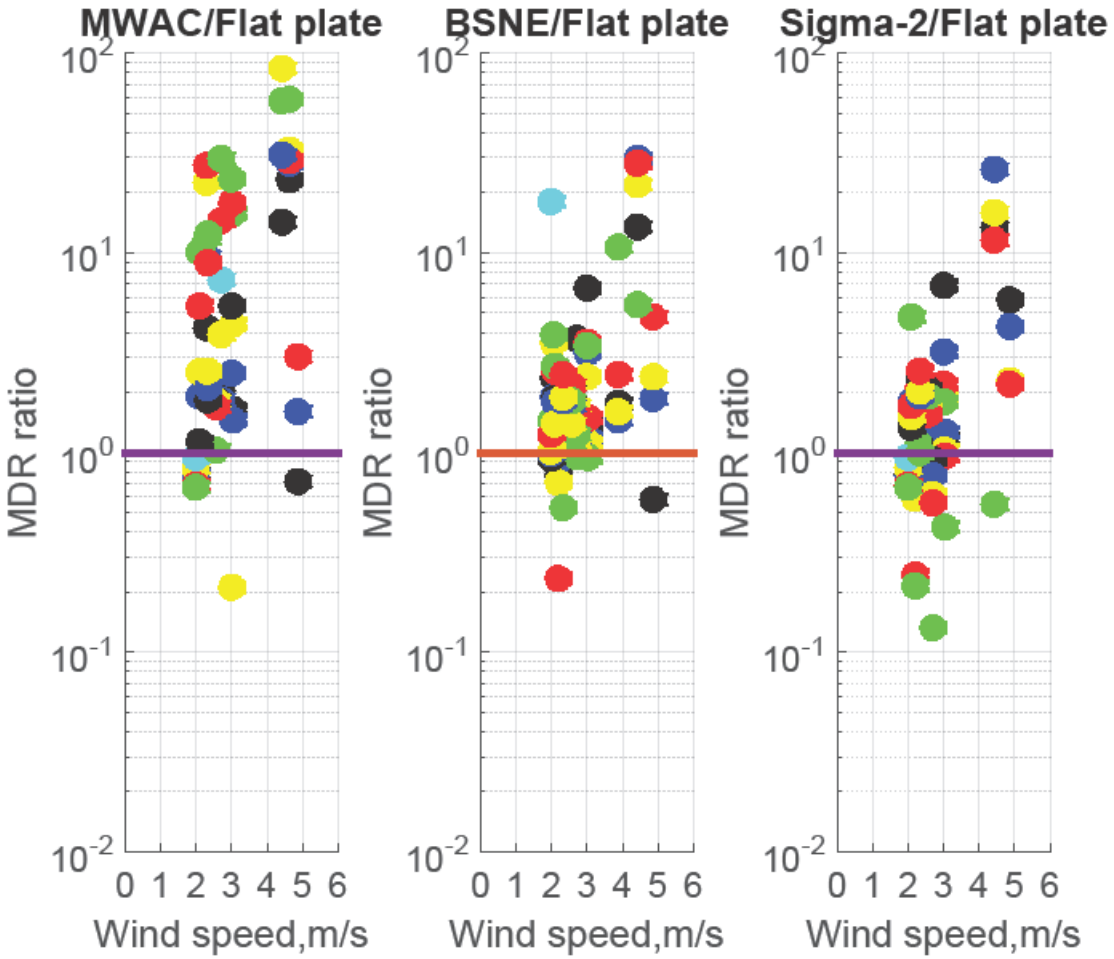

Figure 25: Mass deposition rate (MDR) ratio as a function of wind speed for different measurement days. Different colors represent deposition rates in different size intervals (black: 1-2 µm; blue: 2-4 µm; yellow: 4-8 µm; red: 8-16 µm; green: 16-32 µm; cyan: 32-64 µm).

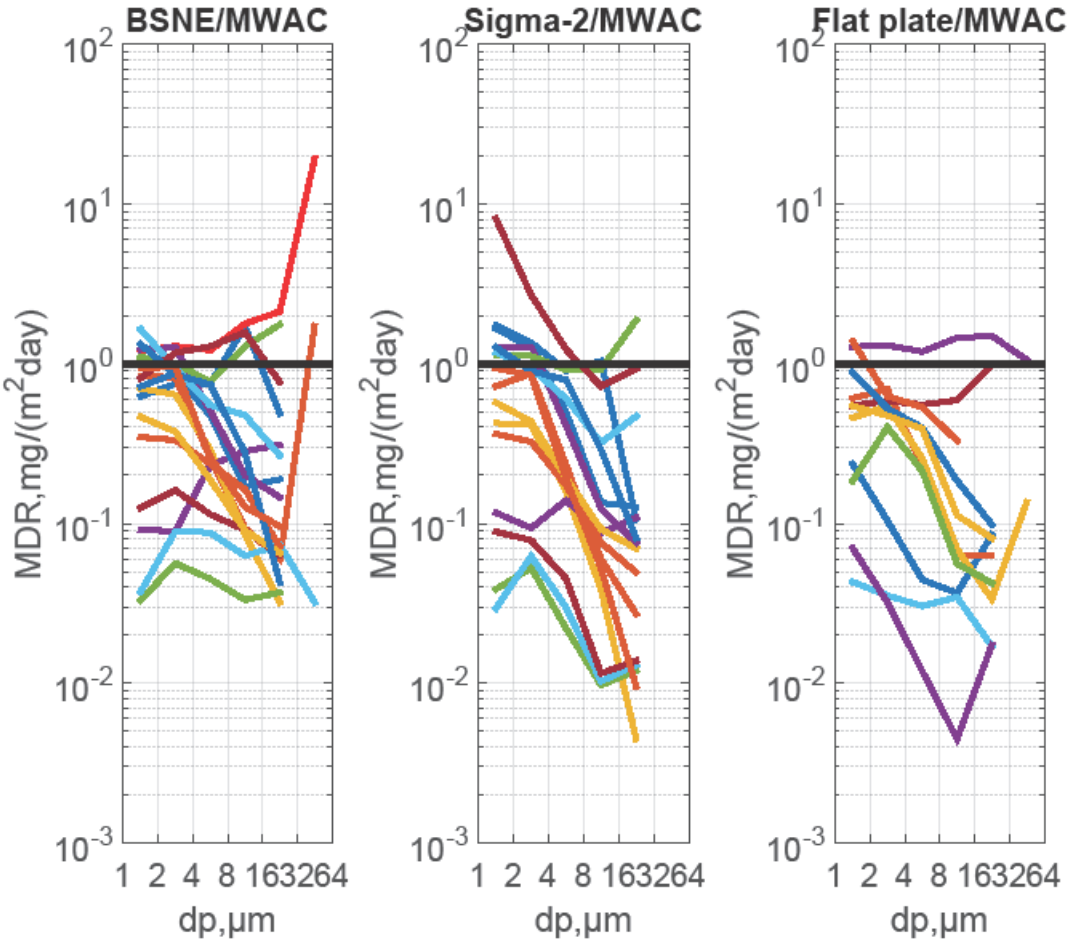

Figure 26: Mass deposition rate (MDR) ratio as a function of particle size (different colors show different measurement days).

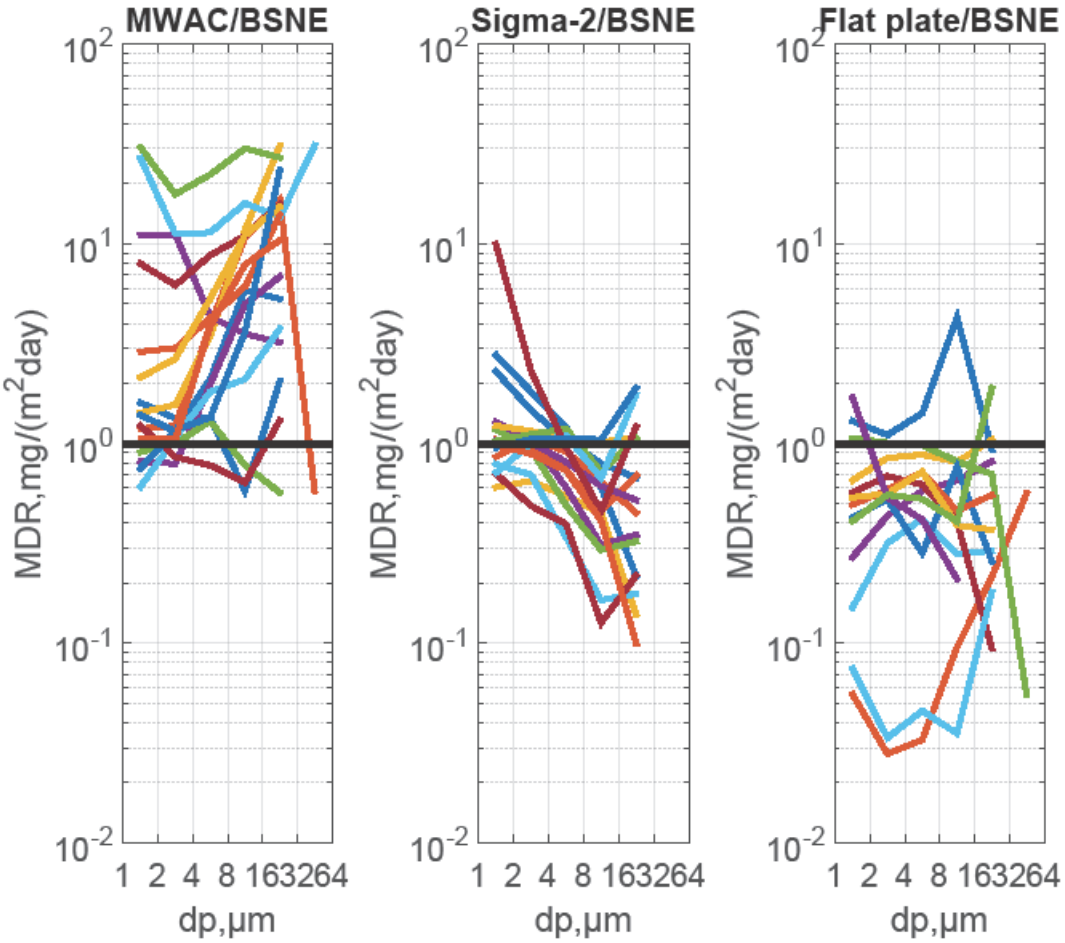

Figure 27: Mass deposition rate (MDR) ratio as a function of particle size (different colors show different measurement days).

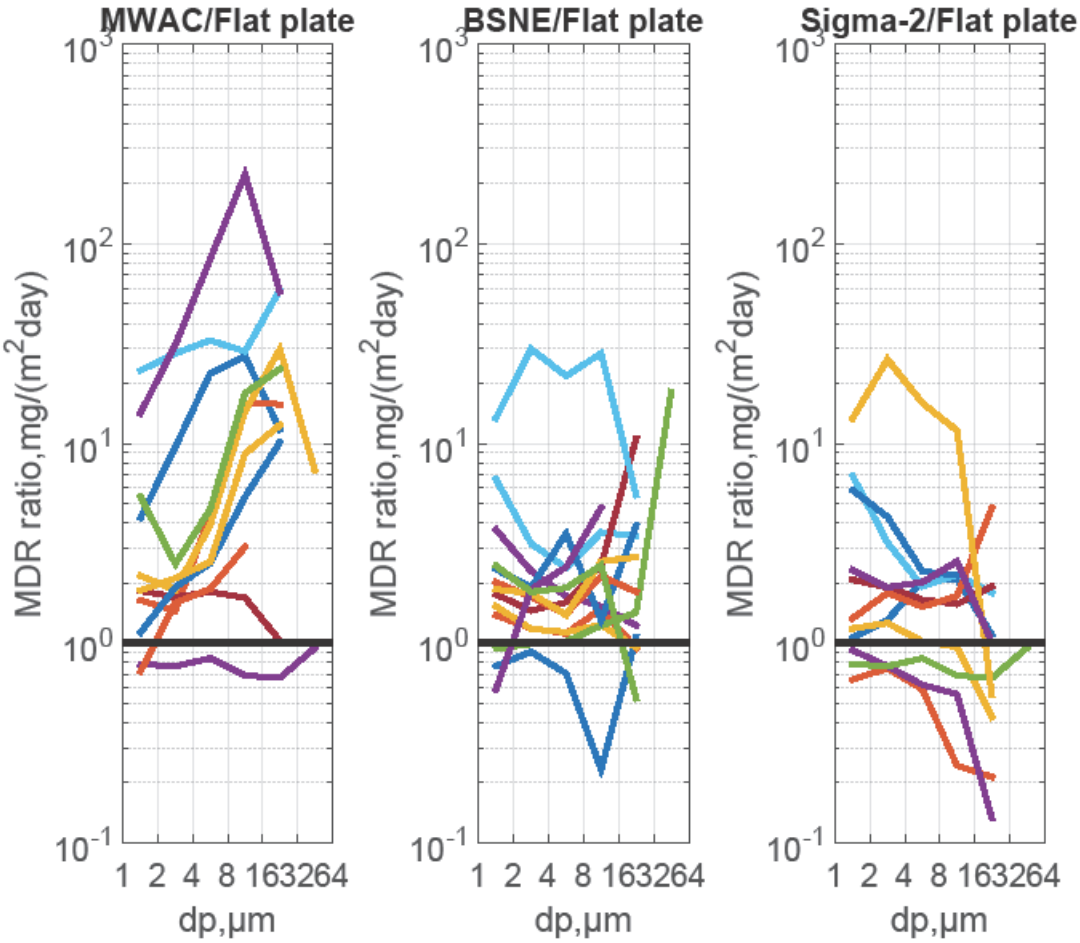

Figure 28: Mass deposition rate (MDR) ratio as a function of particle size (different colors show different measurement days).

While without a true reference technique the absolute deposition velocities can't be determined, their ratio between different instruments can be compared theoretically and by measurement. The deposition velocity ratios for a pair of different samplers are identical to the deposition rate ratios obtained from the corresponding measurements (eq. (7)), as long as the sampling time and the aerosol concentration are the same; the latter condition is achieved by the close and parallel sampling. Therefore, the experimentally determined ratios can now be compared to the deposition velocity ratios derived from the theoretical considerations. Figure 29 shows the according comparison. Note that this consideration allows for the assessment of relative model performance and sampler efficiency, but lacking a 'true' reference, it does not allow for determining the most accurate sampler.

While for BSNE and Sigma-2 observation and model fit comparatively well, the deposition velocity is misestimated for the Flat plate/Sigma-2 pairing for all particle sizes (overestimate for Flat plate deposition velocity or/and underestimate for Sigma-2). For MWAC/Sigma-2,

there is a clear size dependency, indicating that probably the impactor model overestimates the deposition velocity; the latter might be due to unaccounted particle losses (e.g., inlet efficiency). MWAC, BSNE and Sigma-2 agree with respect to deposition velocity better based on the measurement data than predicted by the theory. It may be connected to the non-stationarity of the atmosphere, which is not accounted for by the models, i.e. the permanent wind speed fluctuations smoothing out detail differences of a stationary flow. The Flat plate sampler, however, has a lower-than-predicted deposition velocity.

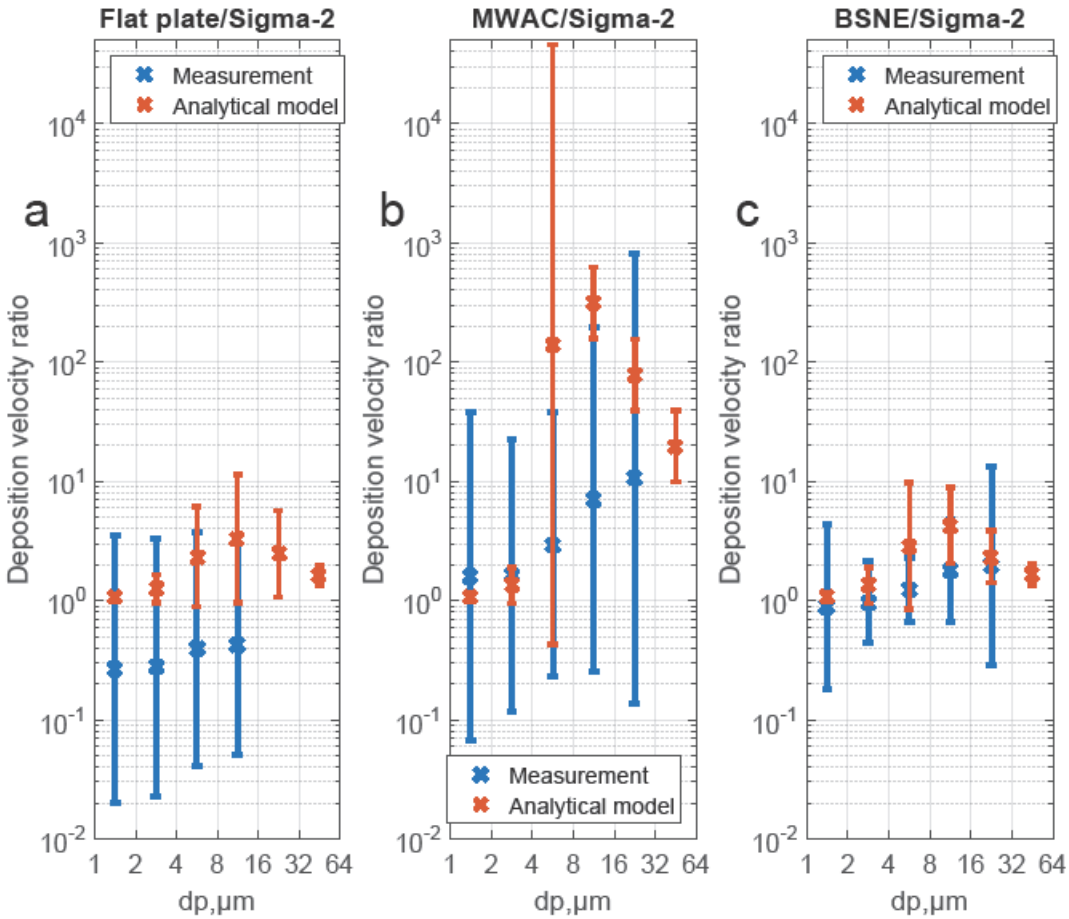

Figure 29: Comparison of geometric mean ratio of deposition velocities for different sampler pairs derived from measured deposition rates (blue) and from corresponding deposition models (orange). (a) Flat plate/Sigma-2; (b) MWAC/Sigma-2; (c) BSNE/Sigma-2. The bars show the central 95% confidence interval of the daily variation. According deposition models are listed in Table 1.

9.1.2 Dependence of PM_{10} dust deposition on atmospheric concentration and wind speed

Figure 30 and Table 3 display for the approximate PM_{10} size range the correlation between number deposition rates, atmospheric particle number concentrations measured by OPC and the wind speed for different samples. For this consideration, only the overlapping size range – 1-10 µm aerodynamic diameter – was used. As expected, there is in all cases a positive correlation between concentrations and number deposition rates (see Figure 30a). In particular, for the BSNE and the Sigma-2, robust correlations with a trend to underestimation at higher concentrations exist. While the models predict a positive correlation of wind speed and deposition rate, this is not observed in the measurements. E.g., the table does not show a linear correlation since the r^2 values are not close to 1 for the first two samplers (particularly the MWAC). Instead, a non-significant anti-correlation can be observed, if at all (e.g., for Flat plate; r^2: 0.319, p-value = 0.070, slope=-0.261) (see Figure 30b), indicating a cross-influence of wind speed and concentration. E.g. higher concentrations of dust aerosol particles might be meteorologically linked to lower wind speeds due to a different transport situation. Such a general behavior was observed previously for example by different techniques for a dust transport region (Kandler et al., 2011). An ambiguous wind-dependency has been reported for other places (Xu et al., 2016). In this study, the main driver of the deposition rate is obviously the dust concentration.

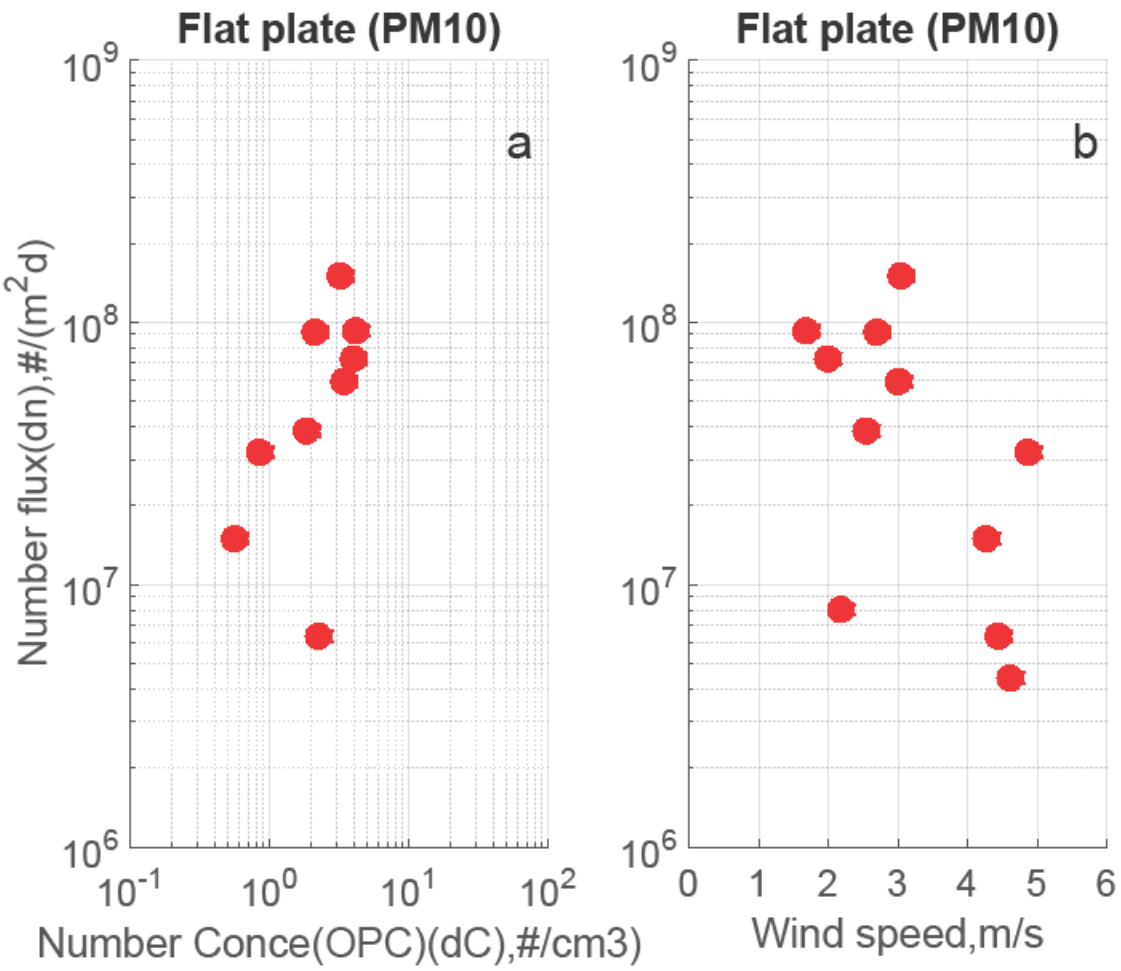

Figure 30: Connection of deposition flux, OPC concentration, and meteorological factors (wind speed). (a) Number deposition rate of particles smaller than 10 µm estimated aerodynamic diameter observed with the flat plate sampler versus number concentration of PM_{10} observed with the OPC. (b) Number deposition rate of particles smaller than 10 µm estimated aerodynamic diameter observed with the Flat plate sampler versus the average wind speed of the collection period.

Table 3: Summary of the regression analysis for the correlations between the dust deposition rate and the atmospheric concentrations (**PM_{10}** size range; measured by the OPC), and for the correlations between the dust deposition rates and the wind speeds. Significant relationships are shown in bold.

	Deposition rate vs concentration			**Deposition rate vs wind speed**		
	r^2	p-value	slope (m/d)	r^2	p-value	Slope ($1.16*10^5/(m^3)$)
Flat plate	0.600	0.0052	0.492	0.319	0.070	-0.261
MWAC	0.155	0.335	0.146	0.308	0.153	-0.157
BSNE	**0.937**	**$1.00*10^{-6}$**	**0.832**	0.017	0.706	-0.052
Sigma-2	**0.925**	**$3.39*10^{-5}$**	**0.725**	0.0125	0.775	-0.069

In a second step is was tested, whether the application of each sampler's assigned deposition model can increase the correlation between the measurements by the deposition samplers and the OPC observations, i.e. whether the meteorological parameters accounted for in the models can decrease the deviation. Therefore, in analogy to the previous correlation, the concentrations modeled from each sampler's SEM data were correlated with the OPC data for the size range between 1 and 10 µm in particle diameter (see Table 4). However, no increase in correlation quality is observed, indicating that – like already observed from the varying ratio calculations above – the deposition models fail to describe the deposition behavior in detail.

From the correlation relations in Table 3, it can be learned that MWAC is least suitable for estimating PM_{10}, which fully agrees well with previous studies (Mendez et al., 2016). However, the correlation analysis here shows that BSNE is actually a suitable instrument for a PM_{10} estimation, which is in contrast to the wind-tunnel observation of Mendez et al. (2016). This discrepancy might be owed to the different approaches. While in the previous work the loss of concentration from the passing aerosol was measured, in this study a gain of deposition was investigated. As a result, for lower deposition velocities (discussed below), the former approach will yield high uncertainties. Similar to BSNE, Flat plate and Sigma-2 appear good estimators for PM_{10}, which is in accordance with previous studies (Dietze et al., 2006).

Table 4: Summary of regression analysis for correlation between calculated dust concentration and OPC measurement.

	Calculated concentration vs OPC measured concentration		
Sampler	r^2	p-value	slope
Flat plate	0.449	0.0241	0.4084
MWAC	0.243	0.214	0.1654
BSNE	0.968	4.70E-08	0.8046
Sigma-2	0.794	0.00127	0.6851

9.1.3 Size-resolved apparent deposition velocity in the PM_{10} size range

Figure 31 displays the apparent deposition velocity (calculated as the ratio of the number deposition rate to the concentration of the OPC) as a function of the wind speed. Obviously, also here there is no clear trend. The apparent deposition velocities range between $2*10^{-4}$-10^{-1} m/s. As can be clearly seen from the plot, the effect of wind speed on deposition velocity is negligible, as indicated in Table 3. While this is in contradiction to the models, one has to keep in mind that the (a) the observed wind speeds are comparatively low here, and (b) the considered size range is not the one most affected by the wind speed. An effect of the wind speed might therefore be much stronger at higher wind speeds and for larger particles.

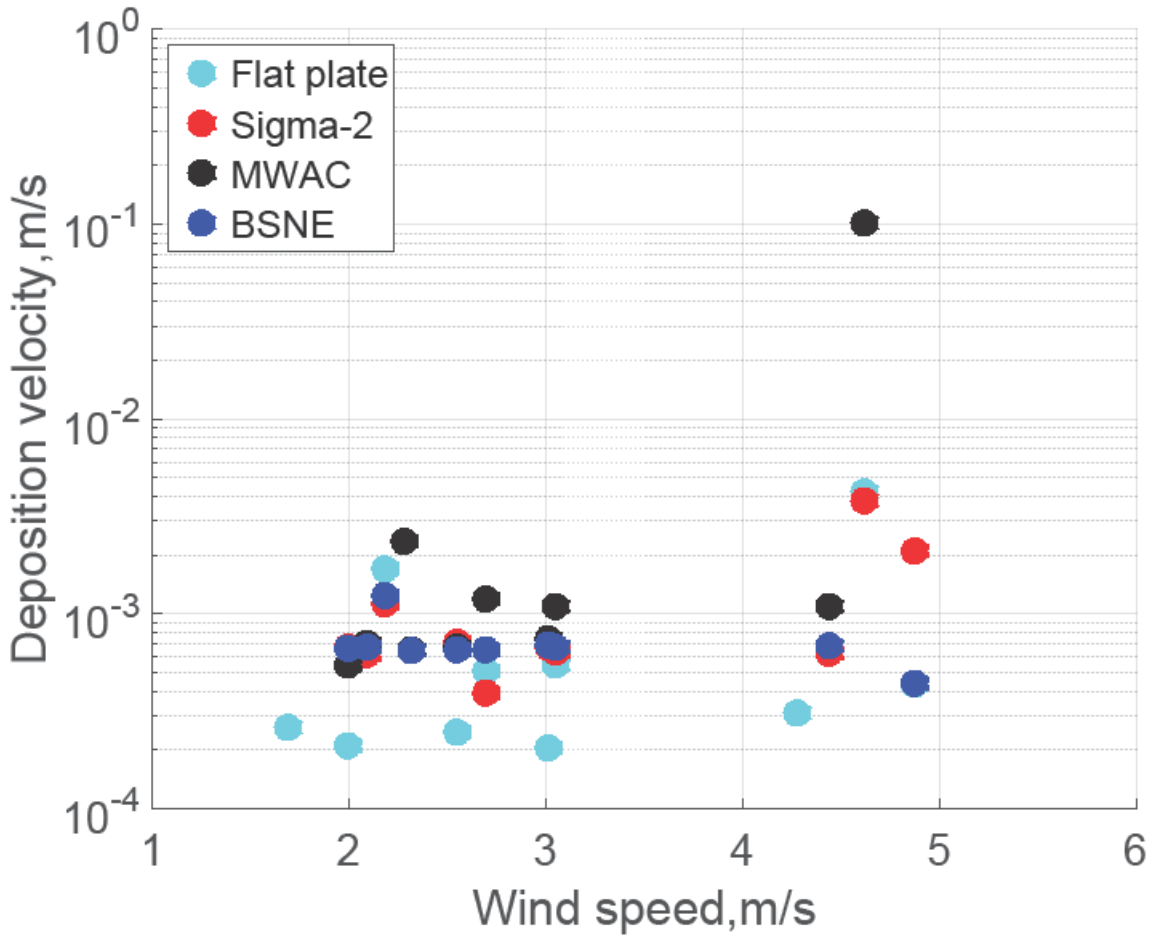

Figure 31: Apparent deposition velocity: ratio of number deposition rate determined from SEM measurements to the number concentration observed by the OPC as a function of wind speed. For the consideration, only the overlapping size range (approximately 1-10 µm) was used.

9.1.4 Atmospheric mass concentrations derived from deposition rates

9.1.4.1 Consistency between samplers and corresponding models

Figure 32 compares a mass deposition rate size distribution with the according concentrations derived by the modeled deposition velocities. Calculating the mass concentrations from different passive samplers with different models leads in most cases to a better agreement between the measurements, taking into account the statistical uncertainties (see Figure 33). This indicates that the deposition velocity models selected for the samplers are generally suitable, despite the deviations in single cases.

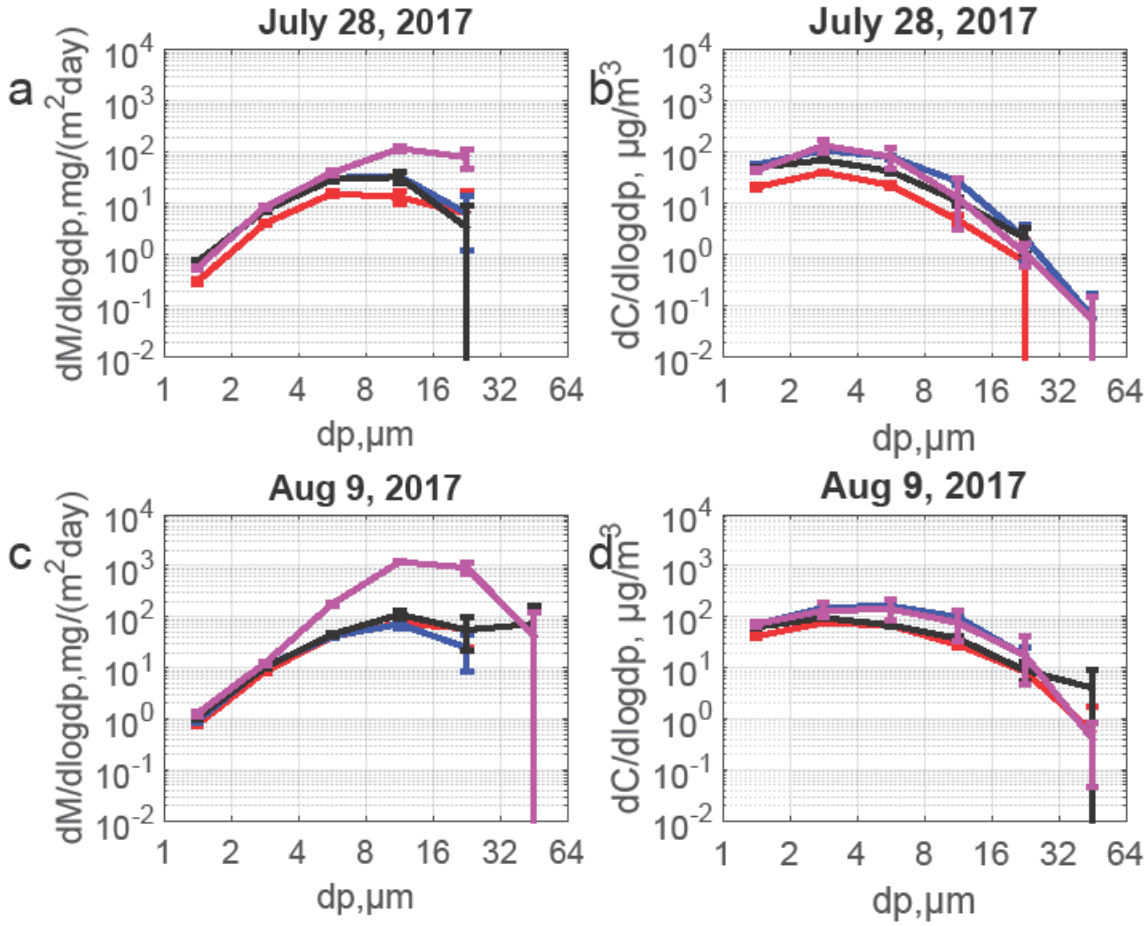

Figure 32: Comparing different samplers with respect to (a, c) dust mass deposition rates and (b, d) dust mass concentrations calculated from application of the corresponding model as a function of particle size. Different colors indicate different samplers (red: Flat plate; blue: Sigma-2; black: BSNE and magenta: MWAC). The bars show the central 95% confidence interval of the daily variation. According deposition models for concentration calculation are given in Table 1.

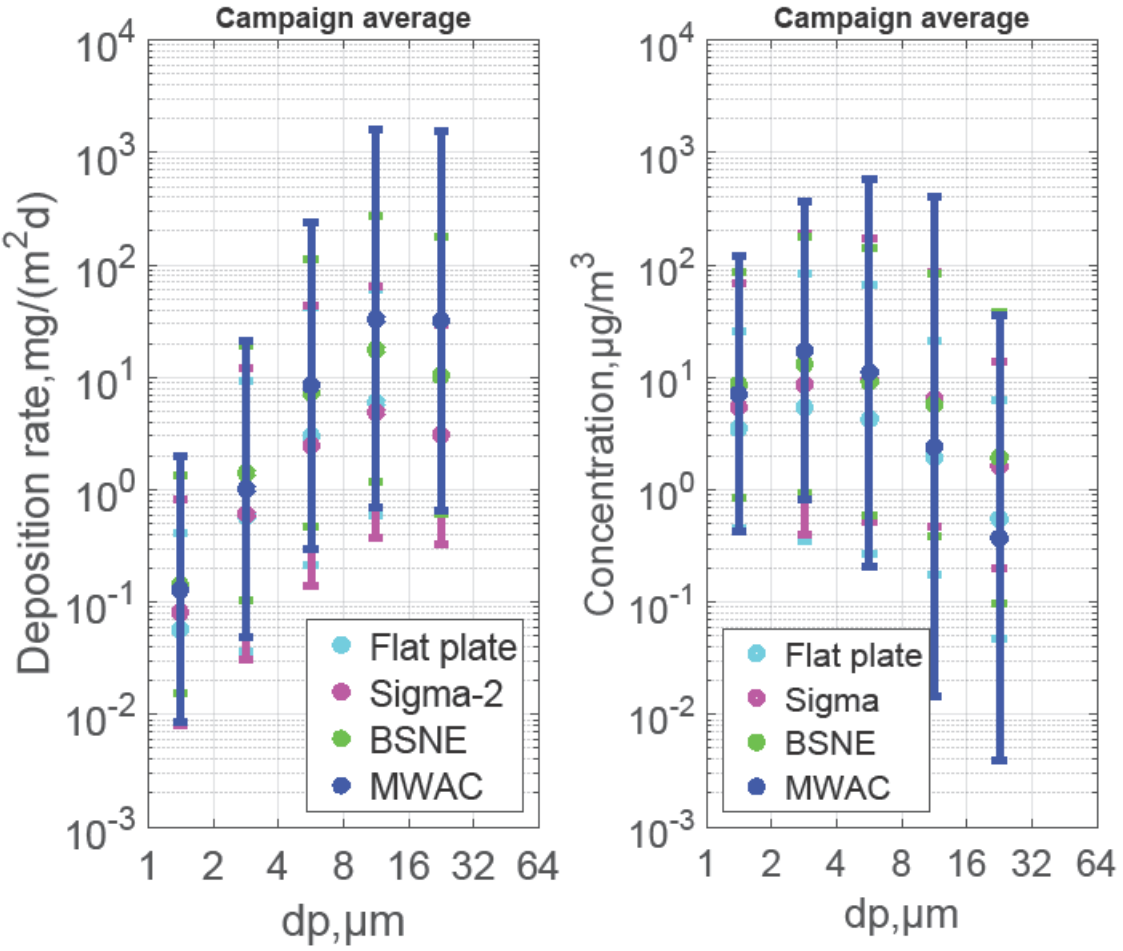

Figure 33: Size-resolved deposition rate and mass concentration measured by different samplers (campaign data). Different deposition velocity models are used for concentration calculation (Flat plate: Piskunov; BSNE: Piskunov; MWAC: combination of Piskunov- and impaction curve). The bars show the central 95% confidence interval of the daily variation.

9.1.4.2 Size-resolved comparison with active samplers

The calculated number concentrations in the size interval between 1–10 µm are compared with the concentrations measured using the OPC. Similarly, the mass concentration size distributions above the PM_{10} size range are validated using the FWI measurements.

Figure 34 shows a comparison of number concentration size distributions calculated from deposition rate measurements of the Flat plate, Sigma-2, BSNE and MWAC samplers with the number size distributions measured by the OPC for different days. Overall, most of the times the number concentrations obtained from OPC measurements are slightly higher than the ones from the deposition rates for the size range 2-5 µm and for dust days, with the exception of the Sigma-2, when considering only Stokes' velocity. This reflects the tendency of a relative

underestimation of the concentrations by the passive techniques for high concentrations, which was already visible in the correlation analysis above. In general, Figure 34 shows that the deviation of calculated values from OPC measured values is significant.

In this context, Figure 34 shows also the low influence of the two techniques used for u_* estimation. While the number concentrations derived using the friction velocity estimated from Wood (1981) formulation are slightly higher and therefore in better agreement with the OPC data, the difference appears to be negligible in general, probably owing to the relatively low wind speeds in this study. For the sake of completeness, the same comparison for the other samplers is shown in Figure 35, Figure 36, Figure 37 and Figure 38.

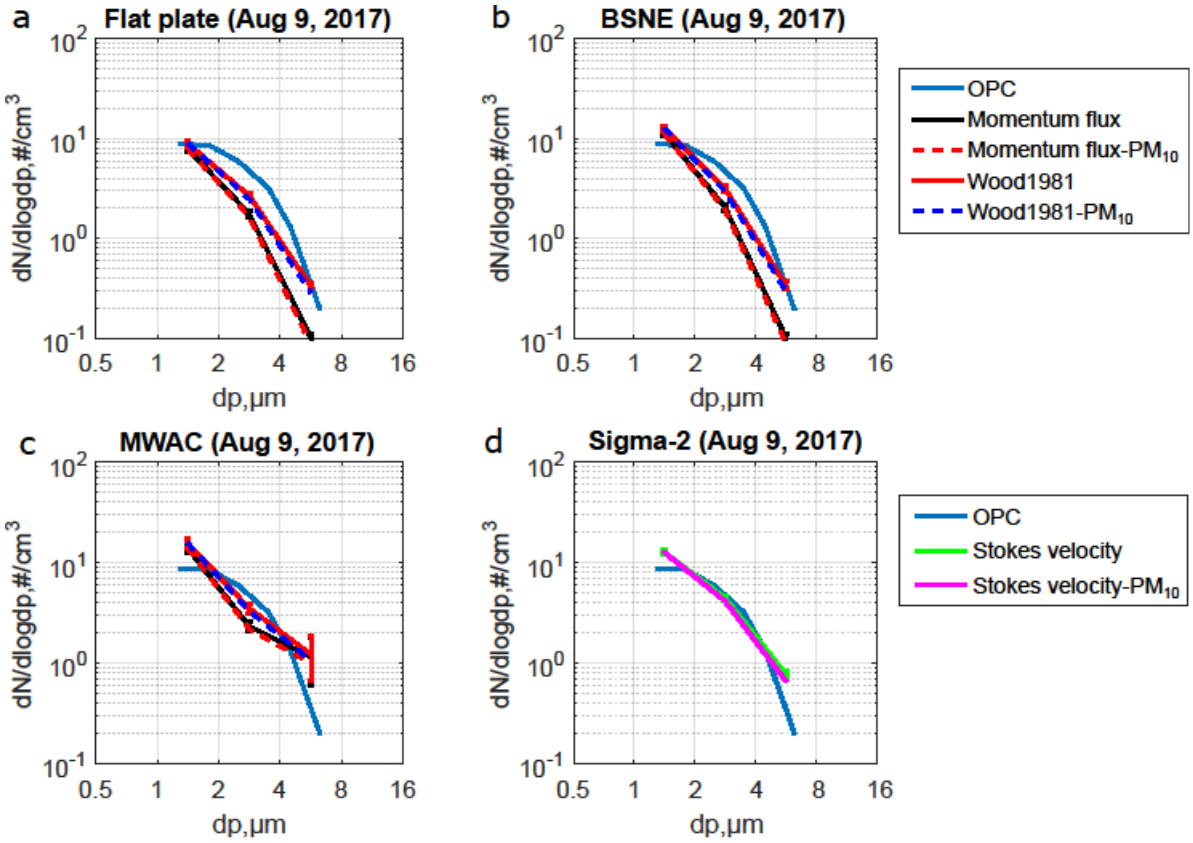

Figure 34: Comparison of the number concentrations calculated from the deposition measurements with the number concentrations measured by the OPC. Number size distributions are obtained by converting the SEM number deposition rates to number concentrations using the different deposition velocity models (Table 1), in analogy to the mass size distributions. The blue curve shows the concentration measurements by the OPC. For the concentrations obtained from the number deposition rates, two different approaches for the friction velocity are shown. The black curve shows the concentration curve calculated using the momentum flux approach without PM_{10} inlet correction (i.e. the atmospheric concentration). The red curve shows the concentration curve calculated using the Wood approach without PM_{10} correction. The dotted blue curve shows the concentration curve calculated using the Wood approach with PM_{10} inlet correction (simulating the concentration

the OPC would supposedly measure). The dotted red curve shows the concentration curve calculated using the Momentum flux approach with PM_{10} inlet correction. In case of the Sigma-2, the green curve shows the concentrations calculated using the Stokes velocity and the magenta curve the ones using Stokes velocity with the PM_{10} inlet correction. The bars show the central 95% confidence interval of the daily variation. (a): Flat plate; (b): BSNE; (c): MWAC; (d): Sigma-2. The average wind speed on Aug 9, 2017 was 3.0 m/s. Note that panel (d) refers to the second legend.

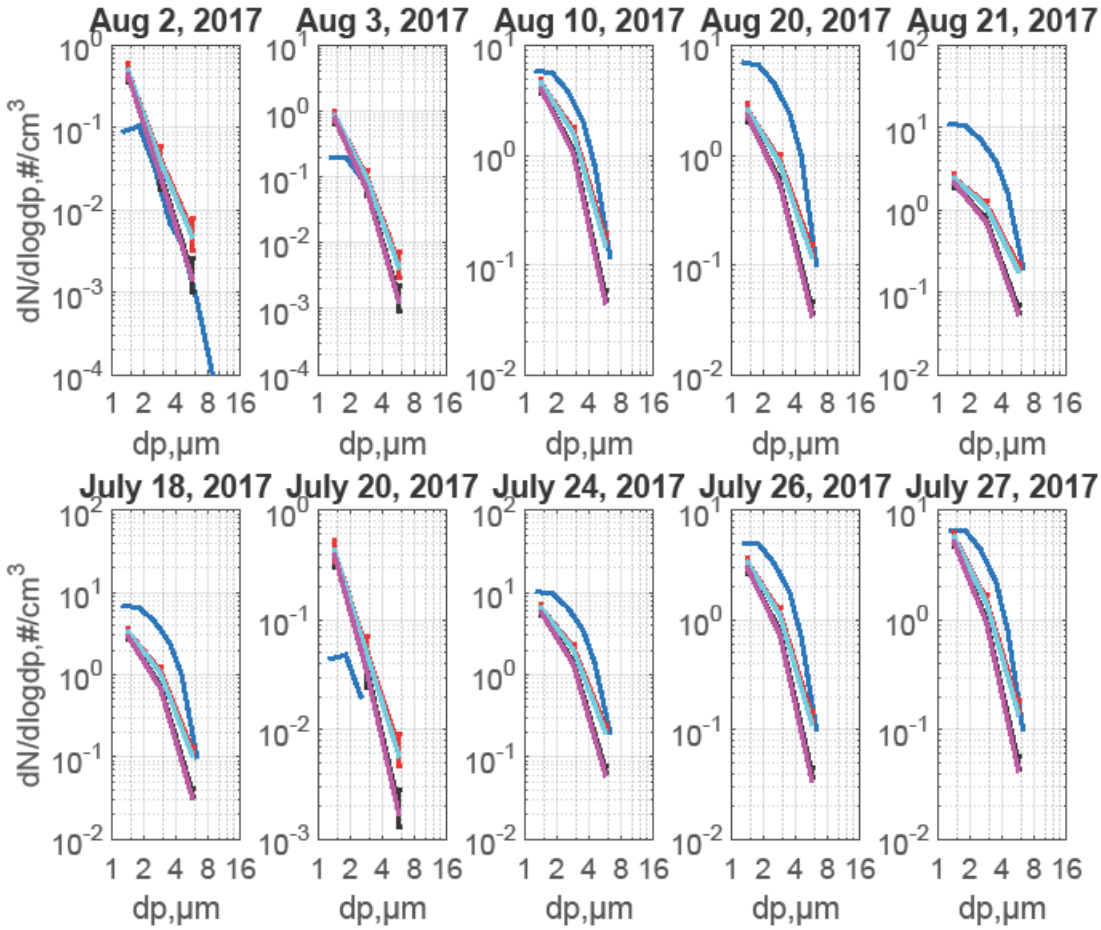

Figure 35: Comparing number concentration calculated from deposition measurement (Flat plate sampler) (Red: Wood 1981; Black: Momentum flux; Cyan: Wood 1981-PM_{10} inlet and Magenta: Momentum flux-PM_{10} inlet) with number concentration by OPC measurement (Blue). The bars show the central 95% confidence interval of the daily variation.

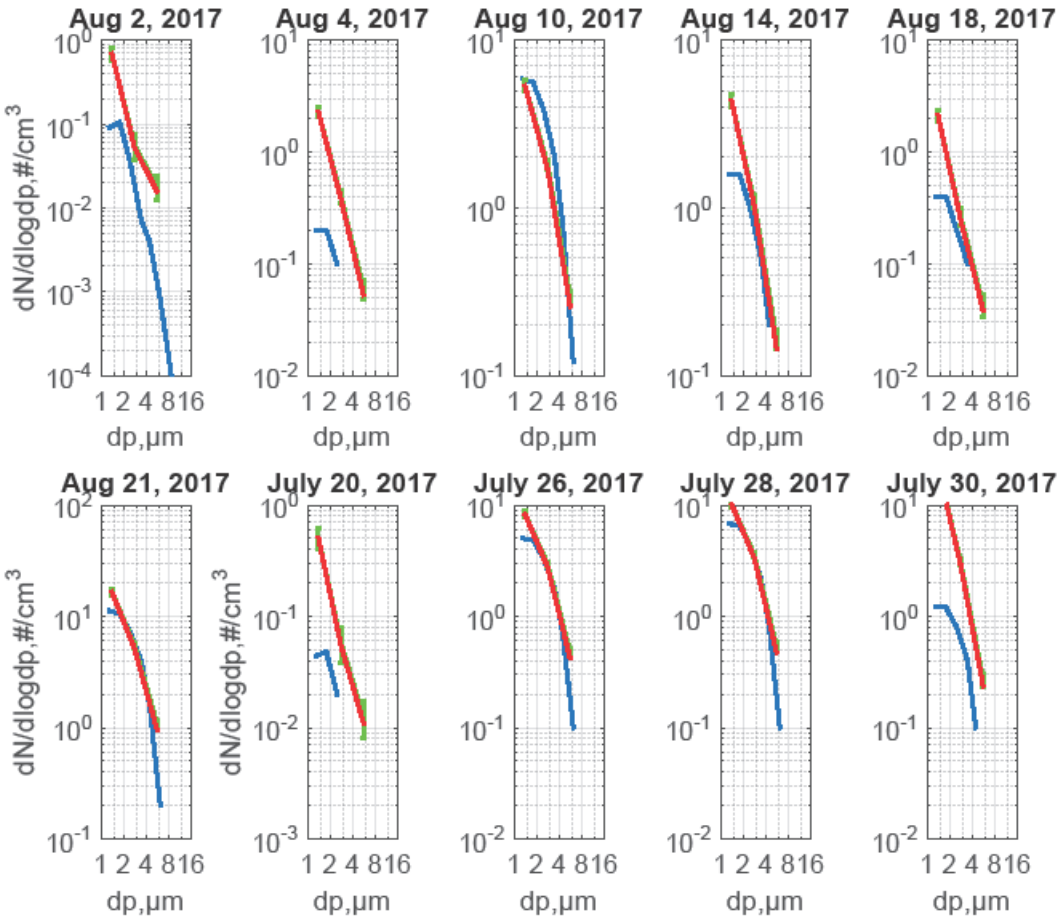

Figure 36: Comparing number concentration calculated from deposition measurement (Sigma-2 sampler) (Green: Stokes' velocity; Red: Stokes' velocity-PM_{10} inlet using Stokes velocity. with number concentration by OPC measurement (Blue). Concentration calculation from Sigma-2 sampler considers only Stokes's velocity (without considering friction velocity). The bars show the central 95% confidence interval of the daily variation.

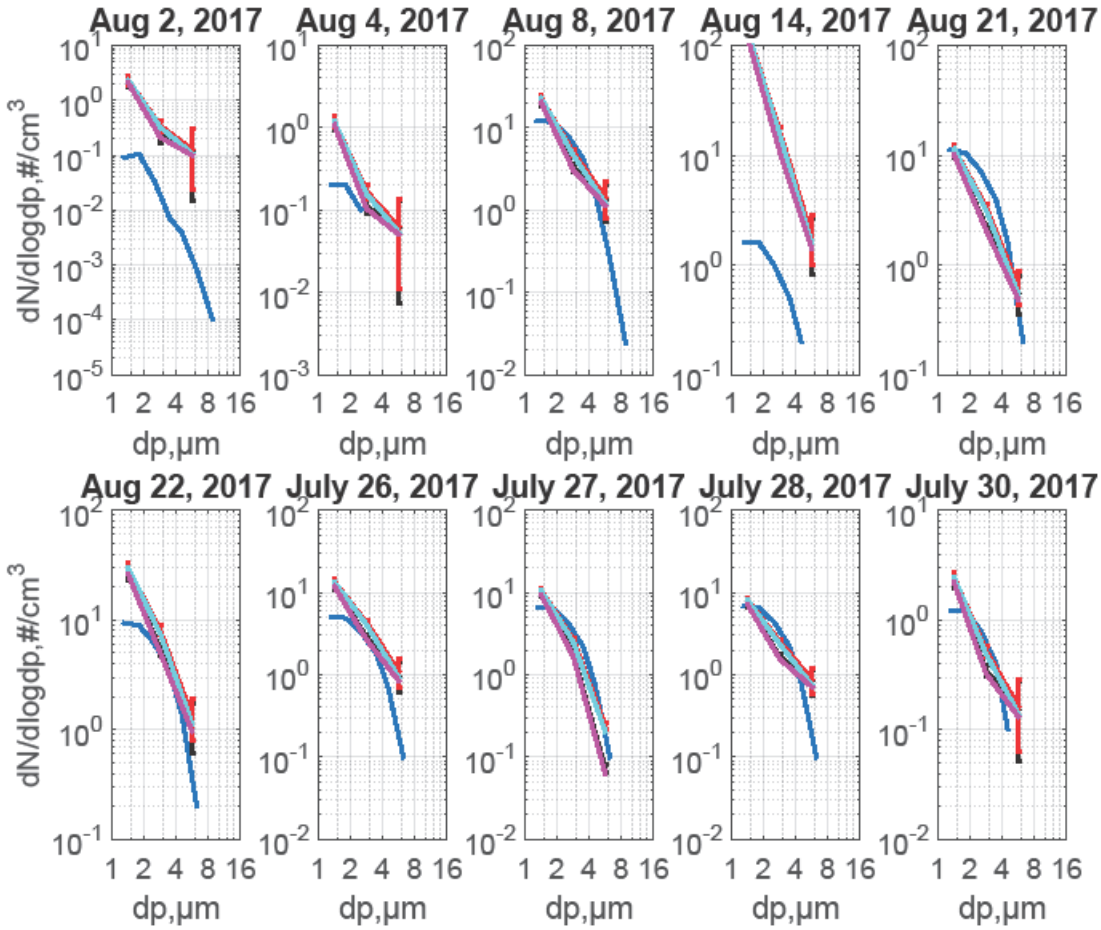

Figure 37: Comparing number concentration calculated from deposition measurement (MWAC sampler) (Red: Wood 1981; Black: Momentum flux; Cyan: Wood 1981-PM_{10} inlet and Magenta: Momentum flux-PM_{10} inlet) with number concentration by OPC measurement (Blue). The bars show the central 95% confidence interval of the daily variation.

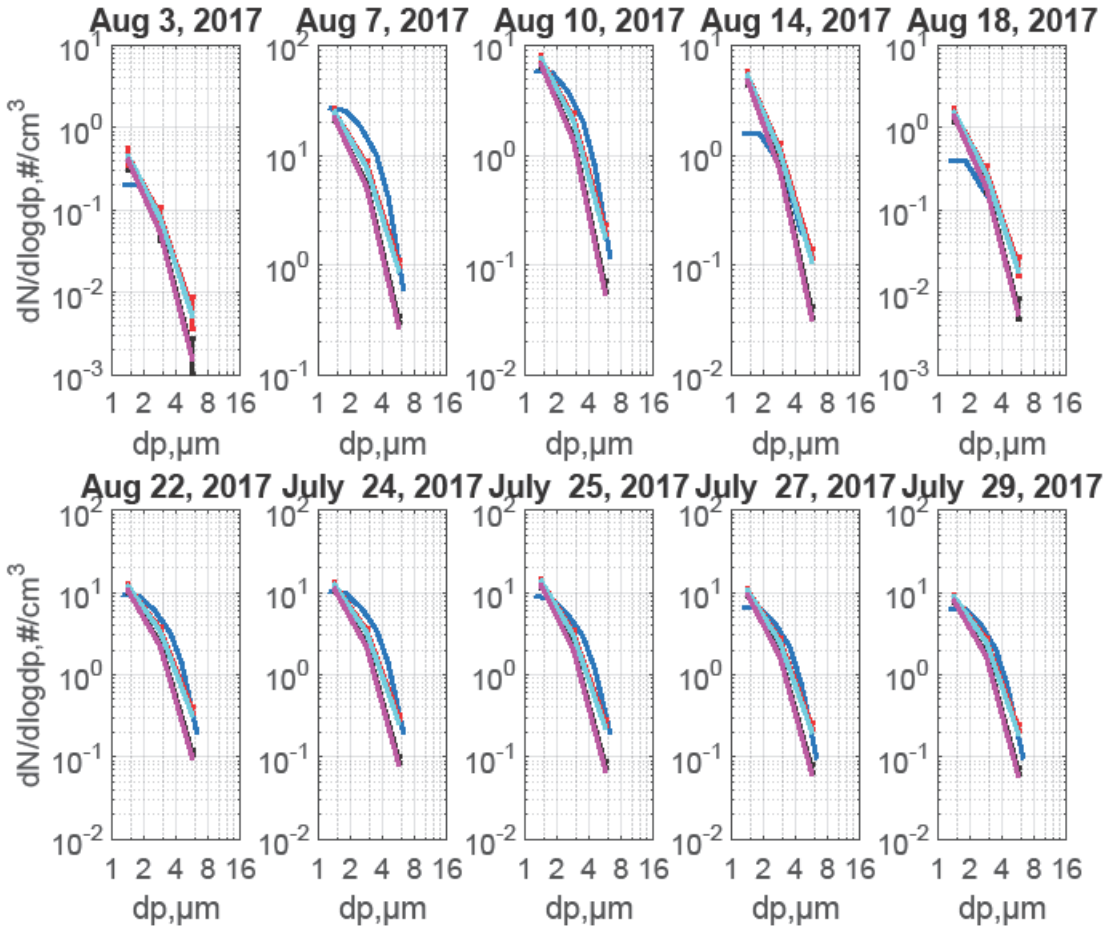

Figure 38: Comparing number concentration calculated from deposition measurement (BSNE sampler) (Red: Wood 1981; Black: Momentum flux; Cyan: Wood 1981-PM_{10} inlet and Magenta: Momentum flux-PM_{10} inlet) with number concentration by OPC measurement (Blue). The bars show the central 95% confidence interval of the daily variation.

Figure 39 and Figure 40 show the comparisons for the larger particles between the deposition-derived number concentrations and the ones from the FWI. Here, a significant inconsistency occurs between the mass size distributions from passive samplers and the ones from FWI. In particular, the size range larger than 10 µm seems to be generally underestimated by the passive samplers. While for particles around 10 µm, this could be partly to a badly-defined collection efficiency curve of the FWI ((Kandler et al., 2018); 50 % cut-off at 11 µm) and the according correction, this can't be the reason for the particles larger than 16 µm, where this efficiency approaches unity. Here, the deposition velocity for the samplers is apparently overestimated. A possible explanation would be inlet losses of the passive sampler, but this needs to be subject of further research. An overview of the OPC measurements comparing the size distributions between the long-term (deposition) and short-term (FWI) sampling is shown in Figure 41.

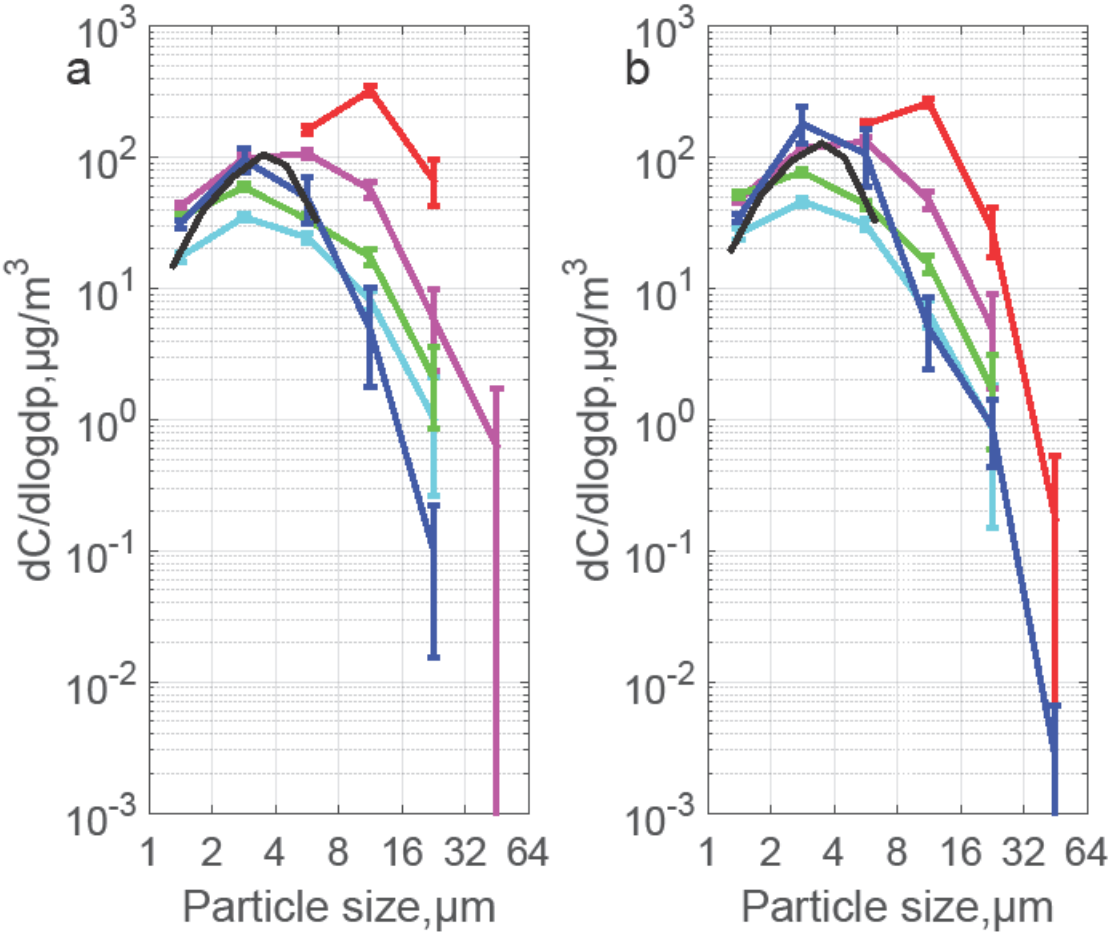

Figure 39: Daily average mass size distributions obtained from the passive sampler techniques in comparison to an active sampler (FWI). Mass concentration size distributions were calculated from the SEM mass flux measurements using the corresponding deposition velocity models. Samples were collected on 26th of July (a) and 27th of July (b). The mass concentration measurements shown by the FWI are daily averages (3 samples per day). The bars show the central 95% confidence interval of the daily variation.

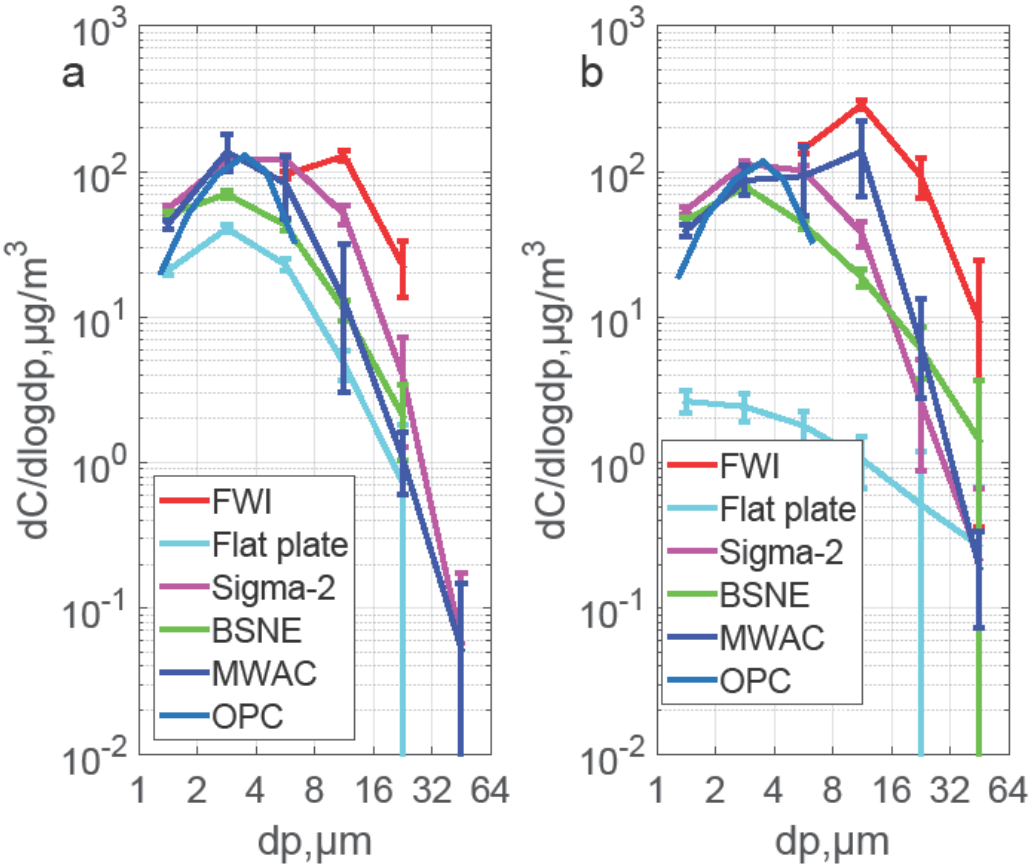

Figure 40: Daily average mass size distributions obtained from the passive sampler techniques in comparison to an active sampler (FWI). Mass concentration size distributions were calculated from the SEM mass flux measurements using the corresponding deposition velocity models. Samples were collected on 28th of July (a) and 29th of July (b). The mass concentration measurements shown by the FWI are daily averages (3 samples per day). The bars show the central 95% confidence interval of the daily variation.

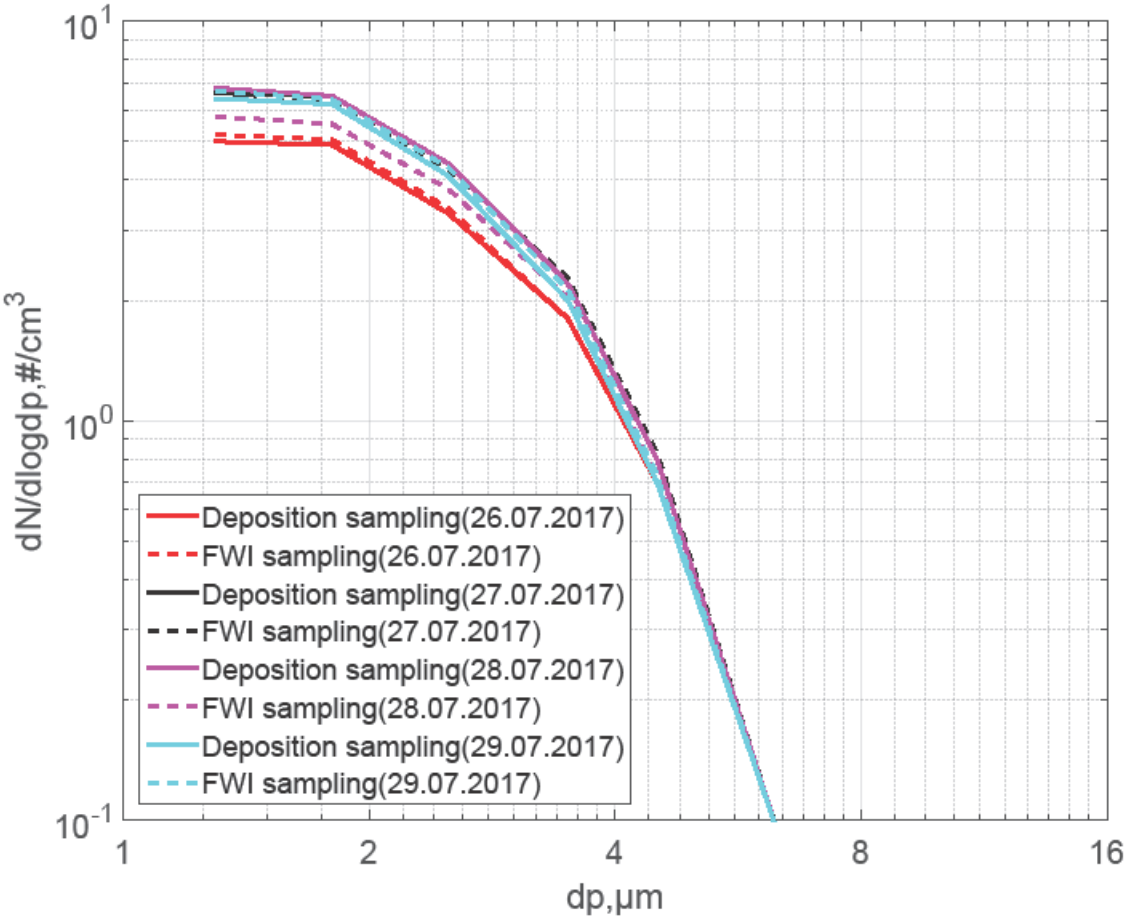

Figure 41: An overview of the OPC measurements comparing the size distributions between the long-term (deposition) and short-term (FWI) sampling.

In a last step, the deposition-derived concentrations are compared to those determined from the iso-axial filter sampler. Figure 42 shows that, while the calculated size distributions are in good agreement with the OPC ones, the filter-derived seem to relatively underestimate the concentrations. A correlation analysis (r^2: 0.681, p-value = 0.0854 and slope = 2.0394) suggests, that there is a weak positive correlation between calculated number concentration from filter samples and the OPC measured concentration. BSNE has been chosen here for comparison, as its agreement with the OPC measurements is generally the closest. The reasons for this weak correlation between the filter sampler and the OPC measurements – in particular compared to the stronger correlation between Sigma-2 and BSNE with the OPC – are not clear. For the sake of completeness, the same comparison for the other samplers is shown in Figure 43, Figure 44 and Figure 45.

While in general here, the disagreement between the Filter sampler and the MWAC and Sigma-2 samplers is significant, for the Flat plate sampler less disagreement occurs. In addition, an overview of the OPC measurements comparing the size distributions between the long-term (deposition) and short-term (filter) sampling is shown in Figure 46.

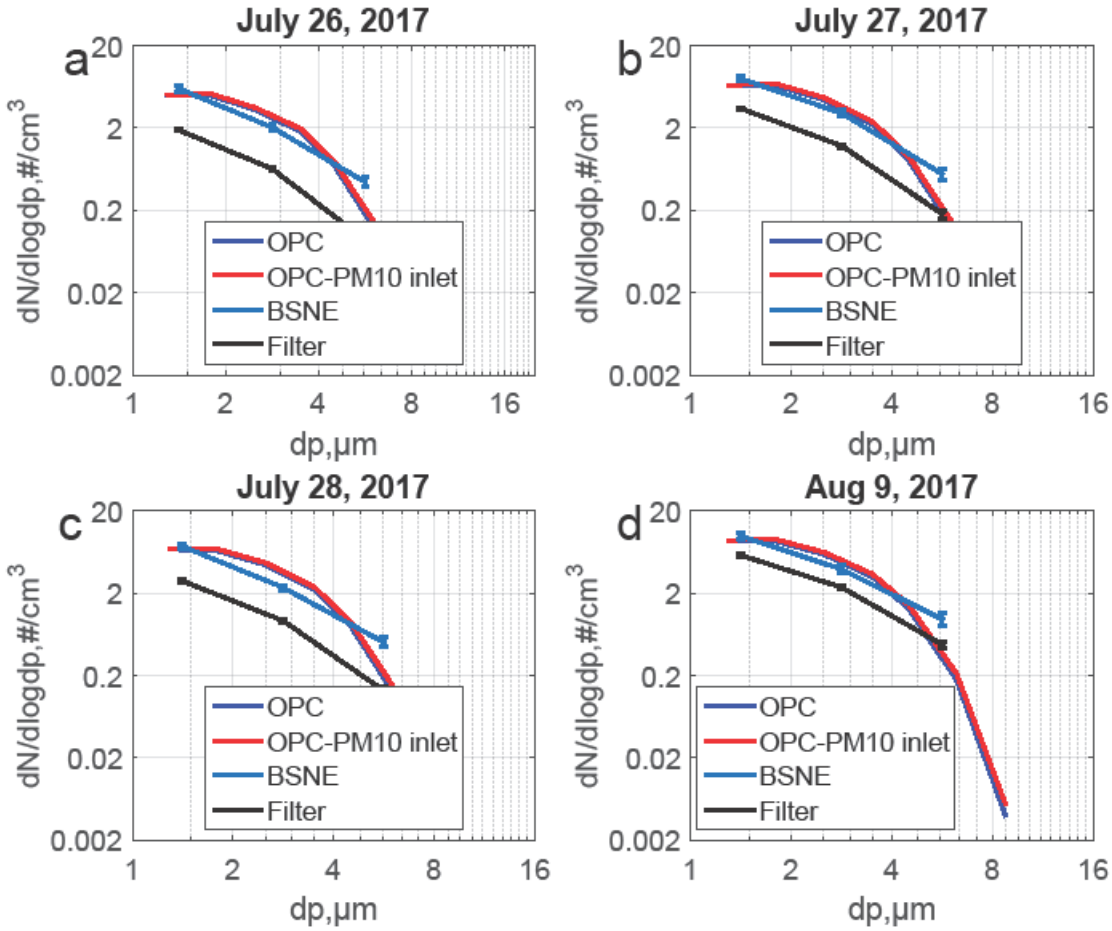

Figure 42: Number concentration size distributions obtained from the SEM analysis of the filter sampler, in comparison to BSNE sampler and OPC for different measurement days (a: July 26, 2017; b: July 27, 2017; c: July 28, 2017; d: August 9, 2017). Number concentration size distributions from deposition are obtained by converting the SEM obtained number deposition rates to number concentration using different deposition velocity models. The red curve shows the OPC with PM_{10} inlet efficiency correction (representing the atmospheric concentration). The number concentration measurements shown for the filter sampler are daily averages. The bars show the central 95% confidence interval of the daily variation.

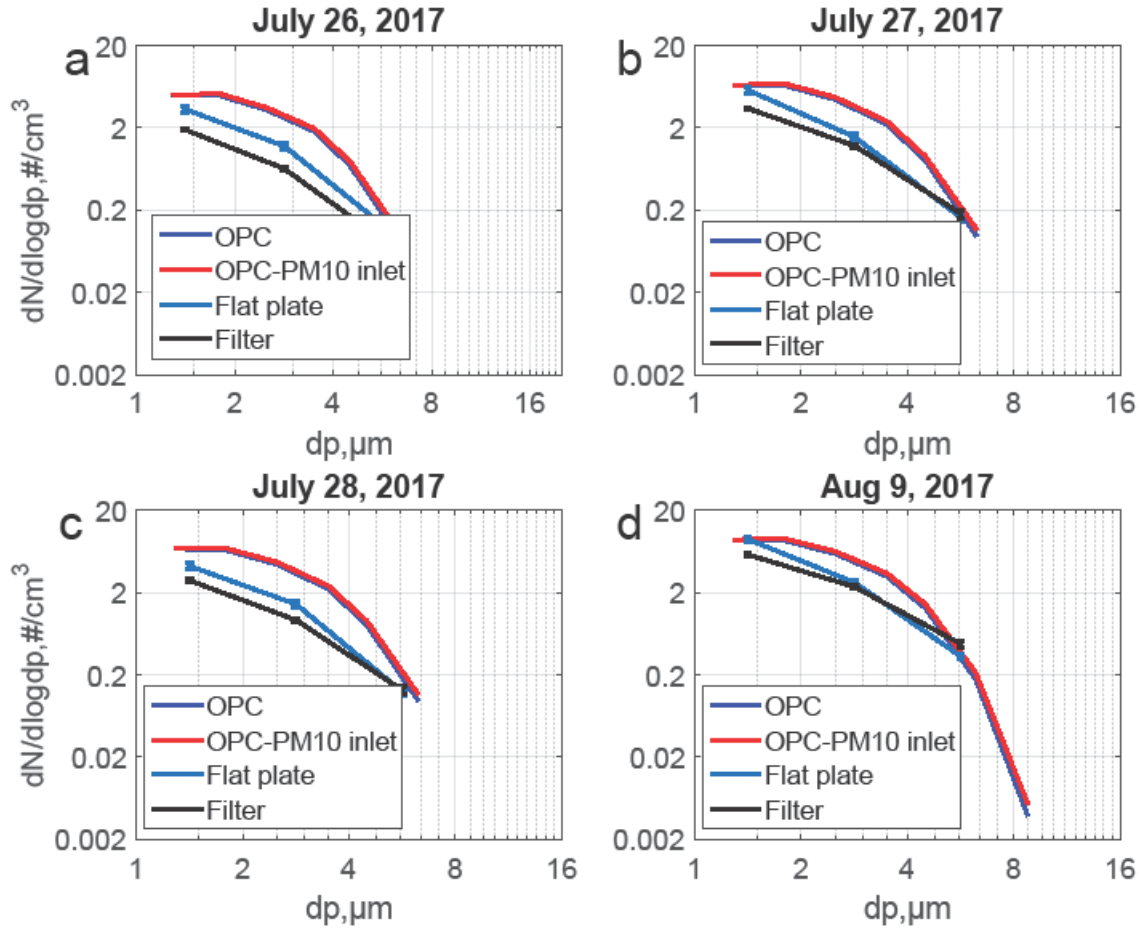

Figure 43: Number concentration measured with Filter-sampler method, in comparison to Flat plate sampler and OPC over different measurement days (a: July 26, 2017; b: July 27, 2017; c: July 28, 2017; d: August 9, 2017). Number concentration size distributions is obtained by converting the SEM obtained number deposition rate ((#/ (m^2day)) to number concentration using different deposition velocity models. The red curve shows OPC with PM_{10} inlet efficiency correction. The number concentration measurement shown by filter sampler is a daily average basis. The bars show the central 95% confidence interval of the daily variation.

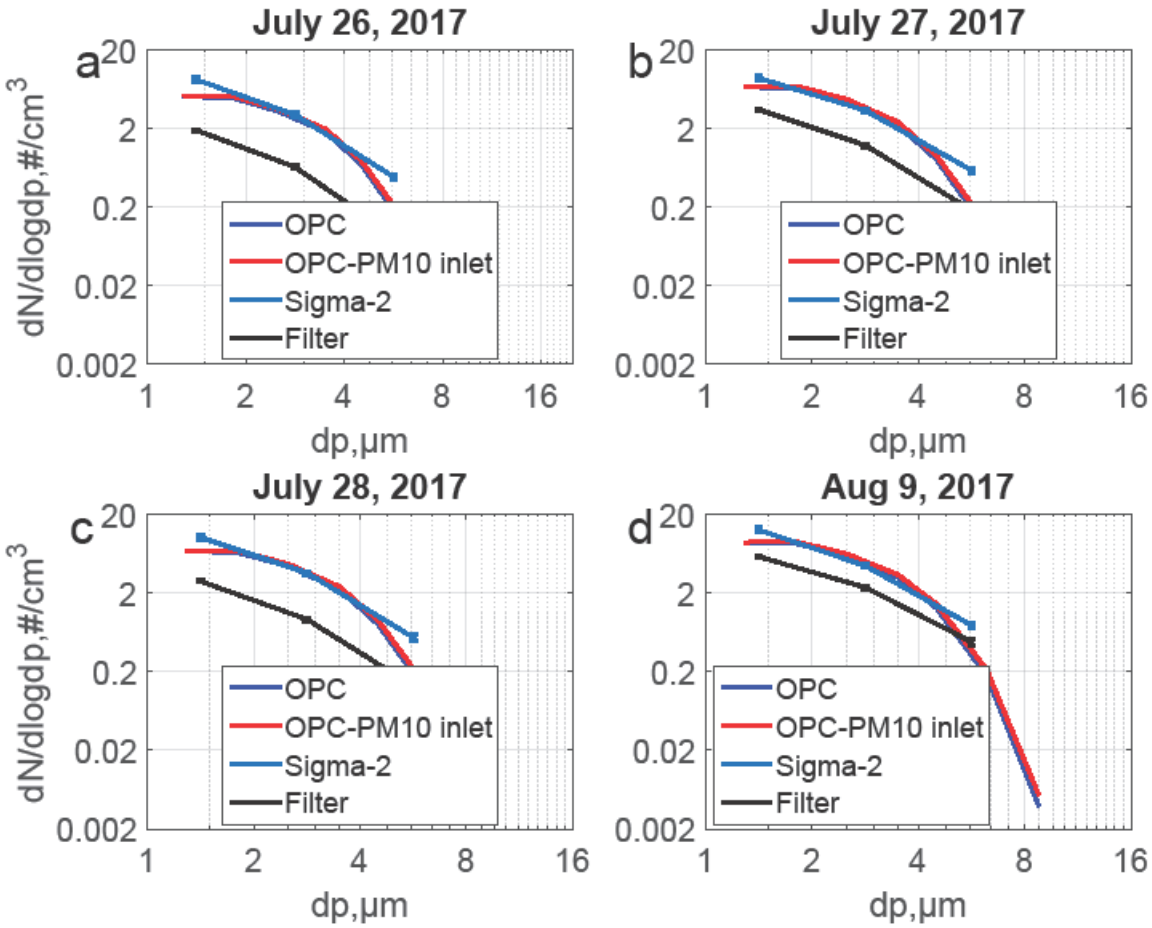

Figure 44: Number concentration measured with Filter-sampler method, in comparison to Sigma-2 sampler and OPC over different measurement days (a: July 26, 2017; b: July 27, 2017; c: July 28, 2017; d: August 9, 2017). Number concentration size distributions is obtained by converting the SEM obtained number deposition rate ((#/ (m^2day)) to number concentration using different deposition velocity models. The red curve shows OPC with PM_{10} inlet efficiency correction. The number concentration measurement shown by filter sampler is a daily average basis. The bars show the central 95% confidence interval of the daily variation.

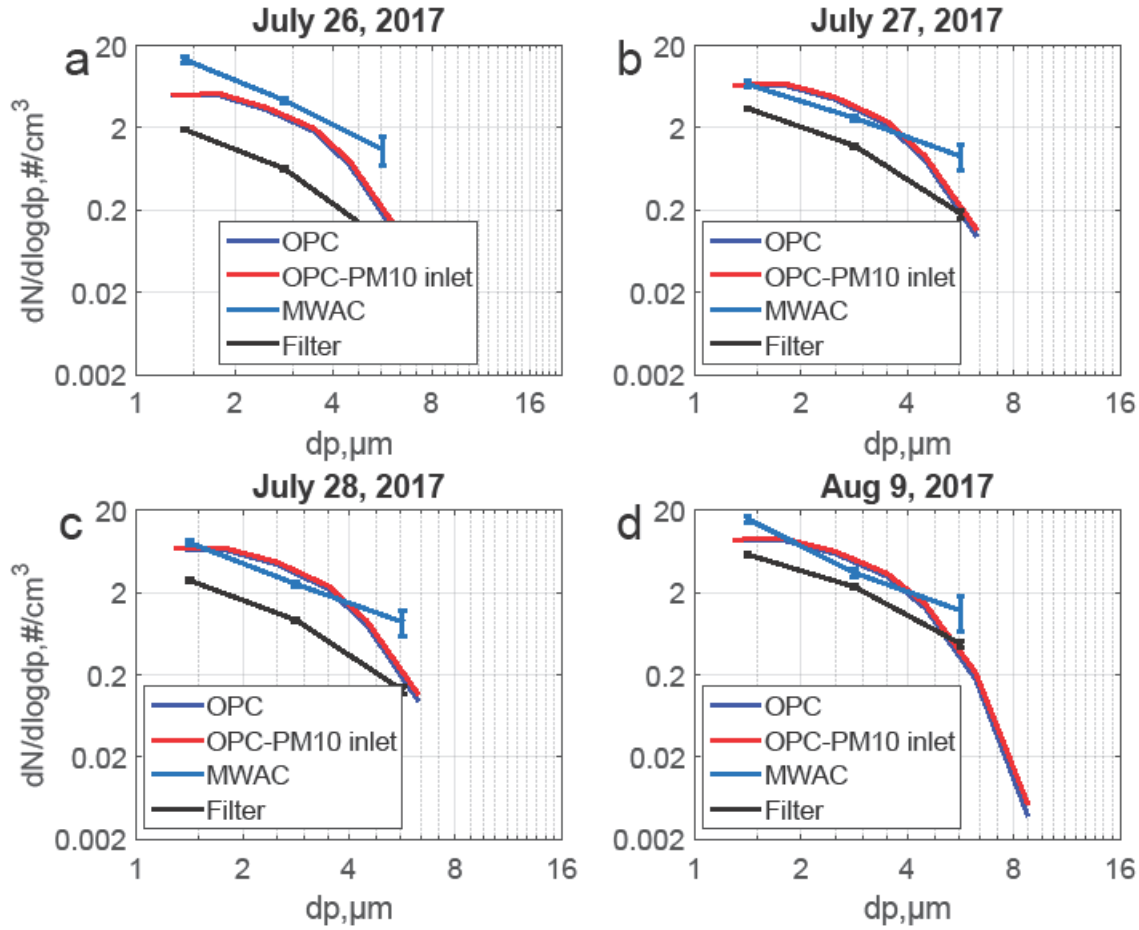

Figure 45: Number concentration measured with Filter-sampler method, in comparison to MWAC sampler and OPC over different measurement days (a: July 26, 2017; b: July 27, 2017; c: July 28, 2017; d: August 9, 2017). Number concentration size distributions is obtained by converting the SEM obtained number deposition rate ((#/ (m^2day)) to number concentration using different deposition velocity models. The red curve shows OPC with PM_{10} inlet efficiency correction. The number concentration measurement shown by filter sampler is a daily average basis. The bars show the central 95% confidence interval of the daily variation.

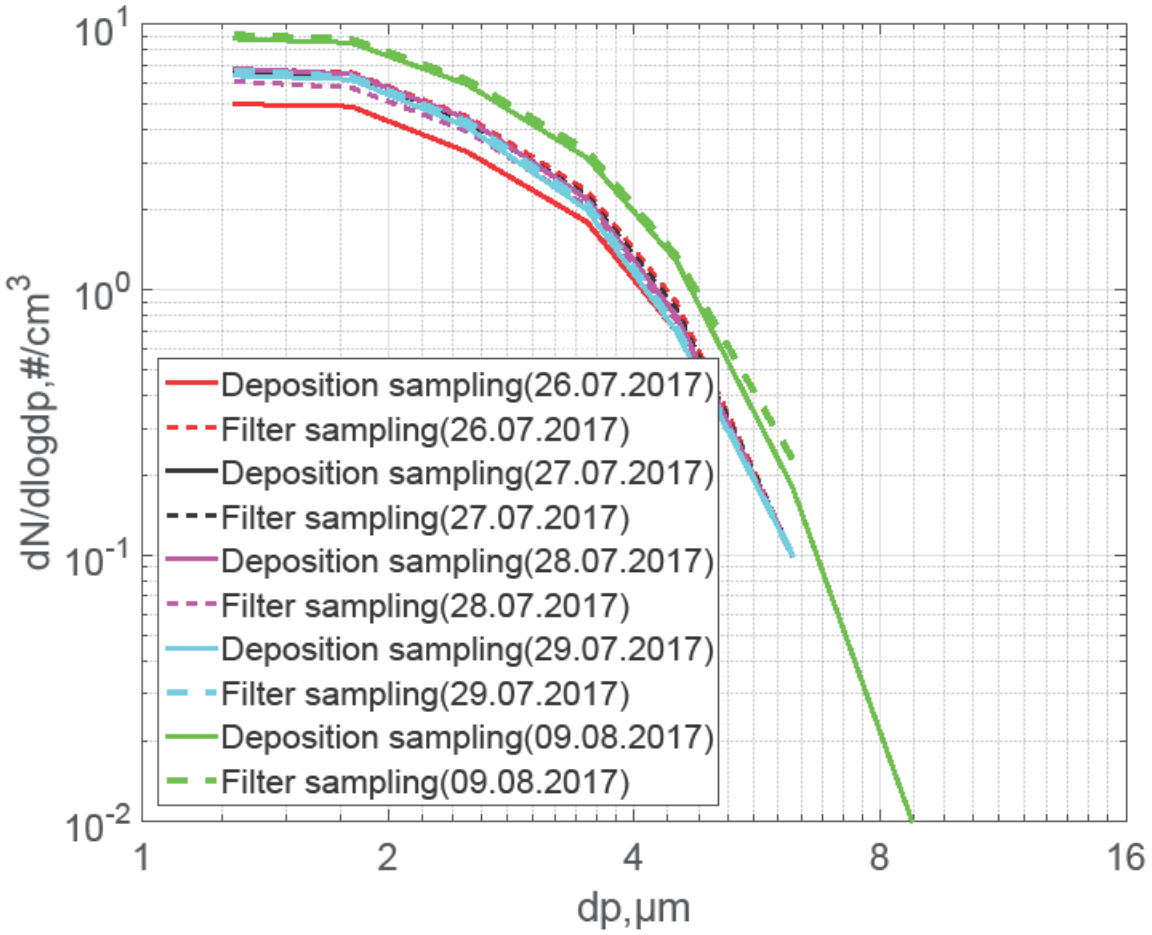

Figure 46: An overview of the OPC measurements comparing the size distributions between the long-term (deposition) and short-term (Filter) sampling.

9.1.5 Estimating the turbulent versus gravitational transport fraction

The size-resolved upward and downward deposition rates were derived from the upward-/downward facing deposition sampler by the same type of SEM analyses. Results of the size resolved-mass and number deposition rate measurements along with daily average temperatures and wind speeds are given Table A 5 and Table A 6 in the Appendix.

The upward deposition rate is always less than the downward deposition rate. This is expected because the upward facing substrate (i.e. measuring the downward-directed deposition rate) collects particles deposited by gravitational settling and turbulent inertial impaction, while the downward facing substrate (for the upward-directed deposition rate) collects particles only by means of turbulent impaction. Figure 47 shows the ratio of upward to downward mass deposition rate as a function of particle size. The deviation is greatest for the particle size range around 8 µm, which is strongly affected by turbulence (Noll and Fang, 1989). However, nearly

no trend of increasing ratio with increasing wind speed can be found here (see Figure 48). Besides the wind speed magnitude, different properties were calculated from the sonic wind data (e.g., turbulent intensity, Monin-Obukhov length, relative standard deviation of wind speed, average vertical component), but none of them was able to explain the observed variations in the deposition rate ratio.

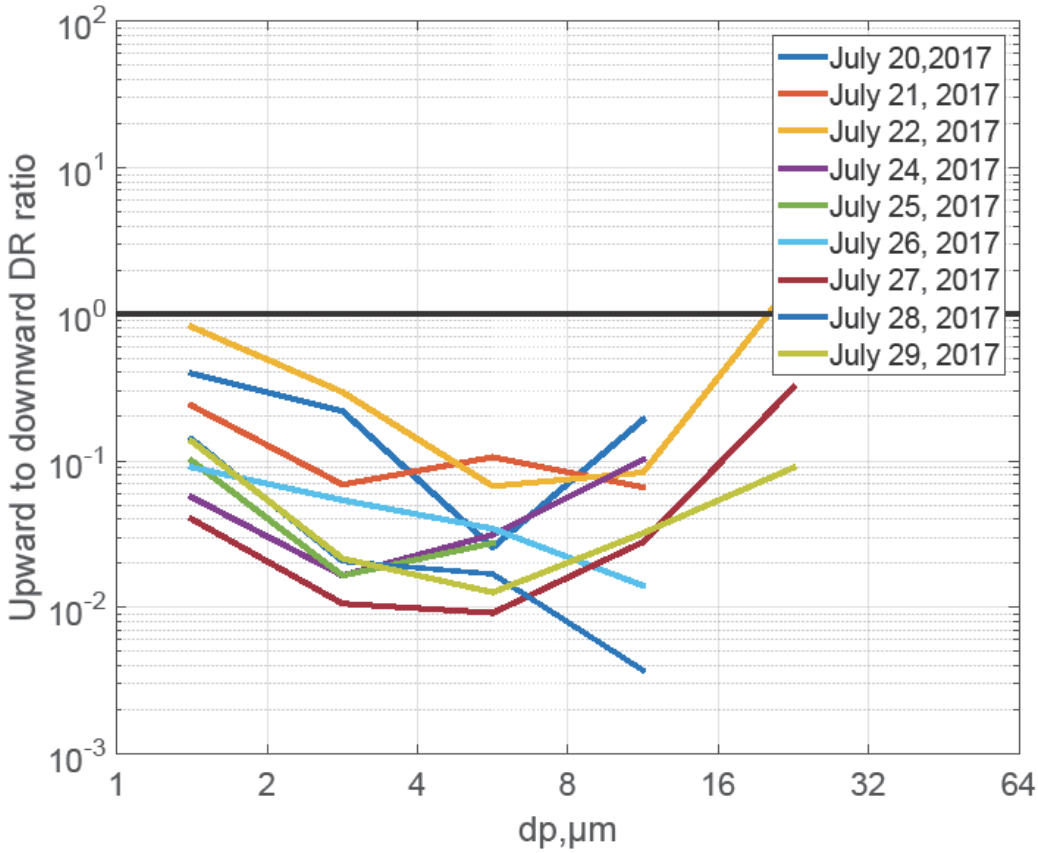

Figure 47: Ratio of upward- to downward-directed mass deposition rate as a function of particle size. The deposition rate is measured using the upward-downward-Flat plate sampler (with 25 mm stub).

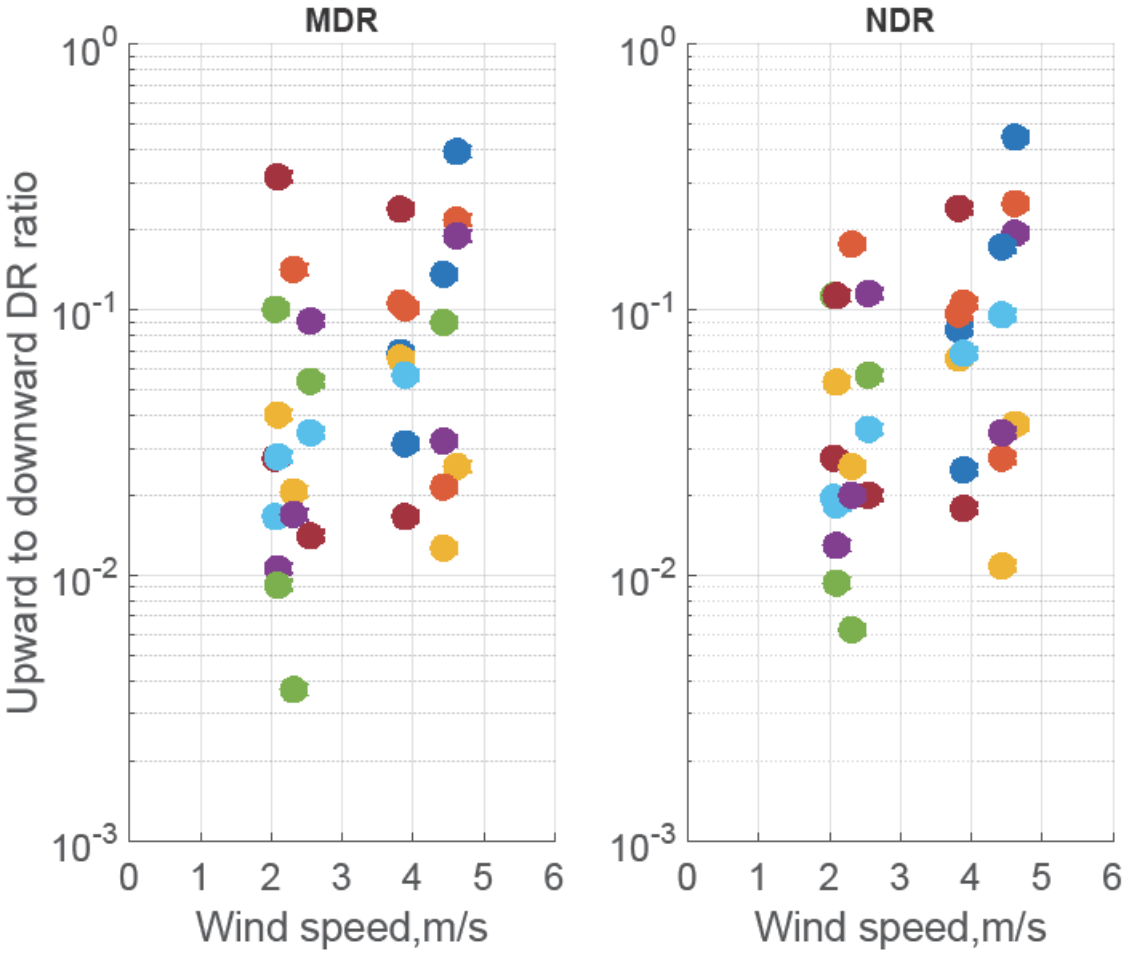

Figure 48: Upward to downward deposition rate ratio vs wind speed. The deposition rates are measured using Flat plate sampler (with 25 mm stub). Different colors represent different size intervals (blue: 1-2 µm; orange: 2-4 µm; yellow: 4-8 µm; Violet: 8-16 µm; green: 16-32 µm; cyan: 32-64 µm).

9.2 Computational fluid dynamics (CFD) simulation)

Using computational fluid dynamics (CFD), deposition velocities of particles for different passive samplers were predicted and compared to the analytical deposition velocity models used for the different samplers (see Figure 49 and Figure 50). While for the Flat plate and MWAC sampler the curves agree qualitatively (i.e. showing deposition speeds higher than Stokes velocity at particles sizes 4-16 µm, which are supposedly strongest affected by turbulence), for the Sigma-2, they are largely contrary except for the lowest wind velocity. The latter might be owed to the fact that in a flow model, the non-omnidirectional construction of the Sigma-2 might lead to preferred airflows, which are not relevant in a more variable and

turbulent atmosphere. However, also for the former ones, the deposition velocity curves are quantitatively largely different. In this context, Figure 51 shows a comparison of the CFD-derived particle deposition velocities at different wind speed values for different samplers. For the Flat plate and the MWAC samplers, the deposition velocity increases with the wind speed, while for the Sigma-2 sampler, such a relation is not observed. Moreover, it can be seen from the figure that in general for the Flat plate and the MWAC samplers, Stokes' velocity is considerably lower than the deposition velocities calculated at different wind speeds by the other models. Interestingly, however, this is not true in the case of Sigma-2 sampler. In general, for the effect of wind speed on the Sigma-2 sampler is not yet clear, why there is an effect for some sizes and for others not, so further modeling work is needed.

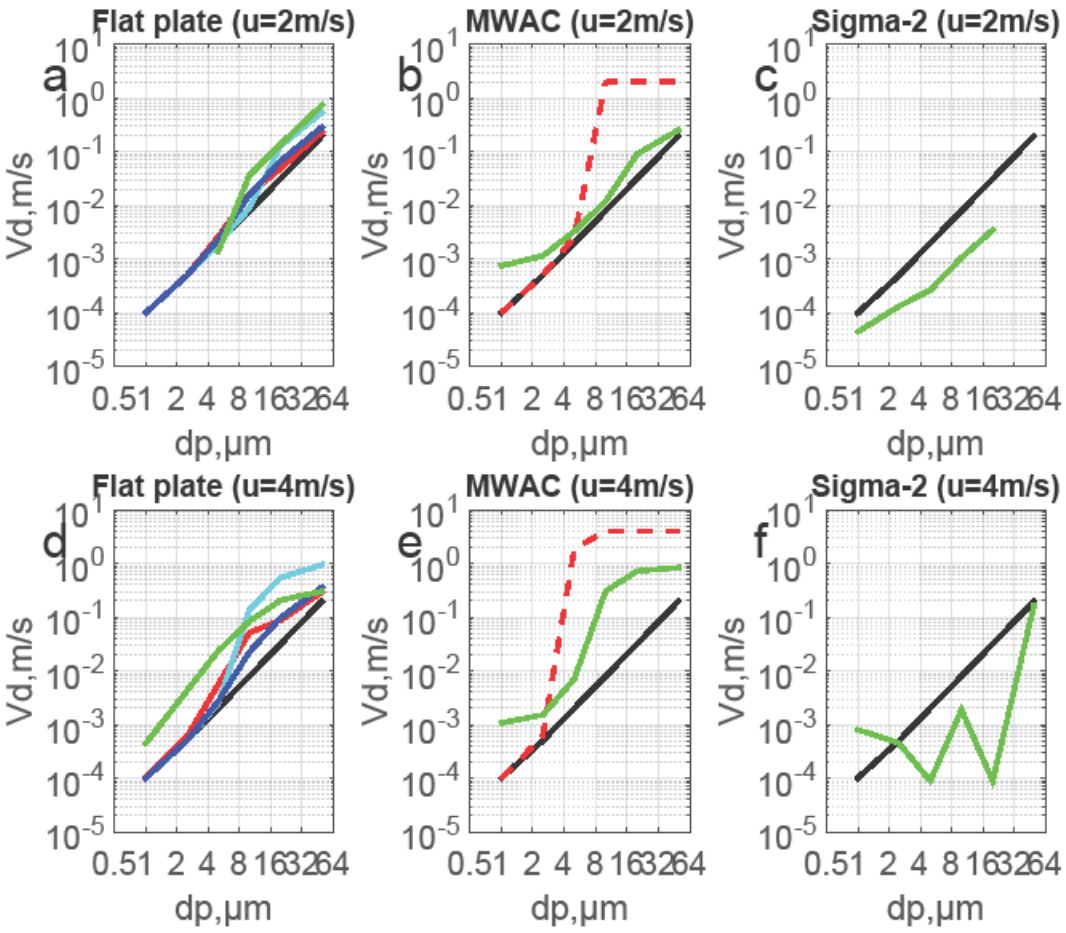

Figure 49: Deposition velocities calculated for different samplers by analytical and CFD approaches. The red curve shows the deposition velocity calculated using the Piskunov model, the dotted red curve shows the combination of the Piskunov and the impaction curve model, the black curve shows the Stokes deposition velocity, the blue curve the Noll and Fang model, the cyan the Zhang model, and the green curve finally the deposition velocity from CFD. Panels **a-c** are calculated for 2 m/s wind speed, **d-f** for 4 m/s.

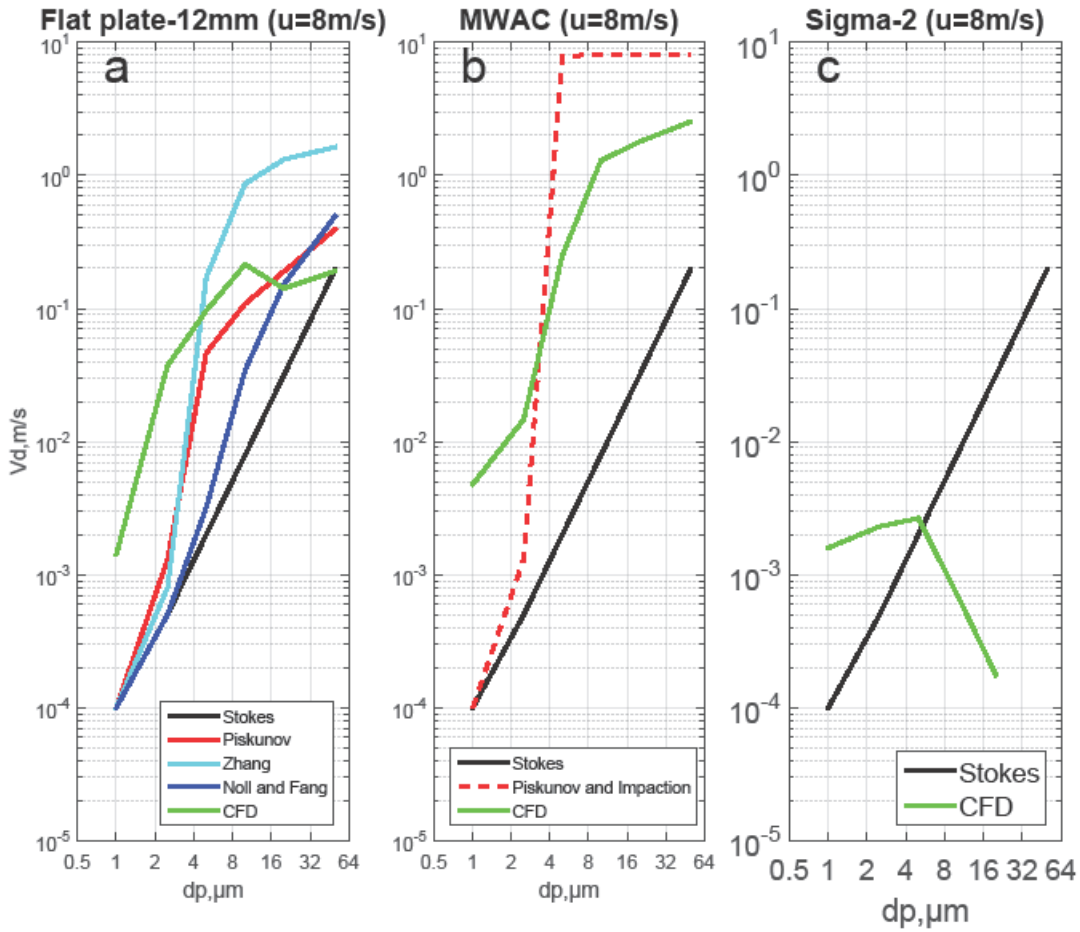

Figure 50: Deposition velocities calculated for different samplers by analytical and CFD approaches. The red curve shows the deposition velocity calculated using the Piskunov model, the dotted red curve shows the combination of the Piskunov and the impaction curve model, the black curve shows the Stokes deposition velocity, the blue curve the Noll and Fang model, the cyan the Zhang model, and the green curve finally the deposition velocity from CFD (at 8 m/s wind speed). (a): Flat plate; (b): MWAC; (c): Sigma-2

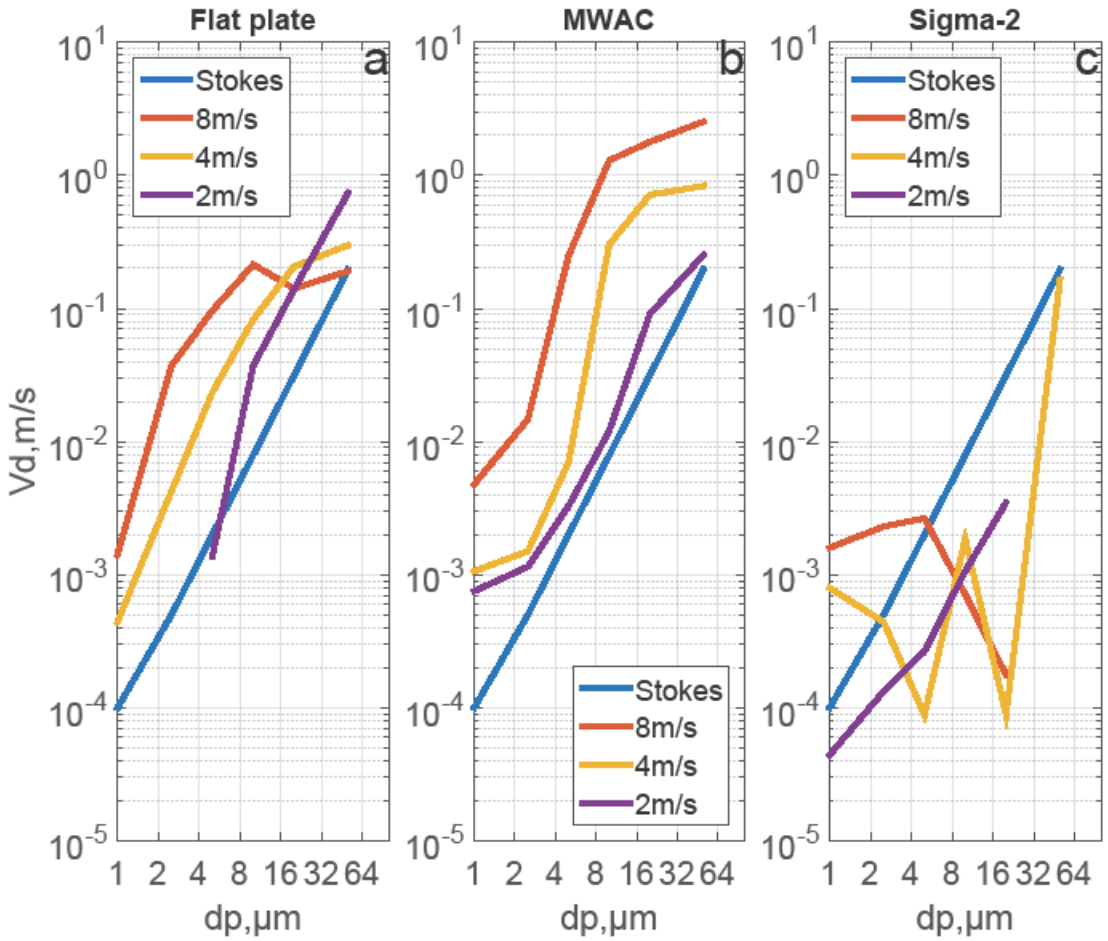

Figure 51: Comparing the CFD-derived particle deposition velocities at different wind speed values for different samplers. (a): Flat plate; (b): MWAC; (c): Sigma-2.

9.3 Comparison of measured deposition rate ratios to analytically and CFD modeled ones

As there is no reference instrument for dry deposition sampling, the separate approaches are compared in a relative way. Figure 52 **a-c** show comparisons of the deposition velocity ratios derived from the analytical models with the according measured deposition velocity ratios (equalling the according deposition rate ratios), **d-f** the respective correlation of the ratios derived from CFD modeling with the measurement. As the CFD models could only be calculated for a limited number of flow velocities, deposition velocity values were interpolated between the calculated cases. Generally, the agreement is very poor. Practically, no variation observed in the measurement data can be explained by model variation, independently of the

type of model. While this might be explained to a smaller extent by the propagating measurement uncertainties for the largest particles with low counting statistics, for the smaller ones this systematic deviation must have other reasons.

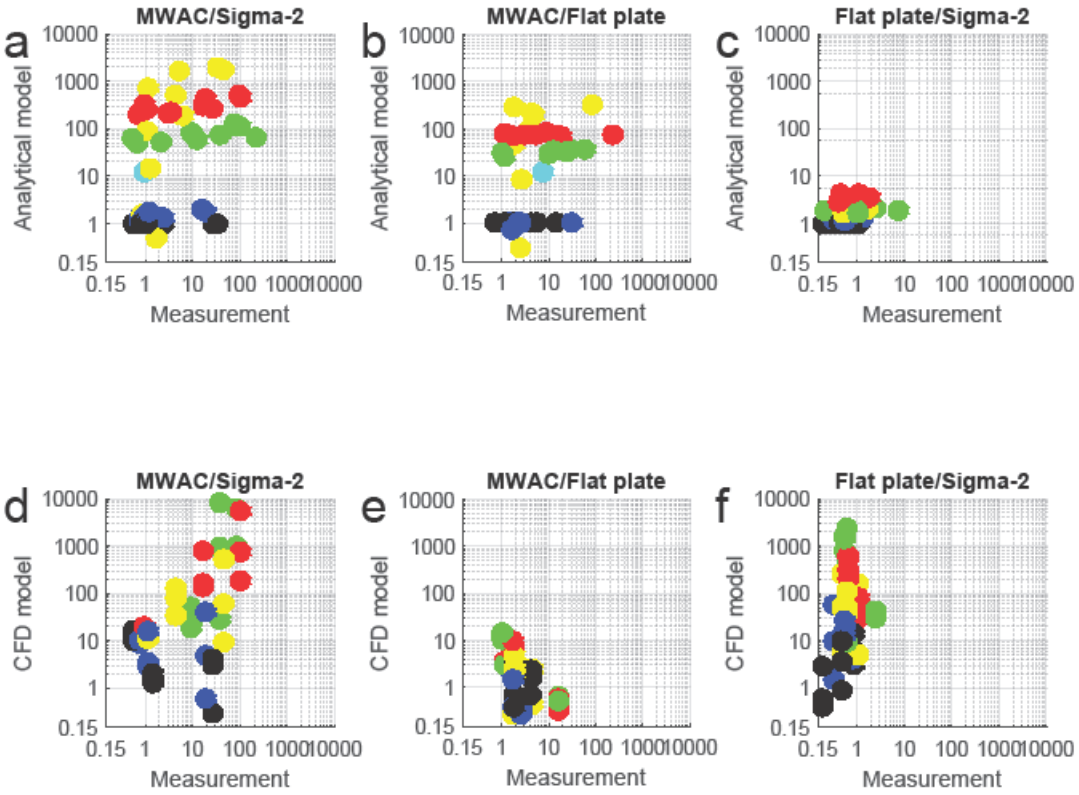

Figure 52: Comparison of the observed deposition velocity ratios with modeled ones by the analytical deposition models (upper row, a-c) and by the CFD models (lower row, d-f). (a, d) MWAC/Sigma-2; (b, e) MWAC/Flat plate; (c, f) Flat plate/Sigma-2. Multiple daily measurements are shown in each plot. Different colors represent different size intervals. 1-2 µm: Black, 2-4 µm: Blue, 4-8 µm: Yellow, 8-16 µm: Red, 16-32 µm: Green, 32-64 µm: Cyan.

10 Data analysis with respect to size distribution, chemical composition, and optical properties

10.1 Chemical composition and composition classification

As I collected a large number of particles, phase determination of individual particle was not possible therefore here analysis of only chemical information (disregarding the mineralogical phase) has been shown. According to the results from the SEM–EDX analysis, 19 elements for quantification (F, Na, Mg, Al, Si, P, S, Cl, K, Ca, Ti, V, Cr, Mn, Fe, Co, Ni and Cu) in the individual aerosol particles has been chosen. A value of M(X) was calculated for elements and combinations of elements (Kandler et al., 2007; Li et al., 2018) as follows:

$$M(X) = X/(F+Na+Mg+Al+Si+P+S+Cl+K+Ca+Ti+V+Cr+Mn+Fe+Co+Ni+Cu) \times 100.$$

According to M(X), the particles were classified into 31 different groups. Previously developed classification scheme was used (Kandler et al., 2007) (for details, see Table A 7 in the Appendix).

10.2 Comparison of mineral dust concentrations - Tenerife vs. Barbados

There are reports on long range transport of desert dust that PM_{10} doesn't change much between Tenerife and Barbados (Maring et al., 2003; Schütz, 1980), however, there is no such report on measurements for large particles. Therefore, in this work, comparison of mass concentration size distributions from FWI measurements is shown. To the best of our knowledge, this is the first study to show the mass concentration size distribution comparison of large particles in these two regions.

10.3 Calculation of the refractive index

Frequently, the complex refractive index is considered to be the most basic and an important indicator for describing the optical properties of aerosol particles in general (Zhang et al., 2015). In the present study, size resolved optical property main complex refractive index (Imaginary and Real parts) from our deposition measurement is demonstrated. While the real part express the extent of scattering by the particle, the imaginary part indicates an absorption loss when the

wave propagates via the particles (Skiles et al., 2017). The complex refractive index of dust aerosols, which is wavelength and size dependent, is characterized by their real and imaginary parts (Banks et al., 2018). It is described by using the following equation (Skiles et al., 2017):

$$m_\lambda = n_\lambda + ik_\lambda \quad \textbf{(16)}$$

Where $n_\lambda$is and $ik_\lambda$are real part, also known as the simple index of refraction and the imaginary the imaginary part respectively. The average complex refractive index $\bar{m}$ of the total aerosol is calculated by using the following equation (Ebert et al., 2002):

$$n = \frac{n_1 v_1 + \cdots + n_i v_i}{v_1 + \cdots + v_i} \quad \textbf{(17)}$$

$$\bar{m} = \frac{1}{V}\sum_{i=1}^{k}(m_i v_i) \quad \textbf{(18)}$$

Where n_i, and v_i refractive index of real parts, and the volume of particle group i, respectively.

10.3.1 Real part

The particle groups used in the calculation of imaginary part are: Silicates, quartz, Ca-rich particles (calcite), S-rich (sulfate), and Fe-rich particles (hematite). These group particles are selected for analysis because they are dominating particle type in dust aerosol. The refractive index values used for the different particle groups are given in Table 5.

Table 5: Refractive indices (real part) of the different particle group, taken from Kandler et al. (2009).

Particle group	**Wavelength**			
	350 nm	630 nm	870 nm	1640 nm
Silicates	1.60	1.56	1.54	1.54
Si-rich (Quartz)	1.57	1.55	1.53	1.53
Ca-rich (Calcite)	1.69	1.66	1.65	1.63
S-rich (Sulfate)	1.54	1.53	1.52	1.49
Fe-rich (Hematite)	2.30	2.8	2.6	2.4

It has to be noted that this volume mixture rule is a great simplification of the physical processes (Lindqvist et al., 2014; Nousiainen, 2009). However, the detailed information required for the in-depth modeling approaches is not available for large numbers of particles. Therefore, I use the volume mixing as a first order estimate, which is in general a fair approach in the range of the uncertainties (Ebert et al., 2002; Müller et al., 2009; Petzold et al., 2009).

10.3.2 Imaginary part

The imaginary part of complex refractive index (k) is calculated for iron oxide particles by using the following equation (Di Biagio et al., 2019):

$$k = aMC + b \quad \textbf{(19)}$$

Where MC is the mass concentration iron oxide, and a and b are the retrieved slope and retrieved intercept respectively.

It is possible that iron oxide can be present in more particle classes than only in iron-rich class particles. Therefore, then, the iron oxide volume content is derived from the total iron content of all particles in the mineral dust classes (Kandler et al., 2009).

To calculate the refractive index of the imaginary part, first the mass of iron particles from total dust particle containing considerable amounts of iron is inferred for each particle. The iron oxide content is calculated from mass of iron particles based on the formula suggested by Di Biagio et al. (2019). Because of its mineral features the largest absorption potential (Alfaro et al., 2004; Wagner et al., 2012), iron oxide (hematite) is selected for analysis of imaginary part of refractive index. Using the volume mixture rule, I calculate the average values for imaginary parts of the refractive index for iron oxide contents of dust aerosol particles at discrete wavelengths between 370 and 950 nm.

10.4 Role of iron (Fe) particles in ocean productivity and biogeochemical cycle

To investigate deposition of Fe particles to ocean surface, first, Fe-rich particles were identified using the M(X) rule and then size resolved deposition rates for these Fe-rich particles is calculated.

10.5 Aerosol potential buffering

To investigate the buffering potential of dust aerosol, first particles are classified into different groups using the M(X) rule. And then out of the group, the Ca-rich (the carbonate aerosol) and Fe-rich particles were selected for analysis of the buffering potential. Finally, the mixing state of the compounds is analyzed by classifying the particles into a matrix spanned by the Ca and Fe index.

10.6 Mixing of sulfate particle with dust

Identifying the state of mixing of aerosol particle is important because the mixing state can have an impact on radiative properties of aerosol particles (Bauer et al., 2007). It has been demonstrated by single particle analysis that mineral dust aerosol particles are frequently mixed with sulfate (Dall'Osto et al., 2010; Falkovich et al., 2001; Kandler et al., 2011).

Using the same approach mentioned previously, the sulfate (S-rich) particles were sorted out from the group. Then, the mixing state of dust particles with sulfate particles is analyzed by calculating the mass of these S-rich particles and the total dust mass. Finally, the ratios of masses of S-rich particles to total dust mass plotted against particle size to get size resolved information on mixing state of sulfate particles.

11 Results and Discussion- Atmospheric measurements

In this chapter, measurements with respect to atmospheric processes analyzed from the Flat plate sampler (if not otherwise stated) is presented. The reason why the Flat plate sampler is chosen is that, most data is available from the sampler.

11.1 Fraction of mineral dust in the samples

Mineral dust was the dominating particle type during this campaign. Figure 53 shows the size resolved deposition rate partitioned by mineral dust aerosol and total dust mass over different measurement days (dust event and non-dust days). As becomes clear from the figure, over 98 % of the dust mass is mineral dust aerosol in size ranges in both dust event and non-dust days.

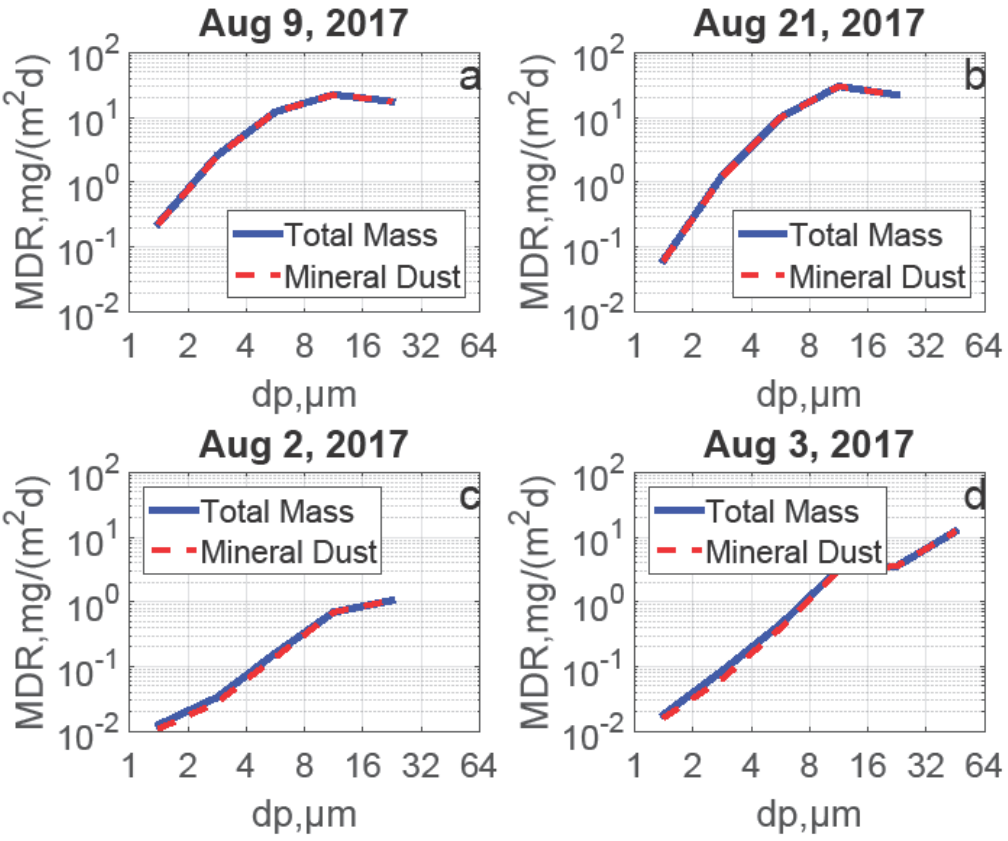

Figure 53**:** Size resolved deposition rate partitioned by mineral dust aerosol and total dust mass. Dust event days (a and b) and non-dust days (c and d).

11.2 Chemical composition

As indicated in the Figure 53, the dust mass is mainly dominated by mineral dust aerosol particles and therefore in the calculations, I assumed the fraction of non-dust particles to be negligible. Furthermore, hygroscopicity was not taken into account, as due to the mostly non-hygroscopic compounds and the moderate humidities their impact was rated low.

Figure 54 and Figure 55 show an overview of the relative proportions of the classes per unit of measurement series and overview of the group and relative proportions against the particle size. As expected, from the figure, it can be clearly seen that the overall mass composition is dominated by mineral dust aerosol particles during this campaign, mainly consisting of different classes of silicates, quartz-like, calcite-like, dolomite-like and gypsum-like particles as previous reports indicated for this location, which is quite similar to previous studies (Kandler et al., 2007; Petzold et al., 2009; Sokolik and Toon, 1999; Textor et al., 2006). For example, according to the study by Sokolik and Toon (1999), about 90% of total Saharan dust mass is composed of aluminosilicates, iron oxides and quartz particles. Furthermore, it is clear that there is no day-to-day variation in relative proportions of different classes of dust particles, confirming that dust aerosol particles are originating from the same source region.

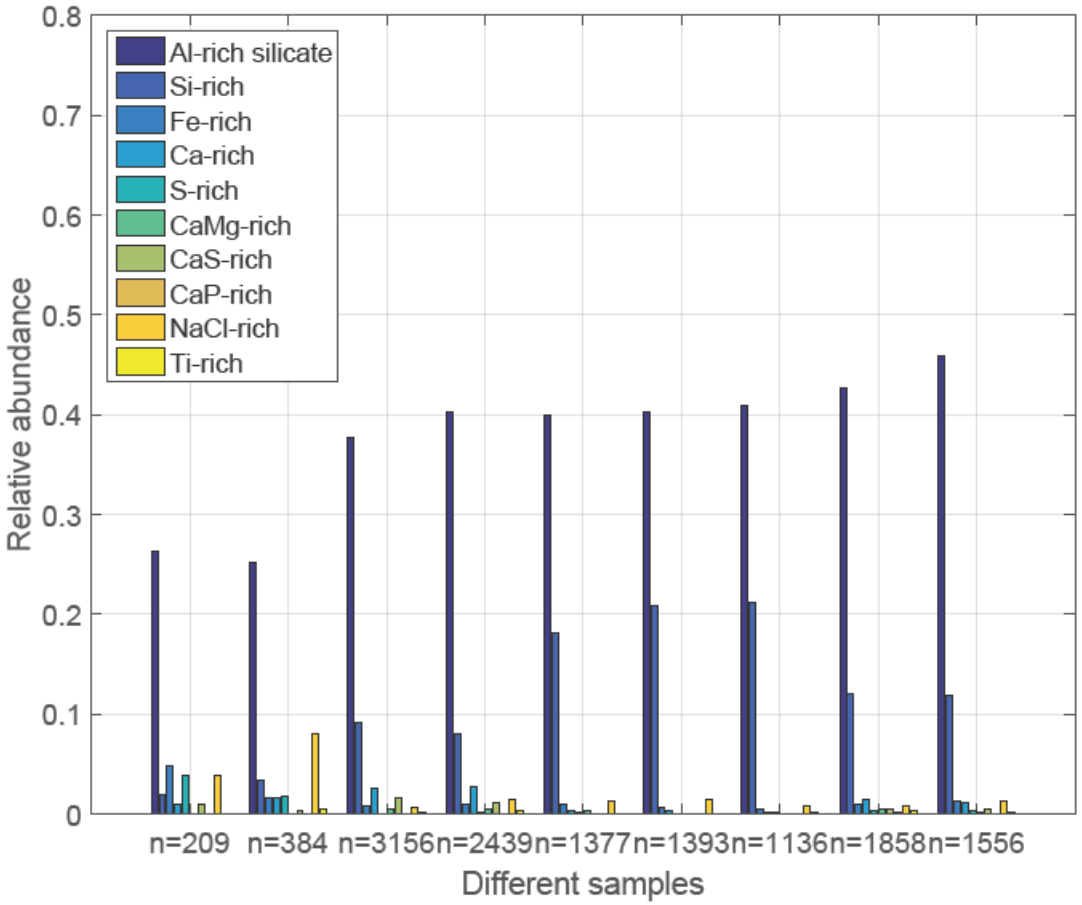

Figure 54: Chemical composition (relative number abundance of different particle groups) of dust particles per unit of measurement.

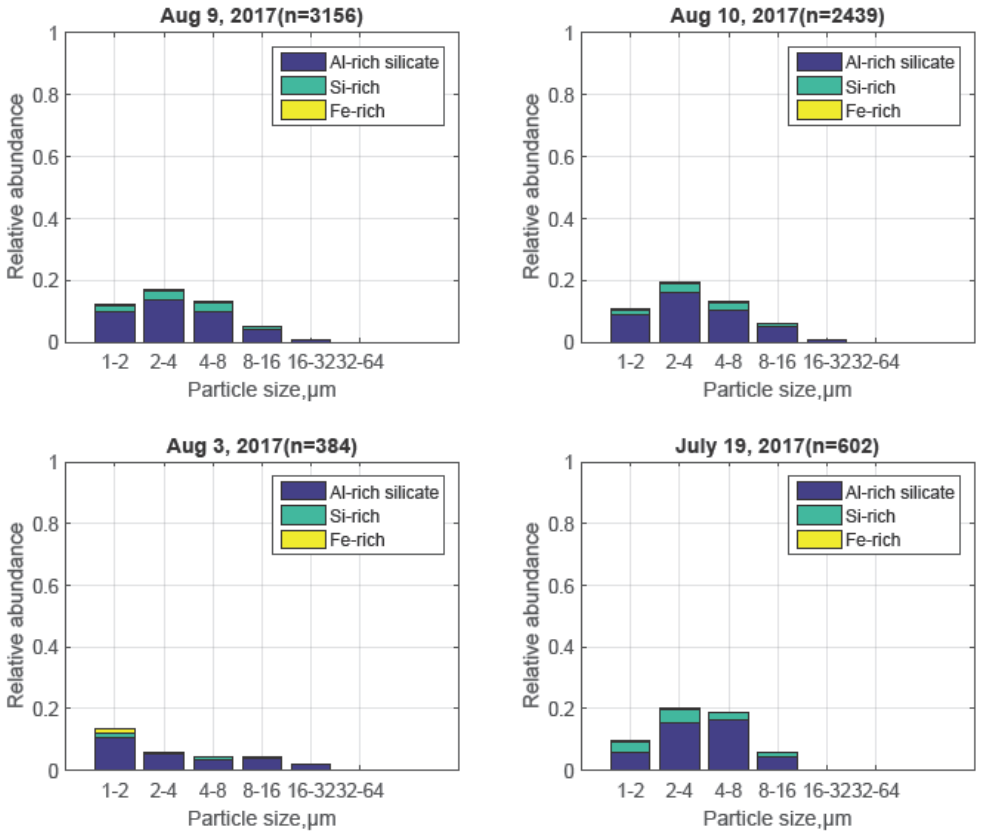

Figure 55: Size-resolved relative number abundance of the different particle groups analyzed over different measurement days (the upper two panels: dust day; the lower two panels: non-dust day).

In this perspective, Figure 56 and Figure 57 shows the comparison of number deposition rates and relative abundances of major dust aerosol components analyzed from different samplers. The analysis clearly indicates that the composition of dust aerosol particles remains largely unaffected by the sampler type.

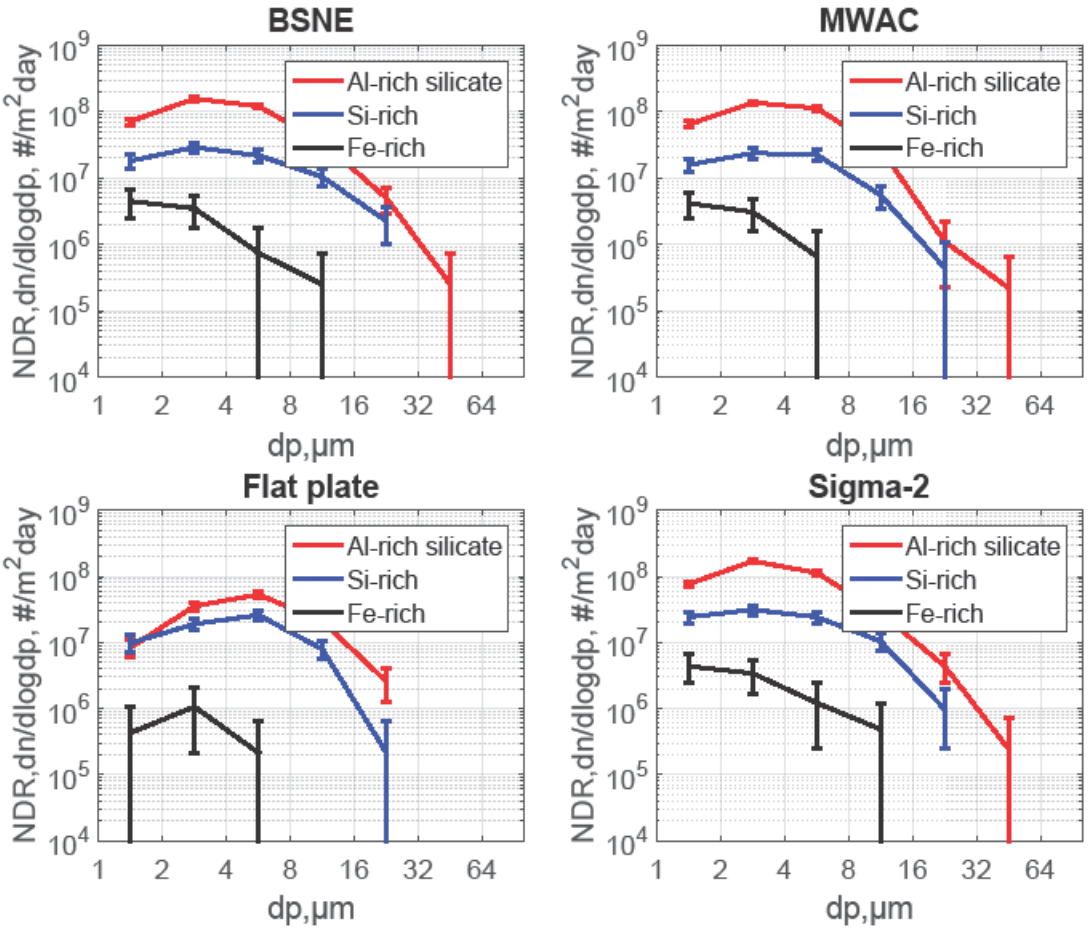

Figure 56: Comparing number deposition rates of major dust aerosol components among different samplers (Aug 21, 2017). The bars show the central 95% confidence interval of the daily variation.

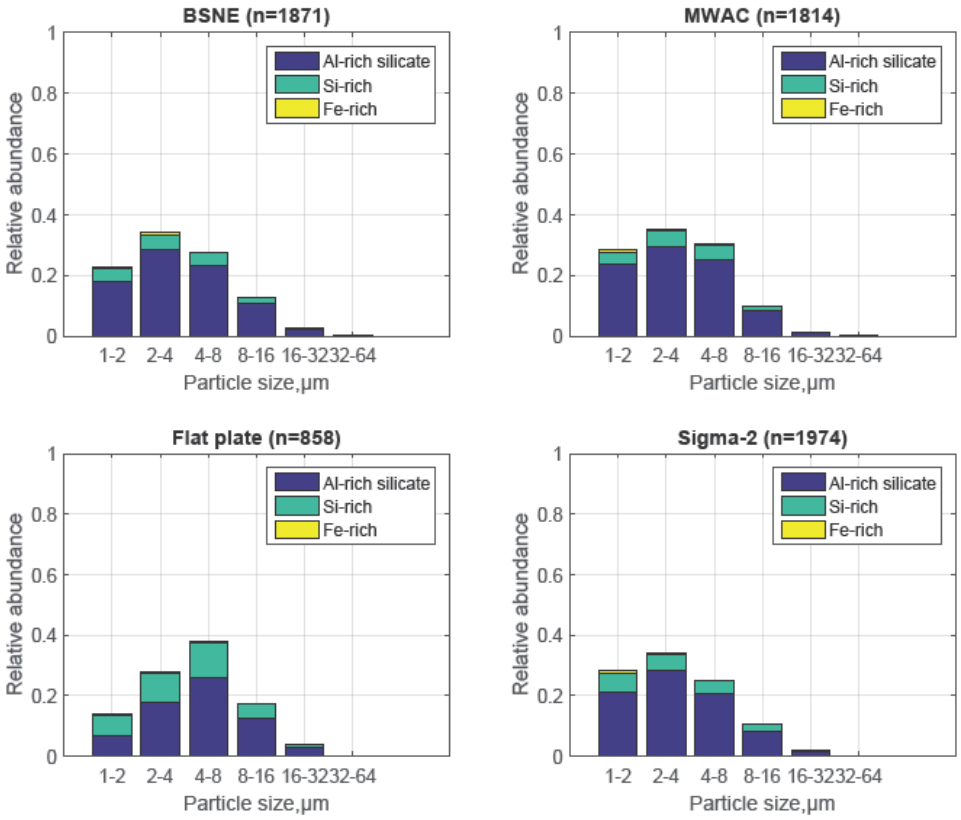

Figure 57: Comparing the relative abundance of major dust aerosol components among different samplers (Aug 21, 2017).

Because of Fe-rich particles are of much interest for the role in ocean productivity and biogeochemical cycle, the deposition rates of Fe-rich particles over different measurement days particularly analyzed as a function of particle size. Figure 58 shows size resolved deposition rates of Fe-rich particles over different measurement days. It is also evident from the graph that small amount of Fe-rich particles is also distinguished particularly for particles less than 8 μm in size which agrees well with the previous studies (Kandler et al., 2007). In this context, deposition rate ratios (see Figure 59) of Fe-rich to Si-rich particles and Fe-rich to Al-rich silicate particles show a decrease with increasing particle size. This indicates that there is a strong dependence of the chemical composition on the particle size.

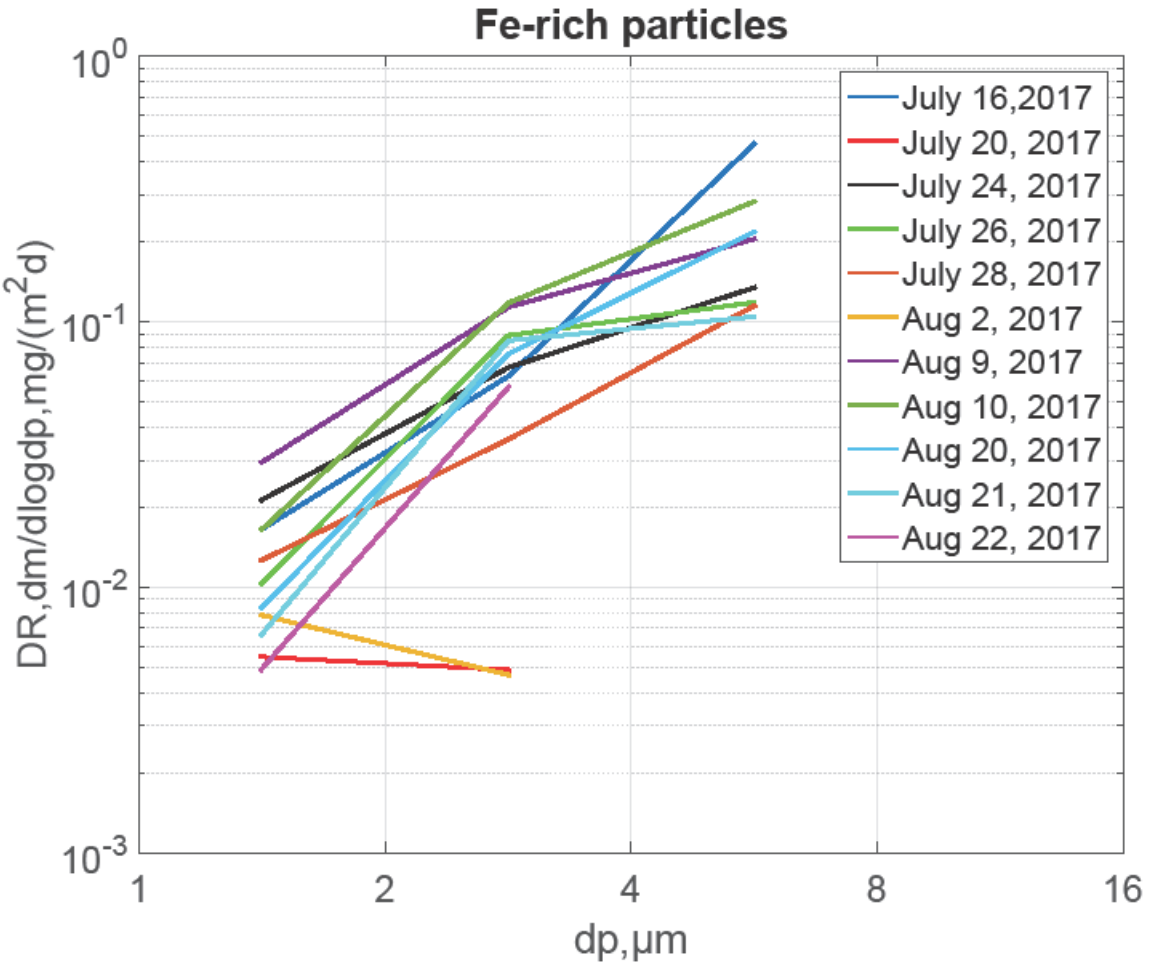

Figure 58**:** Size resolved deposition rate of Fe-rich particles over different measurement days.

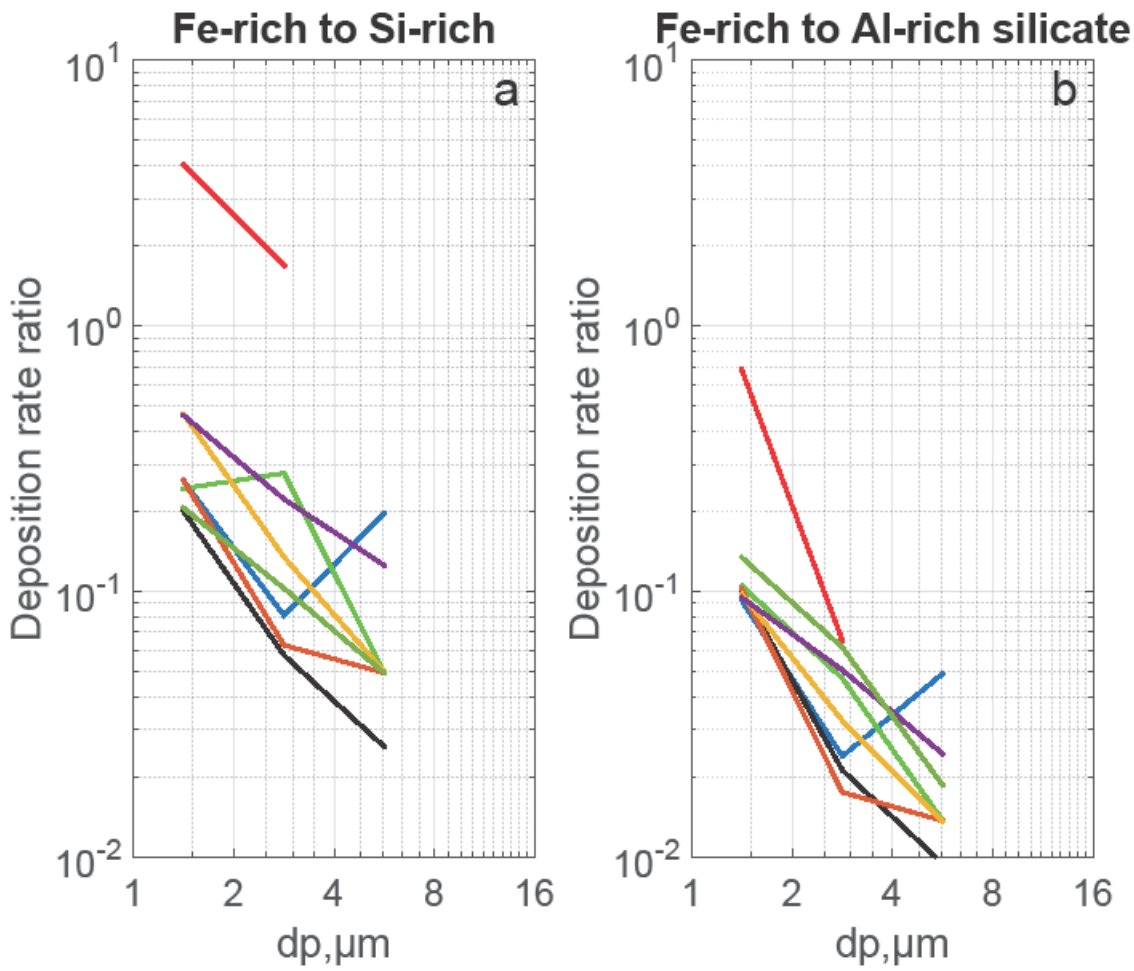

Figure 59: Deposition rate ratio of Fe-rich to Si-rich particles (a) and Al-rich silicate particles (b) analyzed over different measurement days. Colors represent different measurement days.

11.3 Determining the size distributions for mass concentration from the free-wing impactor measurements

11.3.1 Tenerife and Barbados measurements

Figure 60 shows comparisons of the mass concentration size distribution in between Tenerife (summer 2017) and Barbados derived from FWI measurements. From the graph, it is evident that in both regions, the size distribution peaks at approximately at the same size interval (8-16 µm). However, on average the two regions have different maximum average concentration values. Tenerife has maximum average concentration (a dM/dlogd) of 250 µg/m³ while Barbados has maximum average concentration (a dM/dlogd) of 25 µg/m³.

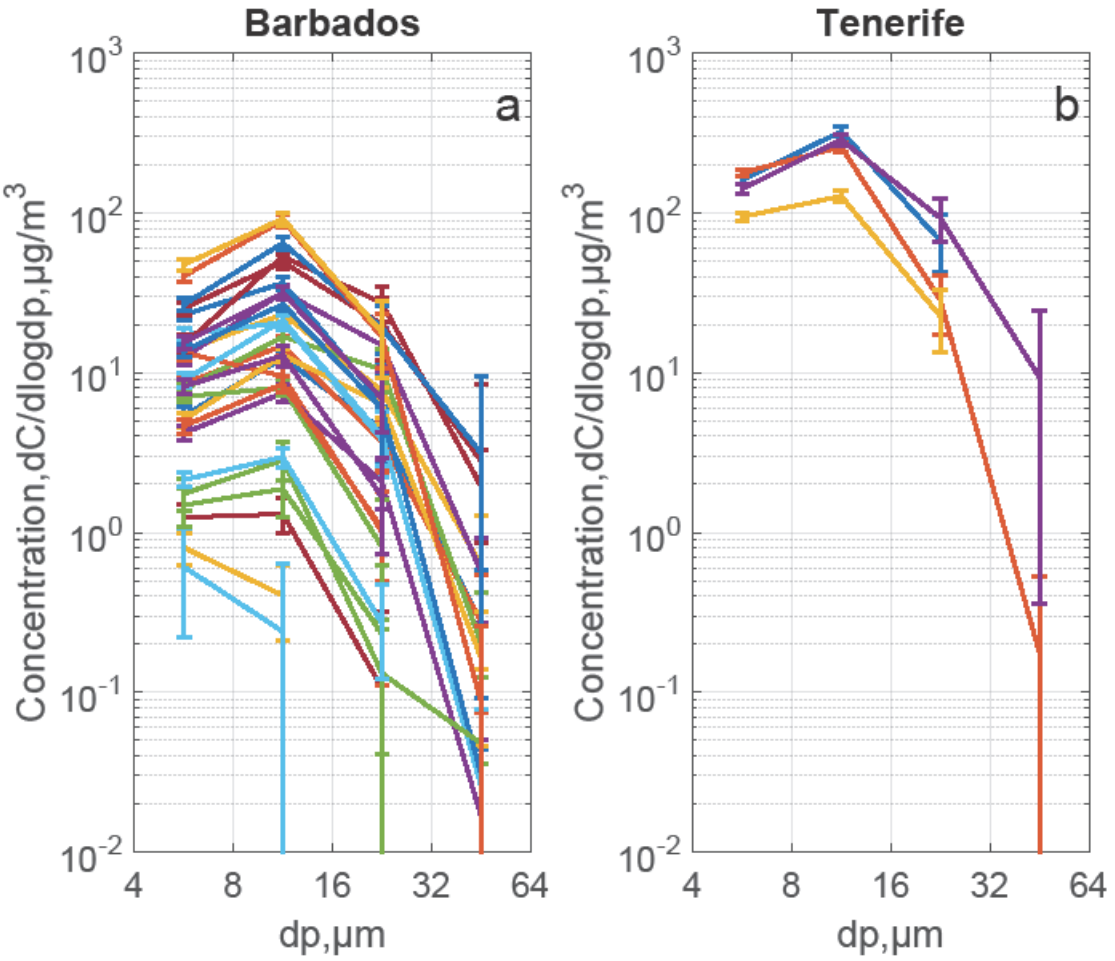

Figure 60: Comparison of daily average mass size distribution measurement (from FWI) between Barbados (a) and Tenerife (b). The bars show the central 95% confidence interval of the daily variation.

11.4 Complex index of refraction

The campaign average values of the real and imaginary parts of refractive index (RI) values as a function of particle size and wavelength given in Figure 61, Figure 62, Figure 63, Figure 64, Figure 65 and Figure 66 (for the daily variation , see also Figure A 1, Figure A 2, Figure A 3, Figure A 4, Figure A 5, Figure A 6 and Figure A 7 in the appendix). From the figures it can be clearly seen that the real ((n(λ)) and imaginary ((k(λ)) parts show different values at different wavelengths. The real (n(λ)) and imaginary (k(λ)) parts show similar spectral behavior, in that both n(λ) and k(λ) at lower wavelengths have higher values. In addition, both the real and imaginary part of complex refractive index shows a continuous decrease towards increasing wavelength. At lower wavelength, the real part of refractive index ((n(λ)) is close to 1.6 while, for imaginary part (for iron oxide particles), the refractive index (k(λ)) is close to 3.2*10-4. In comparison to the real part, at higher wavelength, the refractive index values for

both real and imaginary parts is less than the reported values at lower wavelength showing the lower absorption of dust particles at higher wavelengths.

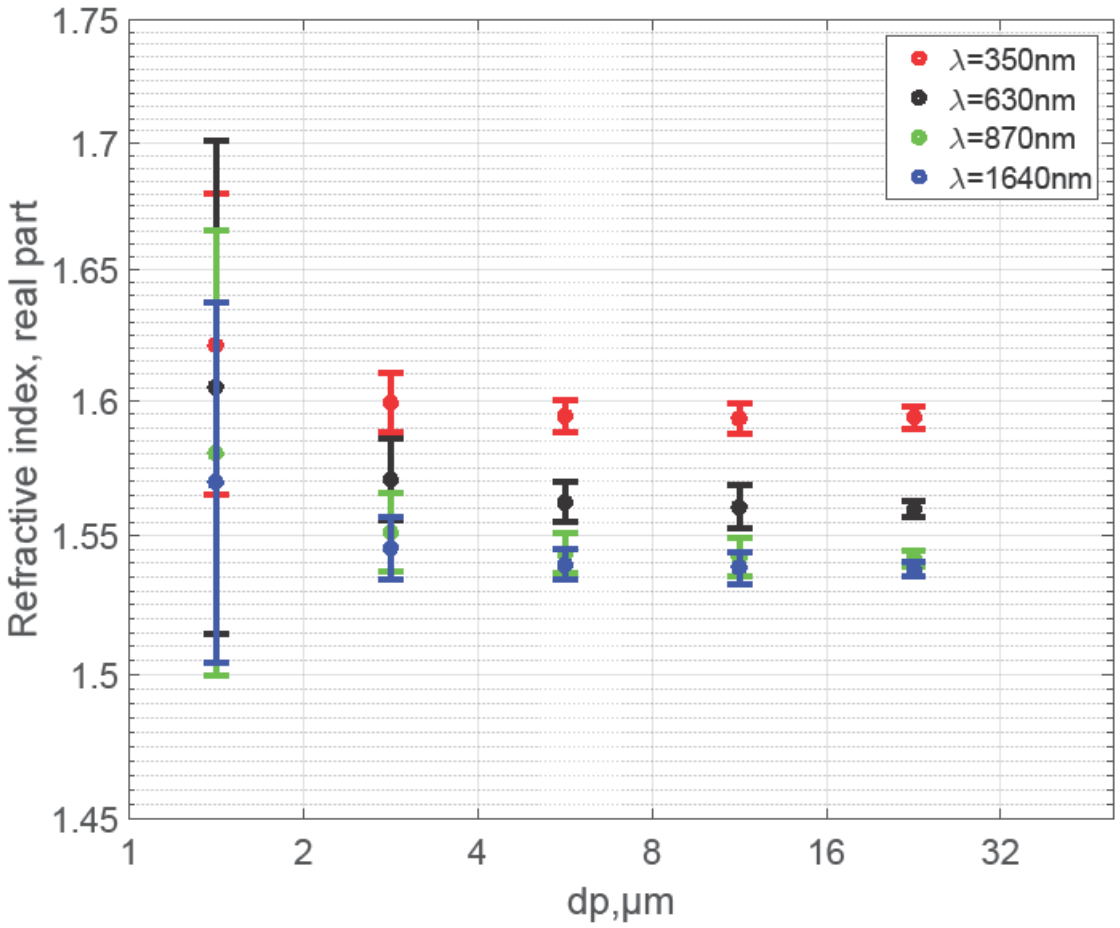

Figure 61: Size-resolved average complex refractive index (real part) analyzed at different wavelengths (Campaign average). The bars show the central 95% confidence interval of the daily variation.

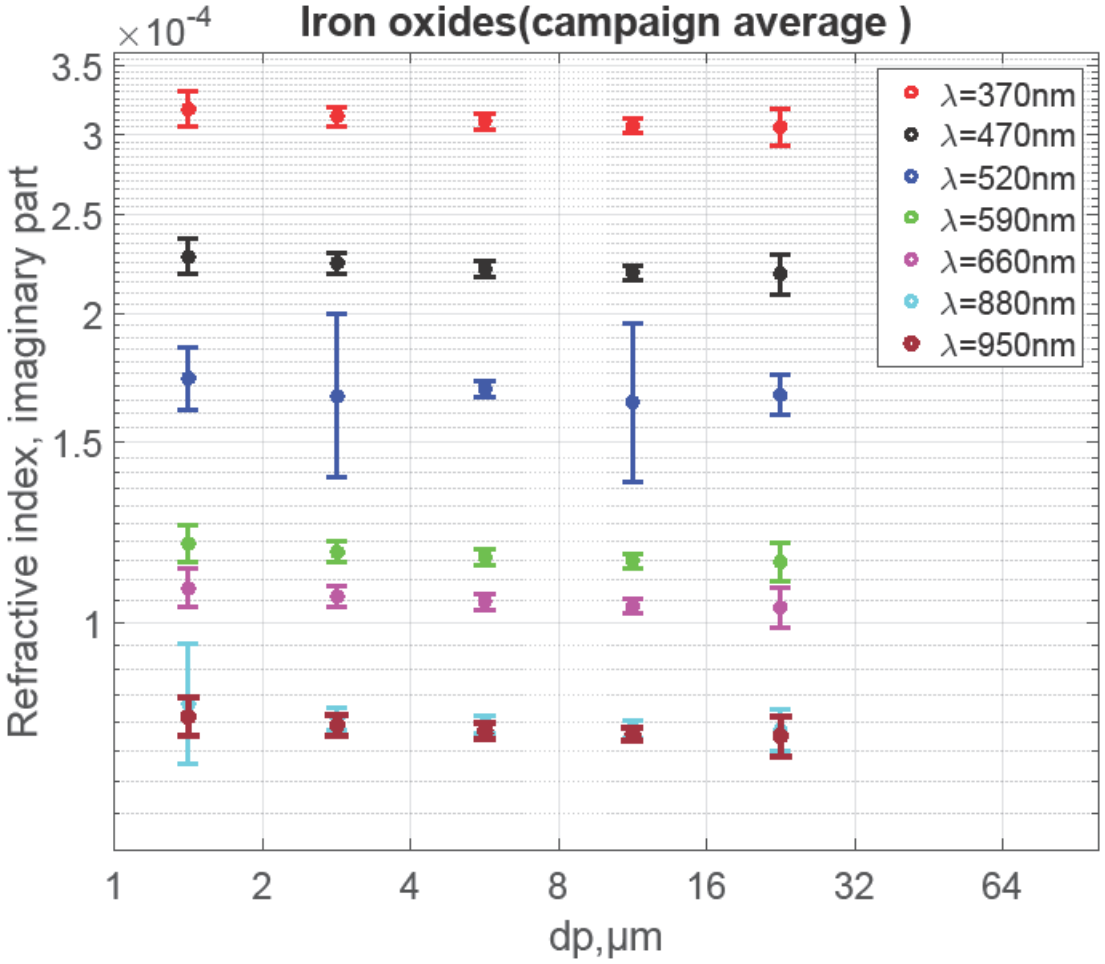

Figure 62: Size-resolved average complex refractive index (imaginary part) of Iron oxide particles analyzed at different wavelengths (Campaign average). The bars show the central 95% confidence interval of the daily variation.

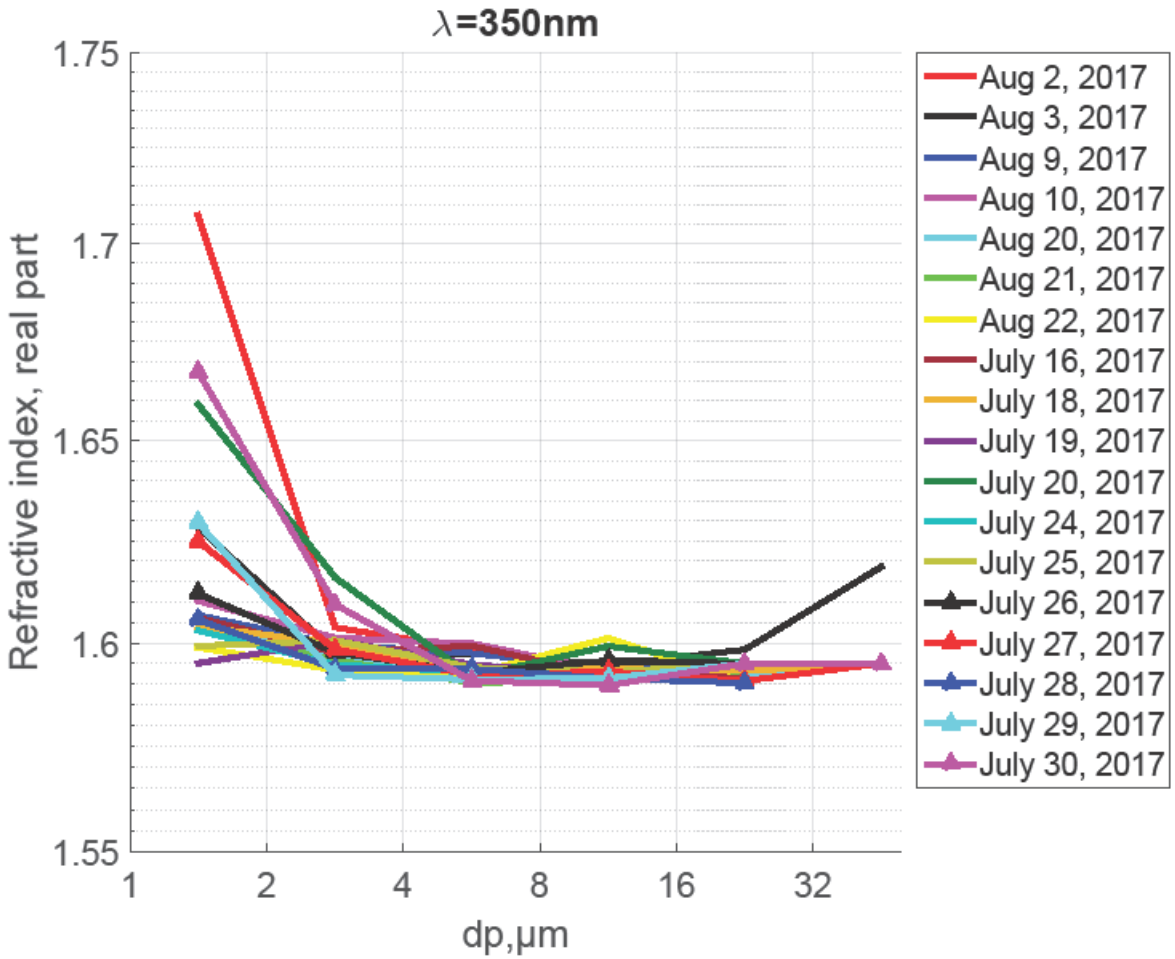

Figure 63: Average complex refractive index (real part) analyzed over different days (at wavelength=350 nm).

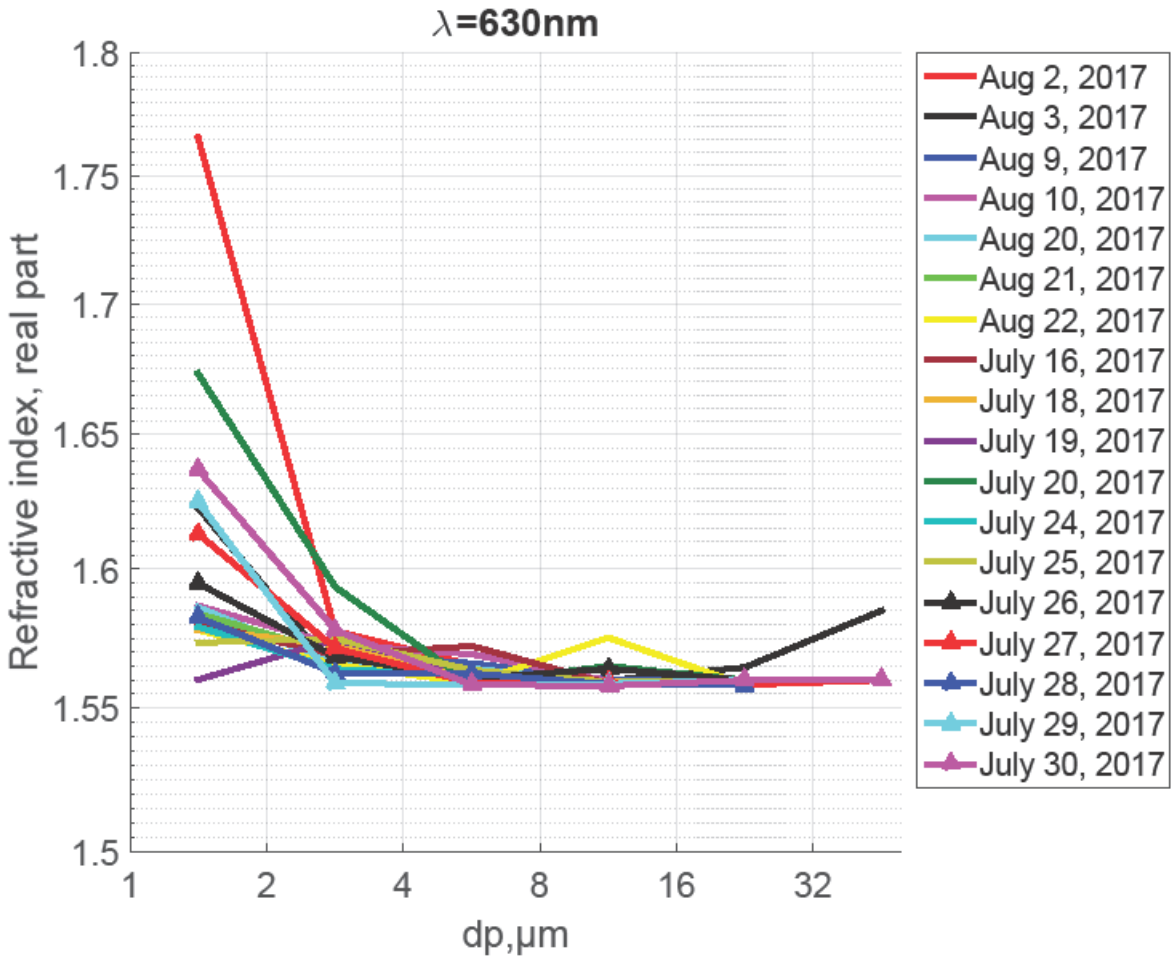

Figure 64: Average complex refractive index (real part) analyzed over different days (at wavelength=630 nm).

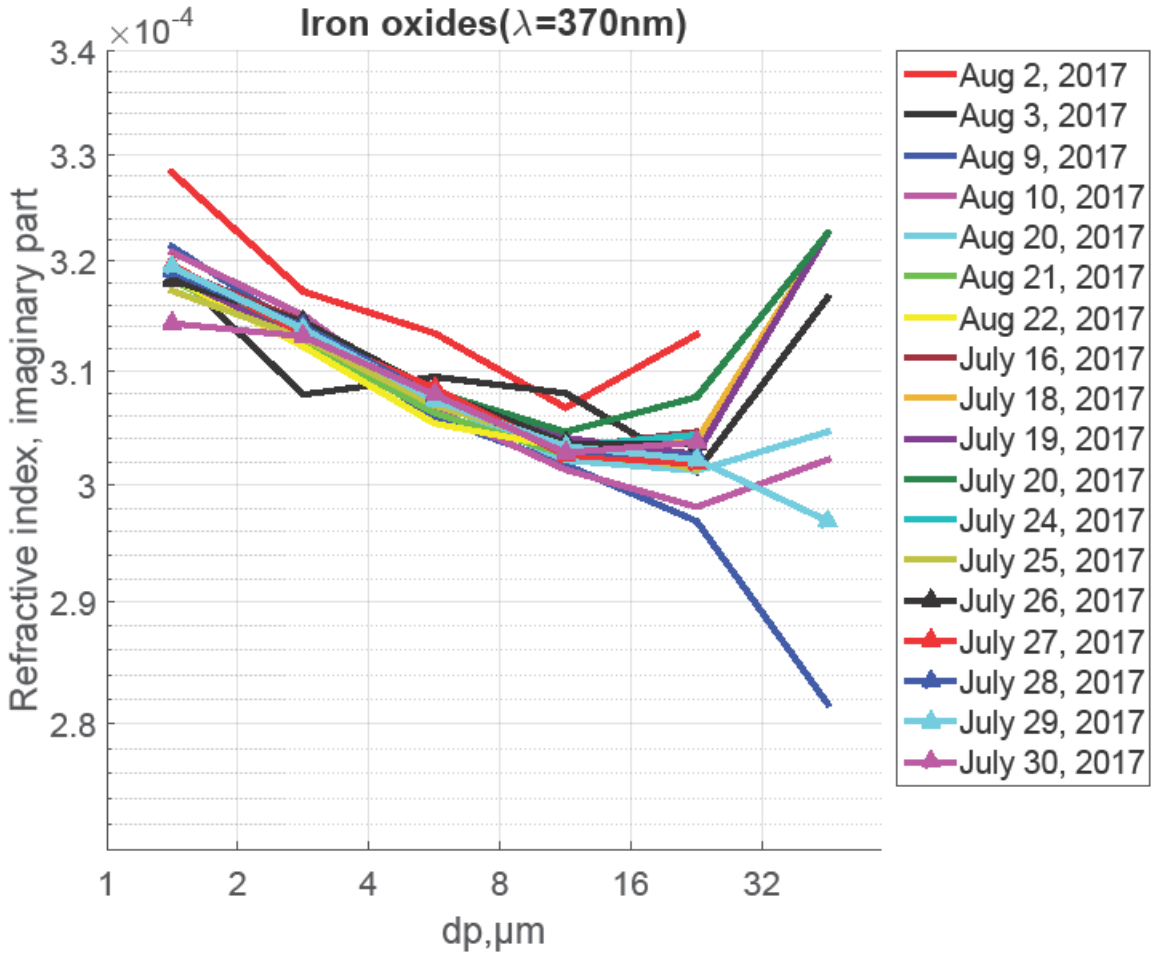

Figure 65: Average complex refractive index (imaginary part) analyzed over different days (at wavelength=370 nm).

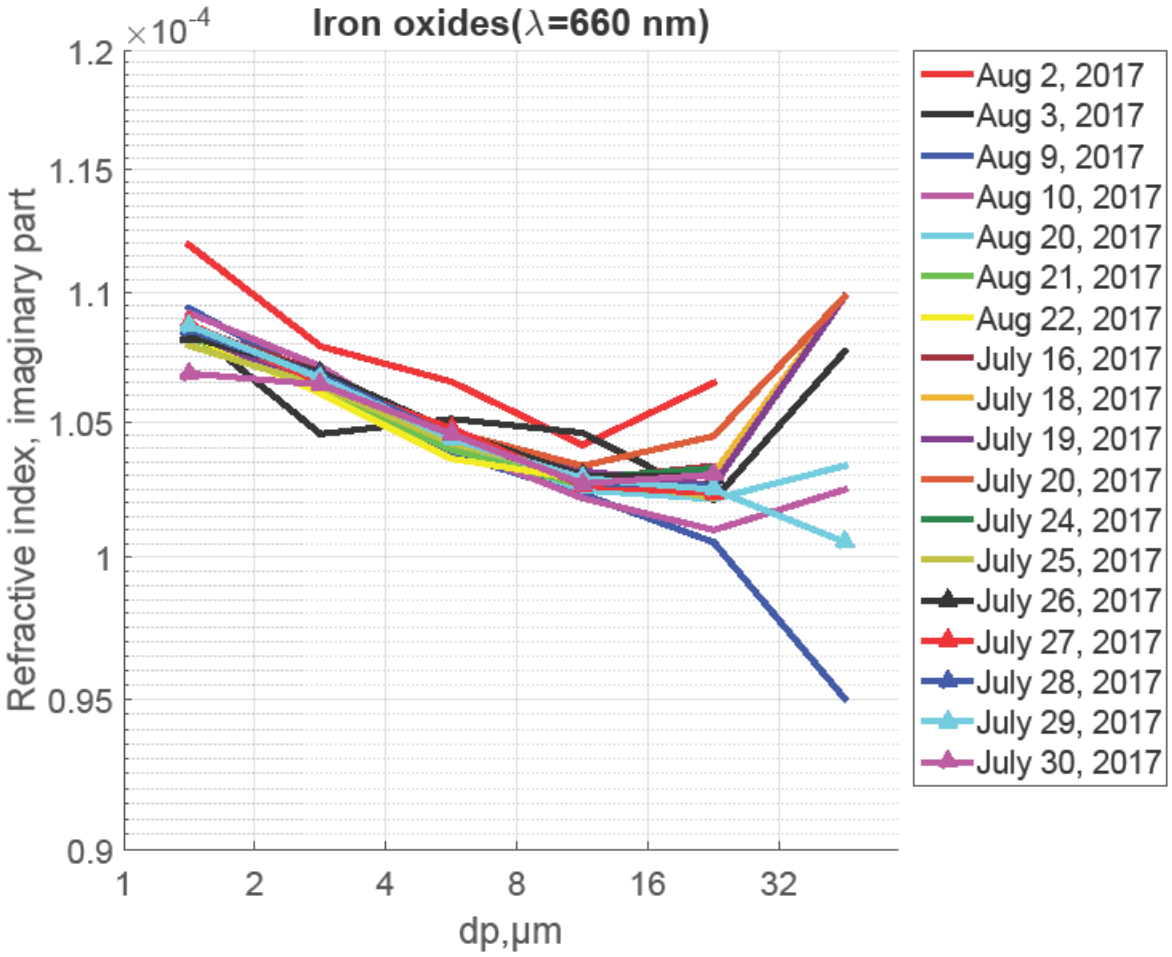

Figure 66: Average complex refractive index (imaginary part) analyzed over different days (at wavelength=660 nm).

11.5 Aerosol potential buffering

In Figure 67 (see also Figure A 8 for the campaign data sets), Fe index class is plotted vs Ca index class, colored according to the aerosol Ca^{2+} Mg^{2+} SO_4^{2-} relative balance. The area of the black circle is the total Fe mass in the particular index range, the area of the colored circle is the total Ca mass, the color scale is the Ca^{2+} Mg^{2+} SO_4^{2-} relative balance index. From the figure, it can be seen that most of the iron particles (the bottom region) carry a little calcium, while some iron particles do not carry calcium at all. Similarly, most of the calcium (mostly in top region) carry little Fe while some are totally not in contact with much iron. The message that can be learned from this figure is that:

- A part of the iron is in particles, which do not contain calcium, so acids getting onto these particles can directly react with the iron.

- Some particles contain iron and (unprocessed) calcium, so acids getting onto these can react with the Ca first, before reacting with Fe.
- Some particles contain Fe and processed Ca (as gypsum), so even in these particle Ca is available, it would not react any more with acids and therefore the acids can react directly with the Fe.

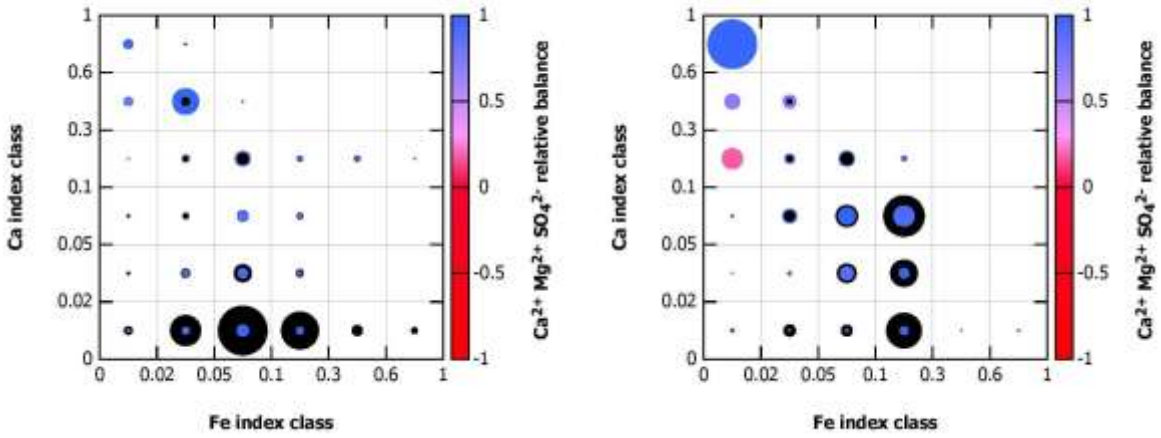

Figure 67: Mixing state of iron (black circles) and calcium (colored circles) as functions of Ca and Fe indices (colored according to the aerosol Ca^{2+} Mg^{2+} SO_4^{2-} relative balance). The circle area is proportional to total iron or calcium mass found in each class, normalized to the highest mass for each sampling location. The blue-red transition shows the average relative ion balance of Ca^{2+} + Mg^{2+} versus SO_4^{2-}, indicating an atmospheric processing. Left panel: dust day (July 24, 2017); Right panel: Non dust day (Aug 3, 2017).

In this context, Figure 68 demonstrates a conceptual models of possible acid processing for internal and external mixture of Fe and Ca particles. The model indicates that if we have only a few acids, the external Ca might be sufficient to buffer it. If we have a lot, it will overcome the carbonate buffer potential and as result Ca gets processed, but also, the non-Ca Fe particles might become processed, while in the Ca-Fe-particles, the Ca might protect the Fe for a while, but eventually when the processing time gets longer, the Fe might be processed at the end. In other words, the chemical processing of mineral dust aerosol particles in the atmosphere can be affected by environmental conditions and time.

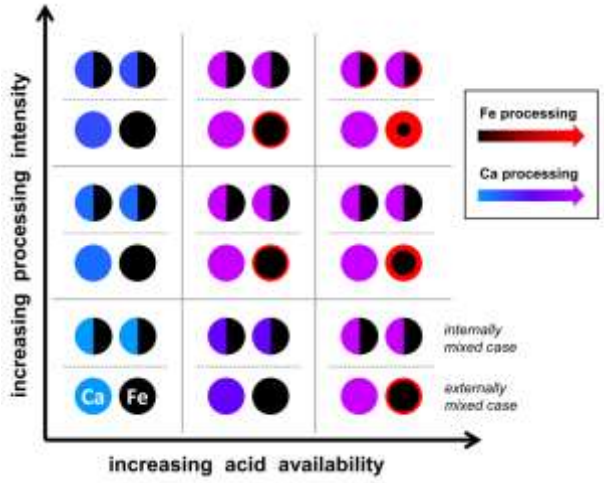

Figure 68: A Schematic diagram showing potential acid processing for dust particles mixed internal and external mixture with respect to calcium and iron particles (iron: black circles and calcium: colored circles).

11.6 Mixing of sulfate particles with dust

Internally mixing of dust particles with sulfate were investigated by analyzing the ratio of mass of sulfate particles in the individual particles to the total mass of the individual particles. Figure 69 (see also Figure 70 for daily variations) shows a relative mass contribution of S particles to the total dust aerosol particle (e.g., ratio of sulfate mass to the total dust particle mass) as a function of particle size. From the graph, it is evident that there is a weak trend with the sulfate, getting a little less for larger particles. With decreasing particle size, sulfate particle become more important. This implies that only fine mode sulfate is internally mixed with mineral dust aerosol particles, in the contrary, coarse particles associated with lower sulfur contents. In support of our result, there are also reports that show lesser sulfate particles (e.g., NH_4NO_3 and $(NH_4)_2SO_4$) can be present in coatings of dust mineral particles (Sullivan et al., 2007). Moreover, Dall'Osto et al. (2010) also suggested that sulfate particles may also be present as a minor proportion of mineral dust aerosol particles particularly originating from Africa and Asia.

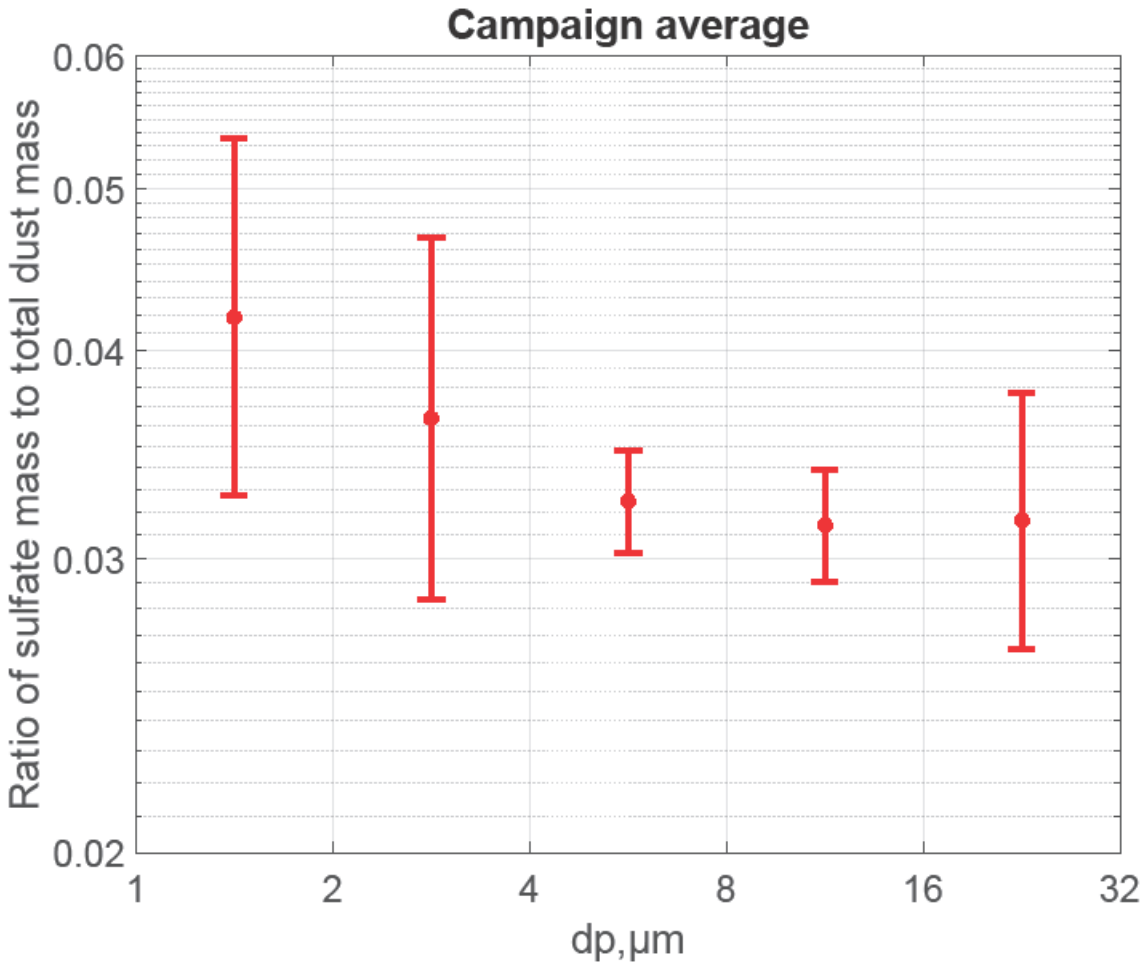

Figure 69: Relative mass contribution of sulfate particles to total dust aerosol mass (Campaign average). The bars show the central 95% confidence interval of the daily variation.

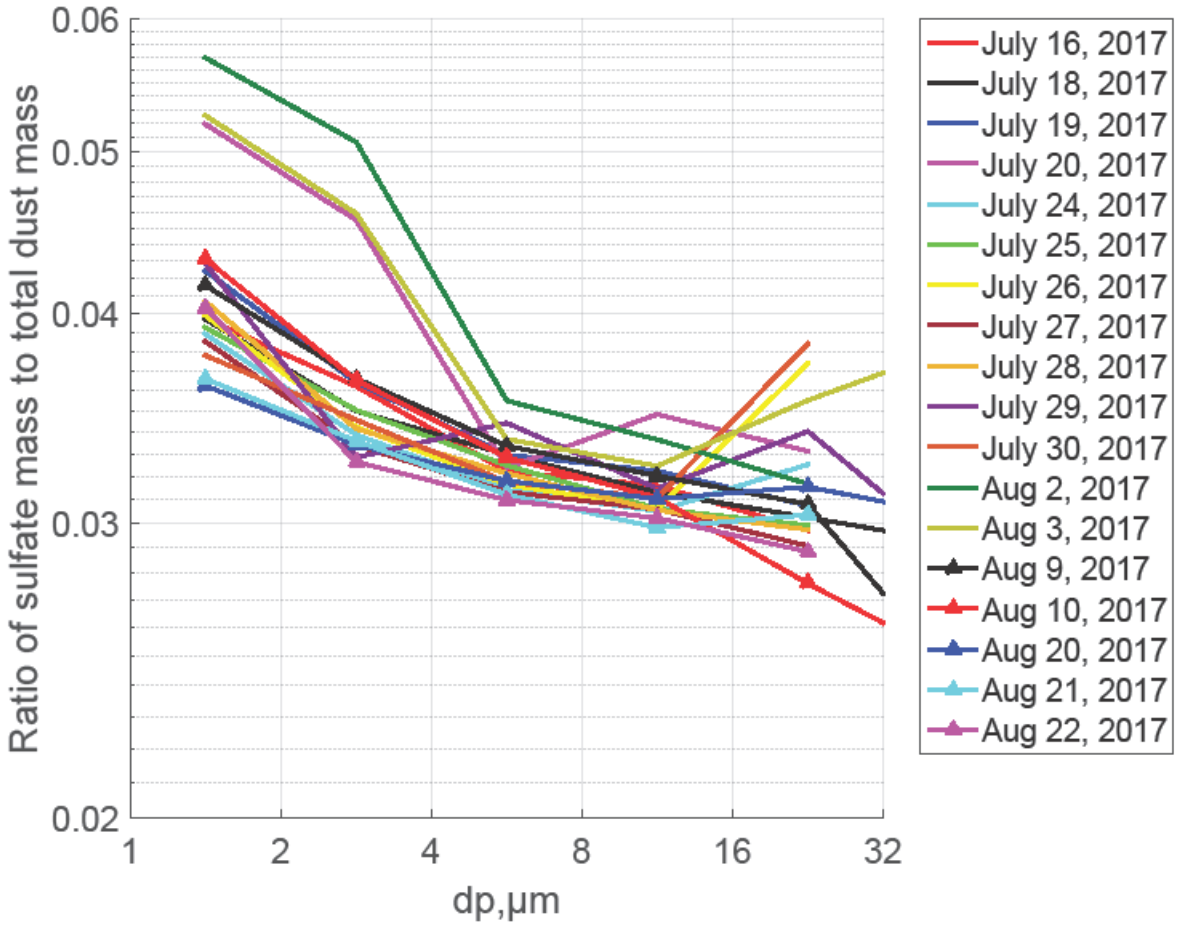

Figure 70: Relative mass contribution of sulfate particles to total dust aerosol mass shown for different sampling days.

12 Conclusions and future outlook

12.1 Conclusions

Parallel dust aerosol deposition measurements by means of deposition and other passive samplers were conducted at Izaña Global Atmospheric Watch Observatory continuously from 14th of July to 24th of August 2017. In addition, active aerosol collection was done with a free-wing impactor and an iso-axial filter sampler. Additional information regarding the aerosol particle size distributions has been obtained by an OPC. 316,000 single particles from 6 different samplers are analyzed by SEM-EDX, yielding size resolved deposition rates.

As known from previous studies, the total deposition rate was dominated by coarse particles (8-16 µm). A high temporal daily variability in total dust deposition rate is observed. The size resolved deposition rate measurements of different passive samplers varied significantly between the samplers under the same conditions. This is in principle expected from the different sampler construction. Applying suitable deposition velocity models, atmospheric concentrations were calculated from different sampler deposition rates. The resulting concentrations on average are in better agreement between the samplers than the deposition rates. However, discrepancies beyond the measurement uncertainty remain unexplained by the deposition models, in particular with respect to dependency on wind speed, which is predicted by the models, but not observed. The estimation of an appropriate deposition velocity from different models for calculating atmospheric concentrations remains obviously a challenge. In particular, when considering the size-resolved deposition velocities and deposition rate ratios, great discrepancies show up.

In the PM_{10} size range, a good agreement is found between the calculated concentrations for samples from different passive and the concentrations measured using an OPC. For particle sizes above PM_{10}, the comparison of the deposition-derived size distributions with impactor and filter measurements shows considerable underestimates of the deposition samplers, which must be interpreted as overestimation of the large-particle deposition velocities.

Deposition velocities from different analytical deposition models are compared to ones calculated using computational fluid dynamics simulations for different samplers. The comparison shows that two methods largely disagree. Moreover, all theory-based deposition

velocities (analytical as well as CFD approaches) fail to represent the observed measurement differences between the samplers. This obviously points to the need of better understanding the physics of dry deposition in general.

The correlation analysis between dust deposition rate, dust concentrations and wind speed reveals that the variation in deposition rate is mainly controlled by changes in concentration; variations in wind speed play a minor role for wind speeds lower than 6 m/s.

The correlation analysis between deposition rates and OPC measurements demonstrates that BSNE and Sigma-2 can be a good option for PM_{10} measurement, while the MWAC is not a suitable option. Apart from that result with respect to the PM_{10} size range, no recommendation for a least biased general purpose deposition sampler can be derived from our study.

Moreover, as the results show that the different samplers can't deliver consistent results between the sampler types, a recommendation must be that if a certain sampler type is chosen for a study, it should not be modified or replaced by another one for the sake of consistency of results, even if it was shown that the results do not agree well for example with active sampling.

During this study, it is also found that mineral dust particles are found to be the dominating particle type mainly composed of various classes of silicates, quartz-like, calcite-like, dolomite-like and gypsum-like particles in agreement with the previous studies in the region.

Size resolved refractive indices are modelled from the chemical composition of dust particles. Both real and imaginary parts of the refractive indices decrease with increasing wavelength. The values for imaginary part (k) ranges from $3.28*10^{-4}$ to $2.82*10^{-4}$ at 370 nm, $2.37*10^{-4}$ to $2.00*10^{-4}$ nm at 470 nm, $1.81*10^{-4}$ to $1.54*10^{-4}$ at 520 nm, $1.23*10^{-4}$ to 1. $*10^{-4}$ at 590 nm, $1.12*10^{-4}$ to $9.50*10^{-4}$ at 660 nm, $8.52*10^{-4}$ to $7.19*10^{-5}$ at 880 nm, $8.38*10^{-5}$ to $7.11*10^{-4}$ at 950 nm. Similarly, the values for real part (m) ranges from 1.71 to 1.59 at 250 nm, 1.77 to 1.56 at 630 nm, 1.72 to 1.54 nm at 870 nm and 1.68 to 1.53 at 1640 nm. Generally, in both cases, the values are wavelength dependent, showing a decrease with increasing wavelength. Also, there is a slight decrease in RI values with increasing particle size. I believe that such a decrease in the k value of iron oxide particles with particle size is mostly related to differences in the dust's iron content (e.g., iron content shows a decrease with an increase in particle size). Furthermore, the results show that the complex refractive index (both the real and imaginary parts) does not show a large vary from sample to sample. Generally, the average complex

refractive index calculated from single particle measurement is in good agreement with the previous measurement.

In this study, the potential for buffering of carbonate dust aerosol particles on the acid mobilization of iron particles has been investigated. The result points out that the buffering potential depends on atmospheric conditions and time. In this connection, by analyzing the ratio of sulfate mass to the total mass of dust of individual particles with the particle sizes, the mixing state of sulfate particles to the total dust particles were investigated. The analysis revealed that the finer dust particles were associated with higher content of S, while the coarse dust particles corresponds to lower S contents revealing only fine mode sulfate is internally mixed with mineral dust aerosol particles.

Overall, the results show that passive sampling techniques coupled with an automated single particle analysis provides insights into the variation of size distribution, deposition rate and concentration of atmospheric particles.

12.2 Outlook

From the deposition measurement presented in this study, our understanding about collection properties of different deposition and other passive samplers is greatly improved. However, we still feel that there are some questions that need further work and thus I recommend that the following issues should be of focus for the future works.

- The primary expectation of our study was that the passive samplers used in this study could be capable of measuring size resolved particle concentration above PM_{10} size range, but the result shows the samplers are not capable of measuring concentration above the PM_{10} size range. Therefore, further work needs to be done to gain a full understanding of why they can't be used for measuring concentration above PM_{10} size range.
- Differences among deposition velocity models show that there is a clear need for further work on the models for a better understanding of the treatment of deposition processes in models.
- Because of resource limitations, the CFD analysis has been performed only for the three geometries (samplers) excluding the BSNE sampler. So to make the comparison complete, I recommend the CFD simulation work for the BSNE geometry too.

Furthermore, from the CFD simulation work, it is not possible to see the influence of wind speed on Sigma-2 sampler. Therefore, I recommend further research to have more understanding on the influence of wind speed on Sigma-2 sampler.

- While for an integrated bulk measurement or the PM_{10} size range at least a qualitative agreement between the samplers can be reached, no model – analytical nor CFD – is able to explain the observed sampler-specific variations in deposition rate. Clearly, a better physical understanding is needed here and therefore a further work on this part is important.
- Some of the classical deposition models are not suitable to treat particles above PM_{10} size range (for example, the Wagner deposition velocity is not meaningful for particles > 30-40 µm), therefore I suggest further work on those deposition velocity models that they could be applied to particles in all size range.

Literature

Aluko, O. and Noll, K. E.: Deposition and suspension of large, airborne particles, Aerosol Sci. Technol. , 40, 503-513, 2006.

Arimoto, R.: Eolian dust and climate: relationships to sources, tropospheric chemistry, transport and deposition, Earth Sci Rev. , 54, 29-42, 2001.

Arya, S.: Suggested revisions to certain boundary layer parameterization schemes used in atmospheric circulation models, Mon Weather Rev., 105, 215-227, 1977.

Axson, J. L., Shen, H., Bondy, A. L., Landry, C. C., Welz, J., Creamean, J. M., and Ault, A. P.: Transported mineral dust deposition case study at a hydrologically sensitive mountain site: Size and composition shifts in ambient aerosol and snowpack, Aerosol Air Qual. Res., 2016. 2016.

Belyaev, S. and Levin, L.: Techniques for collection of representative aerosol samples, J. Aerosol Sci., 5, 325-338, 1974.

Bergamaschi, P., Bräunlich, M., Marik, T., and Brenninkmeijer, C. A.: Measurements of the carbon and hydrogen isotopes of atmospheric methane at Izaña, Tenerife: Seasonal cycles and synoptic-scale variations, J Geophys Res Atmos., 105, 14531-14546, 2000.

Boy, J. and Wilcke, W.: Tropical Andean forest derives calcium and magnesium from Saharan dust, Glob. Biogeochem. Cycles 22, 2008.

Bristow, L. A., Mohr, W., Ahmerkamp, S., and Kuypers, M. M.: Nutrients that limit growth in the ocean, Curr. Biol., 27, R474-R478, 2017.

Businger, J.: Evaluation of the accuracy with which dry deposition can be measured with current micrometeorological techniques, J. Clim. Appl. Meteorol., 25, 1100-1124, 1986.

Cellier, P. and Brunet, Y.: Flux-gradient relationships above tall plant canopies, Agric. For. Meteorol., 58, 93-117, 1992.

Chmielewski, M. and Gieras, M.: Three-zonal wall function for k-ε turbulence models, CMST, 19, 107-114, 2013.

Cotrim da Cunha, L., Buitenhuis, E. T., Le Quéré, C., Giraud, X., and Ludwig, W.: Potential impact of changes in river nutrient supply on global ocean biogeochemistry, Glob. Biogeochem. Cycles, 21, 2007.

Dall'Osto, M., Harrison, R. M., Highwood, E. J., O'Dowd, C., Ceburnis, D., Querol, X., and Achterberg, E. P.: Variation of the mixing state of Saharan dust particles with atmospheric transport, Atmos. Environ., 44, 3135-3146, 2010.

Dämmgen, U., Erisman, J. W., Cape, J. N., Grünhage, L., and Fowler, D.: Practical considerations for addressing uncertainties in monitoring bulk deposition, Environ. Pollut., 134, 535-548, 2005.

Davidson, C. I., Lindberg, S. E., Schmidt, J. A., Cartwright, L. G., and Landis, L. R.: Dry deposition of sulfate onto surrogate surfaces, J Geophys Res Atmos., 90, 2123-2130, 1985.

Davies, C.: Particle-fluid interaction, J. Aerosol Sci 10, 477-513, 1979.

Denjean, C., Formenti, P., Desboeufs, K., Chevaillier, S., Triquet, S., Maillé, M., Cazaunau, M., Laurent, B., Mayol-Bracero, O. L., and Vallejo, P.: Size distribution and optical properties of African mineral dust after intercontinental transport, J. Geophys. Res. Atmos., 121, 7117-7138, 2016.

Di Biagio, C., Formenti, P., Balkanski, Y., Caponi, L., Cazaunau, M., Pangui, E., Journet, E., Nowak, S., Andreae, M. O., Kandler, K., Saeed, T., Piketh, S., Seibert, D., Williams, E., and Doussin, J. F.: Complex refractive indices and single scattering albedo of global dust aerosols in the shortwave spectrum and relationship to iron content and size, Atmos. Chem. Phys. Discuss., 2019, 1-42, 2019.

Droppo, J. G.: Improved Formulations for Air-Surface Exchanges Related to National Security Needs: Dry Deposition Models, Pacific Northwest National Lab.(PNNL), Richland, WA (United States), 2006.

Dupont, S., Rajot, J. L., Labiadh, M., Bergametti, G., Alfaro, S., Bouet, C., Fernandes, R., Khalfallah, B., Lamaud, E., and Marticorena, B.: Aerodynamic Parameters Over an Eroding Bare Surface: Reconciliation of the Law of the Wall and Eddy Covariance Determinations, J. Geophys. Res. Atmos. , 123, 4490-4508, 2018.

Ebert, M., Weinbruch, S., Rausch, A., Gorzawski, G., Helas, G., Hoffmann, P., and Wex, H.: Complex refractive index of aerosols during LACE 98# x2010; as derived from the analysis of individual particles, J. Geophys. Res., 107, 2002.

Efron, B.: Bootstrap Methods: Another Look at the Jackknife, Ann. Statist., 7, 1-26, 1979.

Einstein, S. A., Yu, C.-H., Mainelis, G., Chen, L. C., Weisel, C. P., and Lioy, P. J.: Design and validation of a passive deposition sampler, J. Environ. Monit., 14, 2411-2420, 2012.

Ettling, D.: Theoretische Meteorologie, Vieweg, Braunschweig/Wiesbaden, 1996. 1996.

Falkowski, P., Scholes, R., Boyle, E., Canadell, J., Canfield, D., Elser, J., Gruber, N., Hibbard, K., Högberg, P., and Linder, S.: The global carbon cycle: a test of our knowledge of earth as a system, science, 290, 291-296, 2000.

Fluent, A.: Theory guide, Ansys Inc, 2015. 2015.

Franz, T. P., Eisenreich, S. J., and Holsen, T. M.: Dry deposition of particulate polychlorinated biphenyls and polycyclic aromatic hydrocarbons to Lake Michigan, Environ. Sci. Technol., 32, 3681-3688, 1998.

Gao, Y. and Anderson, J. R.: Characteristics of Chinese aerosols determined by individual-particle analysis, J. Geophys. Res. Atmos. , 106, 18037-18045, 2001.

Gao, Y., Kaufman, Y., Tanre, D., Kolber, D., and Falkowski, P.: Seasonal distributions of aeolian iron fluxes to the global ocean, Geophys. Res. Lett., 28, 29-32, 2001.

Giardina, M. and Buffa, P.: A new approach for modeling dry deposition velocity of particles, Atmos. Environ., 180, 11-22, 2018.

Goossens, D.: Relationships between horizontal transport flux and vertical deposition flux during dry deposition of atmospheric dust particles, J. Geophys. Res. F: Earth Surf., 113, 2008.

Goossens, D. and Offer, Z. Y.: An evaluation of the efficiency of some eolian dust collectors, Soil Technol., 7, 25-35, 1994.

Grousset, F. E., Ginoux, P., Bory, A., and Biscaye, P. E.: Case study of a Chinese dust plume reaching the French Alps, Geophys. Res. Lett., 30, 2003.

Hannah, L.: The Climate System and Climate Change. In: Climate change biology, Hannah, L. (Ed.), Academic Press, Burlington, MA, 2014.

Harrison, W. and Cota, G.: Primary production in polar waters: relation to nutrient availability, Polar Res., 10, 87-104, 1991.

Heinold, B., Tegen, I., Schepanski, K., and Banks, J. R.: New developments in the representation of Saharan dust sources in the aerosol–climate model ECHAM6-HAM2, Geosci. Model. Dev., 9, 765-777, 2016.

Hicks, B.: Measuring dry deposition: a re-assessment of the state of the art, Water Air Soil Pollut., 1986. 75-90, 1986.

Hinds, W. C.: Aerosol technology: properties, behavior, and measurement of airborne particles, John Wiley & Sons, 1999.

Holsen, T. M., Noll, K. E., Liu, S. P., and Lee, W. J.: Dry deposition of polychlorinated biphenyls in urban areas, Environ. Sci. Technol. , 25, 1075-1081, 1991.

Huang, J., Liu, Y., and Holsen, T. M.: Comparison between knife-edge and frisbee-shaped surrogate surfaces for making dry deposition measurements: Wind tunnel experiments and computational fluid dynamics (CFD) modeling, Atmos. Environ., 45, 4213-4219, 2011.

Huang, K., Zhuang, G., Li, J., Wang, Q., Sun, Y., Lin, Y., and Fu, J. S.: Mixing of Asian dust with pollution aerosol and the transformation of aerosol components during the dust storm over China in spring 2007, J Geophys Res Atmos, 115, 2010.

Ingall, E., Feng, Y., Longo, A., Lai, B., Shelley, R., Landing, W., Morton, P., Nenes, A., Mihalopoulos, N., and Violaki, K.: Enhanced Iron Solubility at Low pH in Global Aerosols, Atmosphere, 9, 201, 2018.

Ito, A. and Feng, Y.: Role of dust alkalinity in acid mobilization of iron, Atmos. Chem. Phys., 10, 9237-9250, 2010.

Jaszczur, M., Teneta, J., Styszko, K., Hassan, Q., Burzyńska, P., Marcinek, E., and Łopian, N.: The field experiments and model of the natural dust deposition effects on photovoltaic module efficiency, Environ. Sci. Pollut. Res., 26, 8402-8417, 2019.

Jickells, T., An, Z., Andersen, K. K., Baker, A., Bergametti, G., Brooks, N., Cao, J., Boyd, P., Duce, R., and Hunter, K.: Global iron connections between desert dust, ocean biogeochemistry, and climate, Science, 308, 67-71, 2005.

Junge, C.: Air Chemistry and Radioactivity. Academic Press, New York, 1963.

Kandler, K., Benker, N., Bundke, U., Cuevas, E., Ebert, M., Knippertz, P., Rodríguez, S., Schütz, L., and Weinbruch, S.: Chemical composition and complex refractive index of Saharan Mineral Dust at Izana, Tenerife (Spain) derived by electron microscopy, Atmos. Environ. , 41, 8058-8074, 2007.

Kandler, K., Schneiders, K., Ebert, M., Hartmann, M., Weinbruch, S., Prass, M., and Pöhlker, C.: Composition and mixing state of atmospheric aerosols determined by electron microscopy: method development and application to aged Saharan dust deposition in the Caribbean boundary layer, Atmos. Chem. Phys., 18, 2018.

Kandler, K., Schütz, L., Deutscher, C., Ebert, M., Hofmann, H., Jäckel, S., Jaenicke, R., Knippertz, P., Lieke, K., and Massling, A.: Size distribution, mass concentration, chemical and mineralogical composition and derived optical parameters of the boundary layer aerosol at Tinfou, Morocco, during SAMUM 2006, Tellus B Chem. Phys. Meteorol., 61, 32-50, 2009.

Klaver, A., Formenti, P., Caquineau, S., Chevaillier, S., Ausset, P., Calzolai, G., Osborne, S., Johnson, B., Harrison, M., and Dubovik, O.: Physico-chemical and optical properties of Sahelian and Saharan mineral dust: in situ measurements during the GERBILS campaign, Q. J. R. Meteorol. Soc., 137, 1193-1210, 2011.

Knippertz, P. and Stuut, J.: Mineral dust: A key player in the earth system, Springer, Dordrecht, 2014.

Kok, J. F., Parteli, E. J., Michaels, T. I., and Karam, D. B.: The physics of wind-blown sand and dust, Rep. Prog. Phys., 75, 106901, 2012.

Kouznetsov, R. and Sofiev, M.: A methodology for evaluation of vertical dispersion and dry deposition of atmospheric aerosols, J. Geophys. Res. Atmos., 117, 2012.

Krishnamurthy, A., Moore, J. K., Mahowald, N., Luo, C., Doney, S. C., Lindsay, K., and Zender, C. S.: Impacts of increasing anthropogenic soluble iron and nitrogen deposition on ocean biogeochemistry, Glob. Biogeochem. Cycles, 23, 2009.

Lai, A. and Nazaroff, W.: Supermicron particle deposition from turbulent chamber flow onto smooth and rough vertical surfaces, Atmos. Environ. , 39, 4893-4900, 2005.

Langmann, B.: Volcanic ash versus mineral dust: atmospheric processing and environmental and climate impacts, ISRN Atmos. Sci., 2013, 2013.

Lindqvist, H., Jokinen, O., Kandler, K., Scheuvens, D., and Nousiainen, T.: Single scattering by realistic, inhomogeneous mineral dust particles with stereogrammetric shapes, Atmos. Chem. Phys., 14, 143-157, 2014.

Liu, X., Huneeus, N., Schulz, M., Balkanski, Y., Griesfeller, J., Prospero, J., Kinne, S., Bauer, S., Boucher, O., and Chin, M.: Global dust model intercomparison in AeroCom phase I, Atmos. Chem. Phys., 11, 7781, 2011.

Lovett, G. M.: Atmospheric deposition of nutrients and pollutants in North America: an ecological perspective, Ecol. Appl., 4, 629-650, 1994.

Mahowald, N., Albani, S., Kok, J. F., Engelstaeder, S., Scanza, R., Ward, D. S., and Flanner, M. G.: The size distribution of desert dust aerosols and its impact on the Earth system, Aeolian Res. , 15, 53-71, 2014.

Mahowald, N. M., Baker, A. R., Bergametti, G., Brooks, N., Duce, R. A., Jickells, T. D., Kubilay, N., Prospero, J. M., and Tegen, I.: Atmospheric global dust cycle and iron inputs to the ocean, Glob. Biogeochem. Cycles, 19, 2005.

Malm, W. C., Day, D. E., Kreidenweis, S. M., Collett, J. L., and Lee, T.: Humidity-dependent optical properties of fine particles during the Big Bend Regional Aerosol and Visibility Observational Study, J Geophys Res Atmos, 108, 2003.

Meskhidze, N., Chameides, W., Nenes, A., and Chen, G.: Iron mobilization in mineral dust: Can anthropogenic SO2 emissions affect ocean productivity?, Geophys. Res. Lett., 30, 2003.

Mohan, S. M.: An overview of particulate dry deposition: measuring methods, deposition velocity and controlling factors, Int. J. Environ. Sci. Technol., 13, 387-402, 2016.

Müller, T., Schladitz, A., Massling, A., Kaaden, N., Kandler, K., and Wiedensohler, A.: Spectral absorption coefficients and imaginary parts of refractive indices of Saharan dust during SAMUM-1, Tellus, 61B, 61, 79-95, 2009.

Munn, R. and Bolin, B.: Global air pollution—meteorological aspects: a survey, Atmos. Environ., 5, 363-402, 1971.

Nenes, A., Krom, M. D., Mihalopoulos, N., Cappellen, P. V., Shi, Z., Bougiatioti, A., Zarmpas, P., and Herut, B.: Atmospheric acidification of mineral aerosols: a source of bioavailable phosphorus for the oceans, Atmos. Chem. Phys., 11, 6265-6272, 2011.

Neto, E. C.: Speeding up non-parametric bootstrap computations for statistics based on sample moments in small/moderate sample size applications, PLoS One, 10, e0131333, 2015.

Nicolas, M., Ndour, M., Ka, O., D'Anna, B., and George, C.: Photochemistry of atmospheric dust: ozone decomposition on illuminated titanium dioxide, Environ. Sci. Technol., 43, 7437-7442, 2009.

Niedermeier, N.: Experimental determination of the mass deposition flux of mineral dust at the Cape Verde Islands, 2014. 2014.

Noll, K. E. and Fang, K. Y.: Development of a dry deposition model for atmospheric coarse particles, Atmos. Environ., 23, 585-594, 1989.

Noll, K. E., Jackson, M. M., and Oskouie, A. K.: Development of an atmospheric particle dry deposition model, Aerosol Sci. Technol. , 35, 627-636, 2001.

Nousiainen, T.: Optical modeling of mineral dust particles: A review, J. Quant. Spectrosc. Ra., 110, 1261-1279, 2009.

Osada, K., Ura, S., Kagawa, M., Mikami, M., Tanaka, T., Matoba, S., Aoki, K., Shinoda, M., Kurosaki, Y., and Hayashi, M.: Wet and dry deposition of mineral dust particles in Japan: factors related to temporal variation and spatial distribution, Atmos. Chem. Phys., 14, 1107-1121, 2014.

Ott, D. K., Cyrs, W., and Peters, T. M.: Passive measurement of coarse particulate matter, PM10–2.5, J. Aerosol Sci 39, 156-167, 2008.

Penner, J. E., Andreae, M., Annegarn, H., Barrie, L., Feichter, J., Hegg, D., Jayaraman, A., Leaitch, R., Murphy, D., and Nganga, J.: Aerosols, their direct and indirect effects. In: Climate Change 2001: The Scientific Basis. Contribution of Working Group I to the Third Assessment Report of the Intergovernmental Panel on Climate Change, Cambridge University Press, 2001.

Petzold, A., Rasp, K., Weinzierl, B., Esselborn, M., Hamburger, T., DöRNBRACK, A., Kandler, K., SchuüTZ, L., Knippertz, P., and Fiebig, M.: Saharan dust absorption and refractive index from aircraft-based observations during SAMUM 2006, Tellus, 61B, 61, 118-130, 2009.

Piskunov, V.: Parameterization of aerosol dry deposition velocities onto smooth and rough surfaces, J. Aerosol Sci, 40, 664-679, 2009.

Pósfai, M., Axisa, D., Tompa, É., Freney, E., Bruintjes, R., and Buseck, P. R.: Interactions of mineral dust with pollution and clouds: An individual-particle TEM study of atmospheric aerosol from Saudi Arabia, Atmospheric Res., 122, 347-361, 2013.

Prospero, J. M., Ginoux, P., Torres, O., Nicholson, S. E., and Gill, T. E.: Environmental characterization of global sources of atmospheric soil dust identified with the Nimbus 7 Total Ozone Mapping Spectrometer (TOMS) absorbing aerosol product, Rev. Geophys., 40, 2-1-2-31, 2002.

Prospero, J. M., Landing, W. M., and Schulz, M.: African dust deposition to Florida: Temporal and spatial variability and comparisons to models, J. Geophys. Res. Atmos., 115, 2010.

Prospero, J. M., Schmitt, R., Cuevas, E., Savoie, D., Graustein, W., Turekian, K., Volz-Thomas, A., Diaz, A., Oltmans, S., and Levy, H.: Temporal variability of summer-time ozone and aerosols in the free troposphere over the eastern North Atlantic, Geophys. Res. Lett., 22, 2925-2928, 1995.

Ramachandran, S.: New directions: Mineral dust and ozone-Heterogeneous chemistry, Atmos. Environ., 106, 369-370, 2015.

Ridgwell, A. J.: Dust in the Earth system: the biogeochemical linking of land, air and sea, Philos. Trans. R. Soc. Lond., 360, 2905-2924, 2002.

Roberts, A. P., Rohling, E. J., Grant, K. M., Larrasoaña, J. C., and Liu, Q.: Atmospheric dust variability from Arabia and China over the last 500,000 years, Quat. Sci. Rev., 30, 3537-3541, 2011.

Rodríguez, S., Cuevas, E., Prospero, J., Alastuey, A., Querol, X., López-Solano, J., García, M., and Alonso-Pérez, S.: Modulation of Saharan dust export by the North African dipole, Atmos. Chem. Phys., 15, 7471-7486, 2015.

Rodrıguez, S., Querol, X., Alastuey, A., Kallos, G., and Kakaliagou, O.: Saharan dust contributions to PM10 and TSP levels in Southern and Eastern Spain, Atmos. Environ., 35, 2433-2447, 2001.

Ryder, C. L., Highwood, E. J., Rosenberg, P. D., Trembath, J., Brooke, J. K., Bart, M., Dean, A., Crosier, J., Dorsey, J., and Brindley, H.: Optical properties of Saharan dust aerosol and

contribution from the coarse mode as measured during the Fennec 2011 aircraft campaign, Atmos. Chem. Phys., 13, 303-325, 2013.

Schepanski, K.: Transport of mineral dust and its impact on climate, Geosciences, 8, 151, 2018.

Schepanski, K., Merkel, U., and Tegen, I.: Mineral dust: Meteorological controls and climate impacts, Past Global Changes Magazine-Dust, 22, 62-63, 2014.

Schlichting, H.: Boundary-layer theory, McGraw-Hill, 1968.

Schulz, M., Prospero, J. M., Baker, A. R., Dentener, F., Ickes, L., Liss, P. S., Mahowald, N. M., Nickovic, S., Garcia-Pando, C. P., and Rodríguez, S.: Atmospheric transport and deposition of mineral dust to the ocean: implications for research needs, Environ. Sci. Technol. , 46, 10390-10404, 2012.

Seinfeld, J. H. and Pandis, S. N.: Atmospheric chemistry and physics: from air pollution to climate change, John Wiley & Sons, Hoboken, 2006.

Seinfeld, J. H. and Pandis, S. N.: Atmospheric chemistry and physics: from air pollution to climate change, Wiley-Interscience, New York, 2012.

Shao, Y., Ishizuka, M., Mikami, M., and Leys, J.: Parameterization of size-resolved dust emission and validation with measurements, J Geophys Res Atmos, 116, 2011a.

Shao, Y., Wyrwoll, K.-H., Chappell, A., Huang, J., Lin, Z., McTainsh, G. H., Mikami, M., Tanaka, T. Y., Wang, X., and Yoon, S.: Dust cycle: An emerging core theme in Earth system science, Aeolian Res., 2, 181-204, 2011b.

Slinn, S. and Slinn, W.: Predictions for particle deposition on natural waters, Atmos. Environ., 14, 1013-1016, 1980.

Stuut, J.-B., Smalley, I., and O'Hara-Dhand, K.: Aeolian dust in Europe: African sources and European deposits, Quat. Int., 198, 234-245, 2009.

Sullivan, R., Guazzotti, S., Sodeman, D., and Prather, K.: Direct observations of the atmospheric processing of Asian mineral dust, Atmos. Chem. Phys., 7, 1213-1236, 2007.

Swap, R., Garstang, M., Greco, S., Talbot, R., and Kållberg, P.: Saharan dust in the Amazon Basin, Tellus B, 44, 133-149, 1992.

Tian, Z., Dietze, V., Sommer, F., Baum, A., Kaminski, U., Sauer, J., Maschowski, C., Stille, P., Cen, K., and Gieré, R.: Coarse-particle passive-sampler measurements and single-particle analysis by transmitted light microscopy at highly frequented motorways, Aerosol Air Qual Res., 17, 1939, 2017.

Vandenberg, J. J. and Knoerr, K. R.: Comparison of surrogate surface techniques for estimation of sulfate dry deposition, Atmos. Environ., 19, 627-635, 1985.

Vivanco, M. G., Bessagnet, B., Cuvelier, C., Theobald, M., Tsyro, S., Pirovano, G., Aulinger, A., Bieser, J., Calori, G., and Ciarelli, G.: Joint analysis of deposition fluxes and atmospheric concentrations of inorganic nitrogen and sulphur compounds predicted by six chemistry transport models in the frame of the EURODELTAIII project, Atmos. Environ., 151, 152-175, 2017.

Wagner, J. and Leith, D.: Passive aerosol sampler. Part I: Principle of operation, Aerosol Sci. Technol., 34, 186-192, 2001a.

Wagner, J. and Leith, D.: Passive aerosol sampler. Part II: Wind tunnel experiments, Aerosol Sci. Technol. , 34, 193-201, 2001b.

Wang, K., Zhang, Y., Nenes, A., and Fountoukis, C.: Implementation of dust emission and chemistry into the Community Multiscale Air Quality modeling system and initial application to an Asian dust storm episode, Atmos. Chem. Phys., 12, 10209-10237, 2012.

Waza, A., Schneiders, K., May, J., Rodríguez, S., Epple, B., and Kandler, K.: Field comparison of dry deposition samplers for collection of atmospheric mineral dust: results from single-particle characterization, Atmos. Meas. Tech. Discuss., 2019, 1-40, 2019.

Weinzierl, B., Petzold, A., Esselborn, M., Wirth, M., Rasp, K., Kandler, K., Schuetz, L., Koepke, P., and Fiebig, M.: Airborne measurements of dust layer properties, particle size distribution and mixing state of Saharan dust during SAMUM 2006, Tellus B Chem Phys Meteorol., 61, 96-117, 2009.

WMO: GAW Report, 202. Workshop on Modelling and Observing the Impacts of Dust Transport/Deposition on Marine Productivity (7-9 March 2011), Sliema, Malta, 2011.

Wood, N.: A simple method for the calculation of turbulent deposition to smooth and rough surfaces, J. Aerosol Sci., 12, 275-290, 1981.

Wu, Y.-L., Davidson, C. I., Dolske, D. A., and Sherwood, S. I.: Dry deposition of atmospheric contaminants: the relative importance of aerodynamic, boundary layer, and surface resistances, Aerosol Sci. Technol., 16, 65-81, 1992.

Yamamoto, N., Hikono, M., Koyama, H., Kumagai, K., Fujii, M., and Yanagisawa, Y.: A passive sampler for airborne coarse particles, J. Aerosol Sci, 37, 1442-1454, 2006.

Zhang, J.: A Study on Dust Dry Deposition: Wind-tunnel Experiment and Improved Parameterization, 2013. Universität zu Köln, 2013.

Zhang, J. and Shao, Y.: A new parameterization of particle dry deposition over rough surfaces, Atmos. Chem. Phys., 14, 12429-12440, 2014.

Zhang, J., Shao, Y., and Huang, N.: Measurements of dust deposition velocity in a wind-tunnel experiment, Atmos. Chem. Phys., 14, 8869-8882, 2014.

Appendix

Table A 1: A daily basis mass deposition rate (**mg/ (m^2d)**) shown in each size interval measured by **Vertical deposition samplers**. FP=Flat plate, Sig=Sigma-2

Samp. Id.	Date	Temp (℃)	Wind speed (m/s)	Mass deposition rate (mg/(m^2d)) Size interval (aerodynamic diameter)					
				1-2 µm	2-4 µm	4-8 µm	8-16 µm	16-32 µm	32-64 µm
FP	02.08.17	15.997	2.055	0.0125	0.0332	0.1591	0.6915	1.0487	0
FP	03.08.17	16.832	2.182	0.0178	0.085	0.4457	3.1786	3.5723	12.2381
FP	09.08.17	22.064	3.045	0.2318	2.5612	12.1382	22.3694	17.5472	0
FP	10.08.17	22.041	2.694	0.1268	1.7105	7.6181	14.3374	10.8418	7.2271
FP	20.08.17	23.049	2.321	0.0587	0.9965	7.7644	31.8469	39.2924	0
FP	21.08.17	22.127	1.991	0.0625	1.2487	9.9323	29.9751	22.0631	0
FP	22.08.17	21.126	3.011	0.0413	1.0977	8.4911	16.1487	9.563	0
FP	16.07.17	21.407	1.687	0.1512	1.6673	5.8333	10.3739	6.789	0
FP	18.07.17	19.863	3.289	0.0773	1.0835	4.3797	5.3431	4.4326	0
FP	19.07.17	17.691	4.275	0.0191	0.2874	1.4257	2.5807	0.7248	0
FP	20.07.17	15.915	4.620	0.0084	0.0437	0.3936	1.7336	2.0418	0
FP	24.07.17	20.758	3.883	0.1656	2.1236	8.9983	13.6345	2.7224	0
FP	25.07.17	20.784	2.055	0.1468	1.5641	6.7421	11.8483	0.7455	0
FP	26.07.17	20.989	2.550	0.0819	1.0551	5.0441	7.0303	1.8159	0
FP	27.07.17	21.563	2.092	0.1272	1.3325	6.6209	5.5919	0.8894	0
FP	28.07.17	22.325	2.318	0.0912	1.2328	4.7233	4.0095	1.9389	0
FP	29.07.17	21.971	4.438	0.0145	0.0798	0.5085	0.7329	1.9062	0
FP	30.07.17	19.823	4.874	0.08	0.2918	1.2003	1.9713	0	0
Sig	02.08.17	15.997	2.055	0.0133	0.0435	0.3232	1.4541	1.1561	0
Sig	03.08.17	16.832	2.182	0.0117	0.0637	0.2629	0.7752	0.7638	0
Sig	04.08.17	18.734	3.251	0.0537	0.2111	0.6742	0.9907	0.2664	0
Sig	09.08.17	22.064	3.045	0.2747	3.2314	12.3996	21.4241	7.4674	0
Sig	10.08.17	22.041	2.694	0.1171	1.312	4.7166	7.9581	1.4412	0
Sig	11.08.17	20.230	4.490	0.0506	0.3731	1.4438	3.2957	3.822	5.9832
Sig	12.08.17	18.666	4.551	0.0435	0.3212	1.0996	2.4052	2.1606	0
Sig	14.08.17	19.269	5.154	0.0929	0.6751	2.6105	5.3232	6.6811	0
Sig	15.08.17	19.918	1.855	0.0113	0.0581	0.2661	0.384	1.164	0
Sig	16.08.17	22.284	1.523	0.1003	0.973	3.507	5.4434	4.8978	0
Sig	17.08.17	21.384	2.978	0.1022	0.6704	2.382	4.9459	4.6931	0
Sig	18.08.17	20.574	3.080	0.0423	0.2089	0.7355	1.606	1.455	0
Sig	19.08.17	22.836	2.388	0.0337	0.2013	0.9165	2.0097	2.0509	0
Sig	20.08.17	23.049	2.321	0.2254	2.5137	12.8442	44.6417	42.0205	11.7559
Sig	21.08.17	22.127	1.991	0.3337	4.1199	20.8917	48.5994	36.6512	6.6514
Sig	22.08.17	21.126	3.011	0.2849	3.5102	16.3368	35.5797	17.1256	0
Sig	20.07.17	15.915	4.620	0.0102	0.0431	0.2539	1.8245	2.4863	0
Sig	21.07.17	14.153	3.830	0.0093	0.0405	0.1077	0.5439	0	0

Sig	26.07.17	20.989	2.550	0.1704	2.0074	8.3447	11.0216	3.496	0
Sig	27.07.17	21.563	2.092	0.1692	2.3802	10.0826	9.6501	4.2398	0
Sig	28.07.17	22.325	2.318	0.2126	2.3481	9.5403	10.2896	1.9448	0
Sig	29.07.17	21.971	4.438	0.1927	2.1052	8.1321	8.5173	1.0481	0
Sig	30.07.17	19.823	4.874	0.4671	1.2559	2.7535	4.3127	6.5318	0

Table A 2: A daily basis number deposition rate **(1/ (m²d))** shown in each interval measured by **Vertical deposition samplers**. FP=Flat plate, Sig=Sigma-2

Samp. Id.	**Date**	**Temp (ºC)**	**Wind speed (m/s)**	**Number deposition rate 1/(m²d)** Size interval (aerodynamic diameter)					
				1-2 µm	2-4 µm	4-8 µm	8-16 µm	16-32 µm	32-64 µm
FP	02.08.17	15.997	2.055	2.64E+06	9.95E+05	6.99E+05	2.69E+05	2.70E+05	0
FP	03.08.17	16.832	2.182	4.22E+06	2.39E+06	1.43E+06	1.14E+06	1.99E+05	8.50E+04
FP	09.08.17	22.064	3.045	4.12E+07	6.57E+07	4.39E+07	1.10E+07	8.10E+05	0
FP	10.08.17	22.041	2.694	2.17E+07	4.28E+07	2.70E+07	6.87E+06	6.30E+05	4.00E+04
FP	20.08.17	23.049	2.321	9.70E+06	2.33E+07	2.49E+07	1.20E+07	2.79E+06	0
FP	21.08.17	22.127	1.991	9.52E+06	2.87E+07	3.42E+07	1.35E+07	1.66E+06	0
FP	22.08.17	21.126	3.011	6.48E+06	2.43E+07	2.87E+07	7.87E+06	5.40E+05	0
FP	16.07.17	21.407	1.687	2.72E+07	4.26E+07	2.25E+07	5.69E+06	4.40E+05	0
FP	18.07.17	19.863	3.289	1.33E+07	2.74E+07	1.66E+07	3.02E+06	3.20E+05	0
FP	19.07.17	17.691	4.275	3.34E+06	6.59E+06	4.97E+06	1.32E+06	8.40E+04	0
FP	20.07.17	15.915	4.620	1.80E+06	1.34E+06	1.27E+06	6.96E+05	7.20E+04	0
FP	24.07.17	20.758	3.883	2.83E+07	5.16E+07	3.29E+07	7.71E+06	2.30E+05	0
FP	25.07.17	20.784	2.055	2.58E+07	4.07E+07	2.47E+07	6.18E+06	5.00E+04	0
FP	26.07.17	20.989	2.550	4.22E+06	1.59E+07	1.87E+07	5.13E+06	3.50E+05	0
FP	27.07.17	21.563	2.092	2.46E+07	3.40E+07	2.47E+07	3.59E+06	1.20E+05	0
FP	28.07.17	22.325	2.318	1.59E+07	3.19E+07	1.75E+07	2.43E+06	8.00E+04	0
FP	29.07.17	21.971	4.438	2.80E+06	2.08E+07	1.48E+06	4.25E+05	1.50E+05	0
FP	30.07.17	19.823	4.874	1.98E+07	7.50E+06	4.85E+06	9.70E+05	0	0
Sig	02.08.17	15.997	2.055	2.70E+06	1.32E+06	9.72E+05	5.13E+05	8.10E+04	0
Sig	03.08.17	16.832	2.182	2.55E+06	1.83E+06	9.93E+05	2.95E+05	5.40E+04	0
Sig	04.08.17	18.734	3.251	1.12E+07	6.50E+06	2.69E+06	4.80E+05	3.00E+04	0
Sig	09.08.17	22.064	3.045	4.64E+07	8.29E+07	4.79E+07	1.08E+07	5.80E+05	0
Sig	10.08.17	22.041	2.694	2.00E+07	3.34E+07	1.82E+07	4.23E+06	1.30E+05	0
Sig	11.08.17	20.230	4.490	9.72E+06	1.05E+07	5.75E+06	1.93E+06	3.30E+05	4.00E+04
Sig	12.08.17	18.666	4.551	8.52E+06	8.49E+06	3.71E+06	1.13E+06	1.33E+05	0
Sig	14.08.17	19.269	5.154	1.82E+07	1.77E+07	1.01E+07	2.65E+06	3.50E+05	0
Sig	15.08.17	19.918	1.855	2.07E+06	1.56E+06	9.83E+05	2.18E+05	5.50E+04	0
Sig	16.08.17	22.284	1.523	1.83E+07	2.45E+07	1.33E+07	2.77E+06	2.30E+05	0
Sig	17.08.17	21.384	2.978	2.10E+07	1.85E+07	8.83E+06	2.45E+06	3.60E+05	0
Sig	18.08.17	20.574	3.080	9.04E+06	5.60E+06	2.85E+06	7.56E+05	1.03E+05	0
Sig	19.08.17	22.836	2.388	6.42E+06	5.32E+06	3.42E+06	9.50E+05	1.52E+05	0
Sig	20.08.17	23.049	2.321	3.69E+07	6.64E+07	4.57E+07	1.98E+07	2.63E+06	6.00E+04
Sig	21.08.17	22.127	1.991	5.52E+07	1.04E+08	7.10E+07	2.22E+07	2.50E+06	1.00E+05

Sig	22.08.17	21.126	3.011	4.74E+07	8.96E+07	5.80E+07	1.73E+07	1.45E+06	0
Sig	20.07.17	15.915	4.620	2.11E+06	1.15E+06	7.38E+05	7.12E+05	1.27E+05	0
Sig	21.07.17	14.153	3.830	2.12E+06	1.25E+06	4.24E+05	2.74E+05	0	0
Sig	26.07.17	20.989	2.550	3.05E+07	5.15E+07	3.06E+07	6.54E+06	3.10E+05	0
Sig	27.07.17	21.563	2.092	2.95E+07	5.97E+07	3.74E+07	5.75E+06	4.30E+05	0
Sig	28.07.17	22.325	2.318	3.58E+07	6.28E+07	3.54E+07	5.81E+06	2.00E+05	0
Sig	29.07.17	21.971	4.438	3.20E+07	5.78E+07	3.10E+07	4.68E+06	1.00E+05	0
Sig	30.07.17	19.823	4.874	1.04E+08	4.09E+07	9.80E+06	2.10E+06	3.00E+05	0

Table A 3: A daily basis mass deposition rate (**mg/ (m^2d)**) shown in each interval measured by **Horizontal deposition samplers**. Mass deposition rate in each size interval is also shown. MW=MWAC, BS=BSNE

Samp. Id.	**Date**	**Temp. (ºC)**	**Wind Speed (m/s)**	**Mass deposition rate (mg/(m^2d))** Size interval (aerodynamic diameter)					
				1-2 µm	2-4 µm	4-8 µm	8-16 µm	16-32 µm	32-64 µm
MW	02.08.17	15.997	2.055	0.053	0.3195	3.5756	18.9069	12.3191	0
MW	04.08.17	18.734	3.251	0.0308	0.1555	0.7479	0.9514	2.5171	0
MW	08.08.17	22.889	4.303	0.573	4.788	63.067	431.618	596.928	18.604
MW	09.08.17	22.064	3.045	0.3805	3.7223	53.2968	357.1174	276.0571	12.5649
MW	10.08.17	22.041	2.694	0.2763	3.1587	29.7283	207.9945	321.5826	53.2269
MW	12.08.17	18.666	4.551	1.1247	6.0944	49.9189	246.8832	180.6267	0
MW	14.08.17	19.269	5.154	3.1606	10.8308	87.7027	518.3101	513.3998	110.1782
MW	15.08.17	19.918	1.855	0.1272	0.742	5.9049	33.331	84.2202	0
MW	17.08.17	21.384	2.978	0.0619	0.5264	4.8274	36.7475	36.8723	26.7913
MW	18.08.17	20.574	3.080	0.1162	0.6434	4.26	21.1639	29.4541	47.5157
MW	19.08.17	22.836	2.388	0.059	0.4633	4.7649	21.8155	29.468	6.373
MW	21.08.17	22.127	1.991	0.2617	3.1625	17.5533	33.4467	24.5892	6.2844
MW	22.08.17	21.126	3.011	0.2238	2.7402	39.8506	288.9442	225.7404	24.2119
MW	20.07.17	15.915	4.620	0.1951	1.2363	12.9435	50.1497	120.0182	51.0725
MW	21.07.17	14.153	3.830	0.0234	0.1781	1.9931	7.0882	8.4802	2.4772
MW	22.07.17	15.603	2.559	0.0059	0.0165	0.0728	0.2085	0.3042	0
MW	23.07.17	17.732	4.427	0.0219	0.1316	1.4648	7.4614	6.4594	12.1317
MW	26.07.17	20.989	2.550	0.1499	1.7981	9.1141	11.8906	1.866	0
MW	27.07.17	21.563	2.092	0.1436	2.5401	16.6638	30.1571	9.0439	0
MW	28.07.17	22.325	2.318	0.1674	2.6065	12.0603	35.6525	24.0122	0
MW	29.07.17	21.971	4.438	0.2055	2.4908	42.7172	163.4428	109.8901	0
MW	30.07.17	19.823	4.874	0.0576	0.4659	2.2444	5.989	7.0296	0
BS	03.08.17	16.832	2.182	0.0137	0.077	0.3143	0.7407	3.8354	0
BS	04.08.17	18.734	3.251	0.0193	0.1162	0.5597	1.6363	1.2249	0
BS	05.08.17	21.383	5.379	0.0506	0.6417	3.5234	8.293	9.3819	3.3068
BS	06.08.17	22.347	6.790	0.3858	5.0476	45.0073	159.0974	75.0699	26.4677
BS	07.08.17	22.706	4.842	0.6379	9.1193	51.2209	130.3214	80.8477	0
BS	08.08.17	22.889	4.303	0.7554	6.9688	36.7909	125.2447	88.1866	0
BS	09.08.17	22.064	3.045	0.3203	3.0439	13.5882	33.253	16.5779	21.672

BS	10.08.17	22.041	2.694	0.194	2.0181	8.6547	17.7228	10.3509	0
BS	12.08.17	18.666	4.551	0.037	0.3435	2.2437	8.2023	6.6773	4.2183
BS	14.08.17	19.269	5.154	0.1175	0.9683	7.6959	32.4113	37.7385	3.5343
BS	16.08.17	22.284	1.523	0.0036	0.0253	0.1168	0	0	0
BS	18.08.17	20.574	3.080	0.0403	0.2139	1.0044	3.4598	2.1027	0
BS	20.08.17	23.049	2.321	0.2178	2.2909	13.381	48.7953	48.1988	0
BS	21.08.17	23.049	1.991	0.3135	4.0807	21.3125	59.5899	52.2078	121.0427
BS	24.07.17	20.758	3.883	0.2912	3.0925	14.4286	33.4588	28.8779	0
BS	25.07.17	20.784	2.055	0.3448	2.9782	23.8669	15.4882	2.9016	0
BS	26.07.17	20.989	2.550	0.1655	1.8011	7.0431	15.266	3.2846	0
BS	27.07.17	21.563	2.092	0.2367	2.3747	9.1715	14.3749	2.402	0
BS	28.07.17	22.325	2.318	0.2228	2.2278	8.9356	9.8436	1.0245	0
BS	29.07.17	21.971	4.438	0.1944	2.3734	11.0921	20.7425	10.5312	4.1926
BS	30.07.17	19.823	4.874	0.0469	0.5442	2.8858	9.4036	5.3719	0

Table A 4: A daily basis number deposition rate **(1/ (m²d)**) shown in each interval measured by **Horizontal deposition samplers**. MW=MWAC, BS=BSNE.

Samp. Id.	**Date**	**Temp. (ºC)**	**Wind Speed (m/s)**	**Number deposition rate 1/(m²d)** Size interval (aerodynamic diameter)					
				1-2 µm	2-4 µm	4-8 µm	8-16 µm	16-32 µm	32-64 µm
MW	02.08.17	15.997	2.055	1.10E+07	9.09E+06	1.02E+07	7.47E+06	7.70E+05	0
MW	04.08.17	18.734	3.251	7.12E+06	4.26E+06	2.35E+06	4.20E+05	8.40E+04	0
MW	08.08.17	22.889	4.303	1.06E+08	1.29E+08	1.71E+08	1.86E+08	3.41E+07	2.00E+05
MW	09.08.17	22.064	3.045	7.20E+07	9.20E+07	1.40E+08	1.49E+08	1.66E+07	1.00E+05
MW	10.08.17	22.041	2.694	4.75E+07	8.06E+07	8.56E+07	8.75E+07	2.04E+07	4.80E+05
MW	12.08.17	18.666	4.551	2.21E+08	1.76E+08	1.47E+08	1.07E+08	1.42E+07	0
MW	14.08.17	19.269	5.154	6.09E+08	3.49E+08	2.46E+08	2.21E+08	3.26E+07	1.20E+06
MW	15.08.17	19.918	1.855	2.57E+07	2.04E+07	1.67E+07	1.33E+07	4.02E+06	0
MW	17.08.17	21.384	2.978	1.10E+07	1.33E+07	1.41E+07	1.58E+07	2.08E+06	9.00E+04
MW	18.08.17	20.574	3.080	2.22E+07	1.83E+07	1.27E+07	9.05E+06	1.76E+06	2.30E+05
MW	19.08.17	22.836	2.388	1.08E+07	1.12E+07	1.36E+07	1.00E+07	1.82E+06	8.00E+04
MW	21.08.17	22.127	1.991	4.54E+07	7.94E+07	6.27E+07	1.72E+07	1.32E+06	7.00E+04
MW	22.08.17	21.126	3.011	4.07E+07	6.93E+07	1.07E+08	1.24E+08	1.49E+07	1.00E+05
MW	20.07.17	15.915	4.620	3.67E+07	3.23E+07	3.71E+07	2.25E+07	5.07E+06	2.90E+05
MW	21.07.17	14.153	3.830	2.73E+07	2.67E+07	3.21E+07	1.68E+07	2.74E+06	1.50E+05
MW	22.07.17	15.603	2.559	1.33E+06	4.42E+05	1.63E+05	9.30E+04	2.30E+04	0
MW	23.07.17	17.732	4.427	4.31E+06	3.82E+06	3.87E+06	3.55E+06	4.33E+05	2.70E+04
MW	26.07.17	20.989	2.550	2.66E+07	4.53E+07	3.34E+07	6.39E+06	1.80E+05	0
MW	27.07.17	21.563	2.092	2.50E+07	6.16E+07	5.73E+07	1.62E+07	5.60E+05	0
MW	28.07.17	22.325	2.318	2.81E+07	6.41E+07	4.25E+07	1.51E+07	1.82E+06	0
MW	29.07.17	21.971	4.438	3.80E+07	5.98E+07	1.13E+08	8.17E+07	7.80E+06	0
MW	30.07.17	19.823	4.874	1.20E+07	1.23E+07	8.23E+06	2.59E+06	3.50E+05	0
BS	03.08.17	16.832	2.182	2.67E+06	2.17E+06	1.09E+06	3.29E+05	9.90E+04	0

BS	04.08.17	18.734	3.251	4.43E+06	3.20E+06	1.92E+06	6.94E+05	9.90E+04	0
BS	05.08.17	21.383	5.379	9.16E+06	1.64E+07	1.20E+07	4.15E+06	4.90E+05	4.00E+04
BS	06.08.17	22.347	6.790	6.61E+06	1.27E+07	1.39E+07	7.15E+06	6.30E+05	3.00E+04
BS	07.08.17	22.706	4.842	1.06E+08	2.32E+08	1.72E+08	5.82E+07	6.40E+06	0
BS	08.08.17	22.889	4.303	1.44E+08	1.79E+08	1.29E+08	5.15E+07	7.70E+06	0
BS	09.08.17	22.064	3.045	5.65E+07	7.88E+07	5.07E+07	1.62E+07	1.01E+06	2.00E+05
BS	10.08.17	22.041	2.694	3.35E+07	5.33E+07	3.11E+07	9.35E+06	8.30E+05	0
BS	12.08.17	18.666	4.551	7.11E+06	8.52E+06	6.52E+06	3.50E+06	5.08E+05	2.80E+04
BS	14.08.17	19.269	5.154	2.45E+07	2.59E+07	2.36E+07	1.39E+07	2.10E+06	4.00E+04
BS	16.08.17	22.284	1.523	6.98E+05	7.62E+05	4.44E+05	0	0	0
BS	18.08.17	20.574	3.080	8.63E+06	6.30E+06	3.38E+06	1.63E+06	2.08E+05	0
BS	20.08.17	23.049	2.321	3.65E+07	6.08E+07	4.45E+07	2.19E+07	3.23E+06	0
BS	21.08.17	23.049	1.991	5.14E+07	1.01E+08	7.45E+07	2.65E+07	3.30E+06	2.00E+05
BS	24.07.17	20.758	3.883	5.28E+07	7.98E+07	4.97E+07	1.60E+07	1.96E+06	0
BS	25.07.17	20.784	2.055	6.03E+07	7.79E+07	3.61E+07	8.75E+06	2.40E+05	0
BS	26.07.17	20.989	2.550	2.95E+07	4.74E+07	2.66E+07	7.58E+06	2.90E+05	0
BS	27.07.17	21.563	2.092	4.11E+07	6.26E+07	3.46E+07	7.21E+06	2.00E+05	0
BS	28.07.17	22.325	2.318	3.95E+07	5.91E+07	3.33E+07	5.38E+06	1.00E+05	0
BS	29.07.17	21.971	4.438	3.27E+07	6.05E+07	3.87E+07	1.03E+07	7.50E+05	5.00E+04
BS	30.07.17	19.823	4.874	8.72E+06	1.35E+07	1.00E+07	4.23E+06	4.70E+05	0

Table A 5: A daily basis upward and downward mass deposition rate (**mg/ (m^2d)**) shown in each interval measured by Flat plate sampler (25mm) specified in size intervals (µm). FP_U=Upward deposition rate, FP_D=Downward deposition rate.

Samp. Id.	**Date**	**Temp. (ºC)**	**Wind speed (m/s)**	**Mass deposition rate (mg/(m^2d))** Size interval (aerodynamic diameter)					
				1-2 µm	2-4 µm	4-8 µm	8-16 µm	16-32 µm	32-64 µm
FP_U	20.07.17	15.915	4.620	0.006	0.0126	0.0071	0.1607	0	0
FP_U	21.07.17	14.153	3.830	0.0085	0.0128	0.1135	0.2452	0	0
FP_U	24.07.17	20.758	3.883	0.0129	0.0456	0.2431	0.5339	0	0
FP_U	25.07.17	20.784	2.055	0.0251	0.0397	0.2362	0	0	0
FP_U	26.07.17	20.989	2.550	0.0104	0.0803	0.1911	0.0924	0	0
FP_U	27.07.17	21.563	2.092	0.0065	0.0223	0.0759	0.2792	0.6606	0
FP_U	28.07.17	22.325	2.318	0.0225	0.0375	0.1186	0.0279	0	0
FP_U	29.07.17	21.971	4.438	0.021	0.0444	0.1147	0.2817	0.2653	0
FP_D	20.07.17	15.915	4.620	0.0153	0.0578	0.2786	0.8438	0.2835	0
FP_D	21.07.17	14.153	3.830	0.0357	0.1865	1.0712	3.7204	2.787	0
FP_D	24.07.17	20.758	3.883	0.227	2.7686	7.7674	5.2542	7.7463	0
FP_D	25.07.17	20.784	2.055	0.2505	2.414	8.6004	9.5165	4.7043	0
FP_D	26.07.17	20.989	2.550	0.1151	1.4906	5.555	6.5666	3.226	0
FP_D	27.07.17	21.563	2.092	0.1608	2.1048	8.2862	10.0201	2.0881	0
FP_D	28.07.17	22.325	2.318	0.1585	1.8237	7.0338	7.517	1.2685	0
FP_D	29.07.17	21.971	4.438	0.154	2.0606	9.0657	8.783	2.9589	0

Table A 6: A daily basis upward and downward number deposition rate (**1/ (m^2d)** shown in each interval measured by Flat plate sampler (25mm). FP_U=Upward deposition rate, FP_D=Downward deposition rate.

Samp. Id.	Date	Temp (ºC)	Wind speed (m/s)	Number deposition rate, 1/(m^2d) Size interval (aerodynamic diameter)					
				1-2 µm	2-4 µm	4-8 µm	8-16 µm	16-32 µm	32-64 µm
FP_U	20.07.17	15.915	4.620	1.70E+06	4.60E+05	3.50E+04	7.10E+04	0	0
FP_U	21.07.17	14.153	3.830	1.86E+06	5.32E+05	3.63E+05	1.21E+05	0	0
FP_U	24.07.17	20.758	3.883	2.68E+06	1.28E+06	8.35E+05	3.44E+05	0	0
FP_U	25.07.17	20.784	2.055	4.99E+06	1.28E+06	9.14E+05	0	0	0
FP_U	26.07.17	20.989	2.550	2.33E+06	2.15E+06	7.46E+05	6.80E+04	0	0
FP_U	27.07.17	21.563	2.092	1.40E+06	6.74E+05	2.89E+05	9.60E+04	2.40E+04	0
FP_U	28.07.17	22.325	2.318	4.84E+06	1.20E+06	5.19E+05	2.70E+04	0	0
FP_U	29.07.17	21.971	4.438	4.84E+06	1.20E+06	5.19E+05	2.70E+04	0	0
FP_D	20.07.17	15.915	4.620	3.81E+06	1.82E+06	9.61E+05	3.64E+05	3.30E+04	0
FP_D	21.07.17	14.153	3.830	7.68E+06	6.33E+06	3.75E+06	1.84E+06	1.94E+05	0
FP_D	24.07.17	20.758	3.883	3.90E+07	7.12E+07	3.37E+07	3.25E+06	6.20E+05	0
FP_D	25.07.17	20.784	2.055	4.43E+07	6.54E+07	3.30E+07	5.41E+06	2.70E+05	0
FP_D	26.07.17	20.989	2.550	2.03E+07	3.77E+07	2.11E+07	3.41E+06	2.80E+05	0
FP_D	27.07.17	21.563	2.092	2.61E+07	5.22E+07	3.10E+07	5.26E+06	2.10E+05	0
FP_D	28.07.17	22.325	2.318	2.75E+07	4.70E+07	2.61E+07	4.41E+06	1.30E+05	0
FP_D	29.07.17	21.971	4.438	2.59E+07	5.27E+07	3.50E+07	4.81E+06	2.40E+05	0

Table A 7: Defintion of particle class

	Group name	Classification criteria	Class
1	Fe-rich [Fe-rich]	Fe/ (F+Na+Mg+Al+Si+P+S+Cl+K+Ca+Ti+Cr+Mn+Fe) =0.5... 1.01,Cr/ (Cr+Fe) =0... 0.1 And Cl/ (Cl+Fe) =0... 0.1	Oxides/Hydroxides
2	Mg-rich [Mg-rich]	Mg/(F+Na+Mg+Al+Si+P+S+Cl+K+Ca+Ti+Cr+Mn+Fe)=0.7 .. 1.01	Others
3	Ti-rich [Ti-rich]	Ti/ (F+Na+Mg+Al+Si+P+S+Cl+K+Ca+Ti+Cr+Mn+Fe) =0.7... 1.01,Ca/ (Ca+Ti) =0... 0.3	Oxides/Hydroxides
4	Ti-rich [Ti-Ca-rich]	(Ti+Ca)/(F+Na+Mg+Al+Si+P+S+Cl+K+Ca+Ti+Cr+Mn+Fe)=0.7...1 .01, Ca/ (Ca+Ti) =0.3... 0.7	Oxides/Hydroxides
5	FeTi-rich [Ilmenit]	(Fe+Ti)/(F+Na+Mg+Al+Si+P+S+Cl+K+Ca+Ti+Cr+Mn+Fe)=0.7...1 .01, Ti/Fe=0.25... 4	Oxides/Hydroxides
6	Quartz [Quartz]	Si/(F+Na+Mg+Al+Si+P+S+Cl+K+Ca+Ti+Cr+Mn+Fe)=0.7...1.01, (Na+Mg+K+Ca+Al)/Si=0... 0.2	Silicates
7	K-rich silicate [K-Feldspar]	(K+Al+Si)/ (F+Na+Mg+Al+Si+P+S+Cl+K+Ca+Ti+Cr+Mn+Fe)=0.7...1.01, Al/Si=0.1... 0.5 , K/Si=0.1... 0.5 , Ca/Si=0... 0.1, Na/Si=0... 0.1	Silicates
8	Na-rich silicate [Na-Feldspar]	(Na+Al+Si)/(F+Na+Mg+Al+Si+P+S+Cl+K+Ca+Ti+Cr+Mn+Fe)=0. 7...1.01, Al/Si=0.1... 0.5, Na/Si=0.1... 0.5, Ca/Si=0... 0.1, K/Si=0... 0.1, (Cl+2*S)/Na = 0... 0.3, (Cl+2*S) / (Al+Si) =0... 0.125	Silicates
9	Al-rich silicate [Kaolinite]	(Al+Si)/ (F+Na+Mg+Al+Si+P+S+Cl+K+Ca+Ti+Cr+Mn+Fe)=0.7... 1.01, Al/Si=0.5... 1.5, Fe/ (Al+Si) =0... 0.2, Mg/ (Al+Si) =0... 0.2, Ca/ (Al+Si) =0... 0.2, (Na+Cl+2*S)/ (Al+Si) =0... 0.25	Silicates
10	MgAl-rich silicate [Mg-Clay]	(Mg+Al+Si)/(F+Na+Mg+Al+Si+P+S+Cl+K+Ca+Ti+Cr+Mn+Fe)=0. 7...1.01, Al/Si=0.5... 1.5, Fe/ (Al+Si) =0... 0.2, Mg/ (Al+Si) =0.2... 1.01, (Na+Cl+2*S) / (Al+Si) =0... 0.25	Silicates
11	Fe(Mg)Al-rich silicate [Fe-Clay]	(Mg+Fe+Al+Si)/(F+Na+Mg+Al+Si+P+S+Cl+K+Ca+Ti+Cr+Mn+Fe) =0.7... 1.01, Al/Si=0.5... 1.5, Fe/ (Al+Si) =0.2... 1.01, (Na+Cl+2*S) / (Al+Si) =0... 0.25	Silicates
12	Ca-rich silicate/Ca-Si-mixture[Ca-rich silicate]	(Ca+Al+Si)/(F+Na+Mg+Al+Si+P+S+Cl+K+Ca+Ti+Cr+Mn+Fe)=0. 7... 1.01, Ca/ (Al+Si) =0.3... 3, (Na+Cl+2*S) / (Al+Si) =0... 0.25	Silicates
13	Complex silicate (low Al) [complex feldspar]	(Al+Si+Na+Mg+K+Ca+Fe)/ (F+Na+Mg+Al+Si+P+S+Cl+K+Ca+Ti+Cr+Mn+Fe)=0.7 .. 1.01, Al/Si=0.05 .. 0.5, (Na+K+Ca)/Si=0.1 .. 1, Fe/Si=0 .. 0.5, Ca/Si=0 .. 0.5, K/Si=0.. .5, Mg/Si=0 .. 0.5, K/Si=0..0.5, (Na+Cl+2*S)/(Al+Si)=0..0.25	Silicates
14	complex silicate (high Al) [complex clay]	(Al+Si+Na+Mg+K+Ca+Fe) / (F+Na+Mg+Al+Si+P+S+Cl+K+Ca+Ti+Cr+Mn+Fe)=0.7 .. 1.01, Al/Si=0.5..1.5, (Mg+Fe+K)/Si=0.1 .. 1, Fe/Si=0 .. 0.5, Ca/Si=0 .. 0.5, K/Si=0..0.5, Mg/Si=0..0.5, K/Si=0..0.5, (Na+Cl+2*S)/(Al+Si)=0.. 0.25	Silicates
15	Ca-rich [Calcite]	Ca/(F+Na+Mg+Al+Si+P+S+Cl+K+Ca+Ti+Cr+Mn+Fe)=0.7 .. 1.01, (Al+Si)/Ca=0 .. 0.3, Mg/Ca=0 .. 0.3, S/Ca=0 .. 0.3, Cl/Ca=0 .. 0.3	Ca-rich
16	CaMg-rich [Dolomite]	(Mg+Ca) / (F+Na+Mg+Al+Si+P+S+Cl+K+Ca+Ti+Cr+Mn+Fe)=0.7 .. 1.01, Mg/Ca=0.3 .. 3, S/Ca=0 .. 0.3, Cl/Ca=0 .. 0.3, (Al+Si)/Ca=0 .. 0.3	Ca-rich
17	CaP-rich [Apatite]	(Ca+P) / (F+Na+Mg+Al+Si+P+S+Cl+K+Ca+Ti+Cr+Mn+Fe)=0.7 .. 1.01, Mg/Ca=0 .. 0.3, P/(Ca+P)=0.2 .. 0.8, Cl/Ca=0 .. 0.3, (Al+Si)/(P+Ca)=0 .. 0.25	Ca-rich
18	CaS-rich [Gypsum]	(Ca+S) / (F+Na+Mg+Al+Si+P+S+Cl+K+Ca+Ti+Cr+Mn+Fe)=0.7 .. 1.01, Ca/(Ca+S)=0.2 .. 0.8, Mg/Ca=0 .. 0.3, Cl/Ca=0 .. 0.3	stable sulfates
19	AlKS-rich [Alunite]	(Al+K+S) / (F+Na+Mg+Al+Si+P+S+Cl+K+Ca+Ti+Cr+Mn+Fe)=0.7 .. 1.01, Ca/(Ca+Al+K+S)=0..0.05, Si/(Si+Al+K+S)=0.. .1, K/(Al+K+S)=0.05..0.3 ,S/(Al+K+S)=0.15 .. 0.5, Al/(Al+K+S)=0.3..0.8	stable sulfates

20	NaCl-rich [Sea-salt]	(Na+Mg+Cl)/(F+Na+Mg+Al+Si+P+S+Cl+K+Ca+Ti+Cr+Mn+Fe)=0.7..1.01, Cl/(Na+0.5*Mg)=0.5 .. 2, Cl / (Cl+S)=0.7 .. 1.01, S/(Na+0.5*Mg)=0 .. 0.2, K/Na=0 .. 0.5, Ca/Na=0 .. 0.5, Mg/Na=0 .. 0.5, (Al+Si) / (Na+Cl+S)=0 .. 0.25	sea-salt
21	NaClS-rich [aged Sea salt]	(Na+Mg+Cl+S+Ca) / (F+Na+Mg+Al+Si+P+S+Cl+K+Ca+Ti+Cr+Mn+Fe)=0.7 .. 1.01, Cl/(Na+0.5*Mg)=0.2 .. 0.8, S/(Na+0.5*Mg)=0.2 .. 0.8, (Cl+2*S) / (Na+0.5*Mg+0.5*Ca)=0.3 .. 3.333, Cl / (Cl+S)=0.3 .. 0.7, K / (K+Na)=0 .. 0.3, Ca / (Ca+Na)=0 .. 0.2, Mg / (Mg+Na)=0 .. 0.3, (Al+Si) / (Al+Si+Na+Cl+S)=0 .. 0.25	sea-salt
22	NaS-rich [Na Sulfate]	(Na+Mg+S+Cl)/(F+Na+Mg+Al+Si+P+S+Cl+K+Ca+Ti+Cr+Mn+Fe)=0.7 .. 1.01, S/(Na+0.5*Mg)=0.8 .. 2, Cl/(Na+0.5*Mg)=0 .. 0.2, Cl / (Cl+S)=0 .. 0.3, K/Na=0 .. 0.5, Ca/Na=0 .. 0.5, Mg/Na=0 .. 0.5, (Al+Si)/(Na+Cl+S)=0 .. 0.25	soluble sulfates
23	S-rich [sulfate]	S/(F+Na+Mg+Al+Si+P+S+Cl+K+Ca+Ti+Cr+Mn+Fe)=0.7 .. 1.01, Cl / (Cl+S)=0 .. 0.3, Na/S=0 .. 1.01, Cl/S=0 .. 0.2, Si/S=0 .. 0.5, (Al+Si)/S=0 .. 0.25	Sulfates
24	complex sulfate [complex sulfate]	(Na+Mg+K+Ca+S+Cl)/ (F+Na+Mg+Al+Si+P+S+Cl+K+Ca+Ti+Cr+Mn+Fe)=0.7 .. 1.01, (Al+Si)/S=0 .. 0.25, Cl / (Cl+S)=0 .. 0.3	soluble sulfates
25	complex soluble salt [complex sulfate-chloride]	(Na+Mg+K+Ca+S+Cl)/ (F+Na+Mg+Al+Si+P+S+Cl+K+Ca+Ti+Cr+Mn+Fe)=0.7 .. 1.01, (Al+Si)/S=0 .. 0.25	soluble sulfates
26	NaCl/Si mixture [NaCl-Si-Mix]	(Al+Si+Mg+Fe+Na+Cl+S)/ (F+Na+Mg+Al+Si+P+S+Cl+K+Ca+Ti+Cr+Mn+Fe)=0.7 .. 1.01, Fe / (F+Na+Mg+Al+Si+P+S+Cl+K+Ca+Ti+Cr+Mn+Fe)=0 .. 0.3, (Na+Cl+2*S) / (Al+Si)=0.25 .. 4, S/Cl=0 .. 0.5	sea-salt/silicate mixtures
27	NaS/Si mixture [NaS-Si-Mix]	(Al+Si+Mg+Fe+Na+Cl+S)/ (F+Na+Mg+Al+Si+P+S+Cl+K+Ca+Ti+Cr+Mn+Fe)=0.7 .. 1.01, Fe / (F+Na+Mg+Al+Si+P+S+Cl+K+Ca+Ti+Cr+Mn+Fe)=0 .. 0.3, (Na+Cl+2*S) / (Al+Si)=0.25 .. 4, S/Cl=0 .. 0.5, (Na+Cl+2*S) / (Al+Si)=0.25.. 4, (K+Ca+Fe)/(Si+Al)=0 .. 0.7, Cl/S=0 ..1, S/Na=0.. 0.5	sulfate/silicate mixtures
28	NaClS/Si mixture [NaClS-Si-Mix]	(Al+Si+Mg+Fe+Na+Cl+S)/ (F+Na+Mg+Al+Si+P+S+Cl+K+Ca+Ti+Cr+Mn+Fe)=0.7 .. 1.01, (Na+Cl+2*S) / (Al+Si)=0.25 .. 4, Fe / (F+Na+Mg+Al+Si+P+S+Cl+K+Ca+Ti+Cr+Mn+Fe)=0.. .3,S/Cl=0.5..1	sea-salt/silicate mixtures
29	S/Si mixture [S-Si-Mix]	(Al+Si+Mg+Fe+Na+S)/ (F+Na+Mg+Al+Si+P+S+Cl+K+Ca+Ti+Cr+Mn+Fe)=0.7 .. 1.01, Fe / (F+Na+Mg+Al+Si+P+S+Cl+K+Ca+Ti+Cr+Mn+Fe)=0 .. 0.3, Si / (Al+Si+Mg+Fe) = 0.2..1.01, S/(Al+Si)=0.25 .. 4, Cl/S=0..1, Na/S=0.. 1	sulfate/silicate mixtures
30	other silicate [other silicate]	(Al+Si+Na+Mg+K+Ca+Fe+Ti)/ (F+Na+Mg+Al+Si+P+S+Cl+K+Ca+Ti+Cr+Mn+Fe)=0.7 .. 1.01, (Na+Cl+S) / (Al+Si+Fe)=0 .. 0.25	silicates
31	complex mixture [complex mix]	(Na+Mg+Al+Si+S+Cl+K+Ca+Fe)/ (F+Na+Mg+Al+Si+P+S+Cl+K+Ca+Ti+Cr+Mn+Fe)=0.7 .. 1.01, (Na+Cl) / (F+Na+Mg+Al+Si+P+S+Cl+K+Ca+Ti+Cr+Mn+Fe)=0.1 .. 0.9, S/(F+Na+Mg+Al+Si+P+S+Cl+K+Ca+Ti+Cr+Mn+Fe)=0.1 .. 0.9,(Ca+K+Mg+Fe)/ (F+Na+Mg+Al+Si+P+S+Cl+K+Ca+Ti+Cr+Mn+Fe)=0.1 .. 0.9, (Al+Si)/(F+Na+Mg+Al+Si+P+S+Cl+K+Ca+Ti+Cr+Mn+Fe)=0.1.. 0.9	complex mixtures

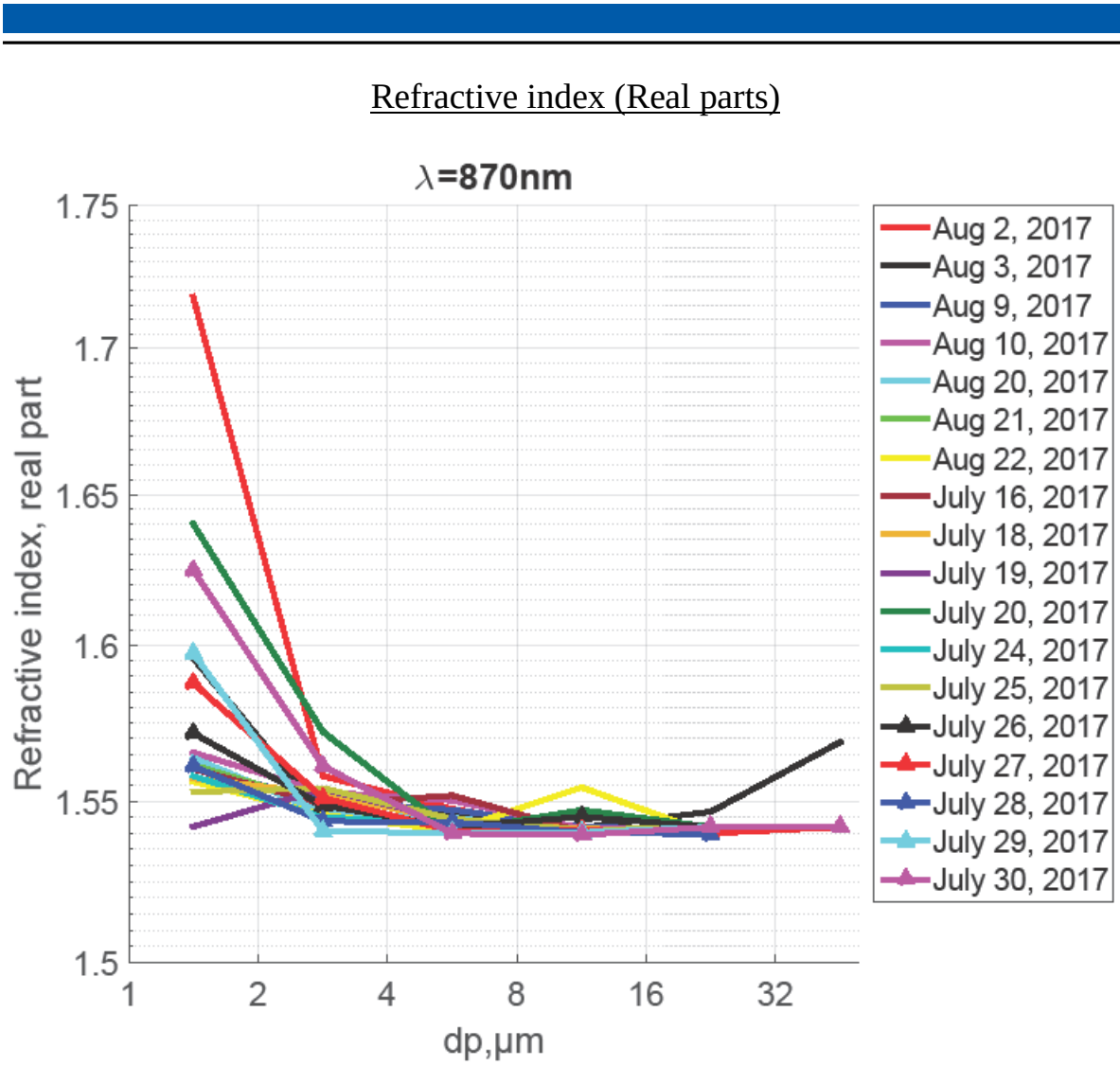

Figure A 1: Average complex refractive index (real part) analyzed over different days (at wavelength=870 nm).

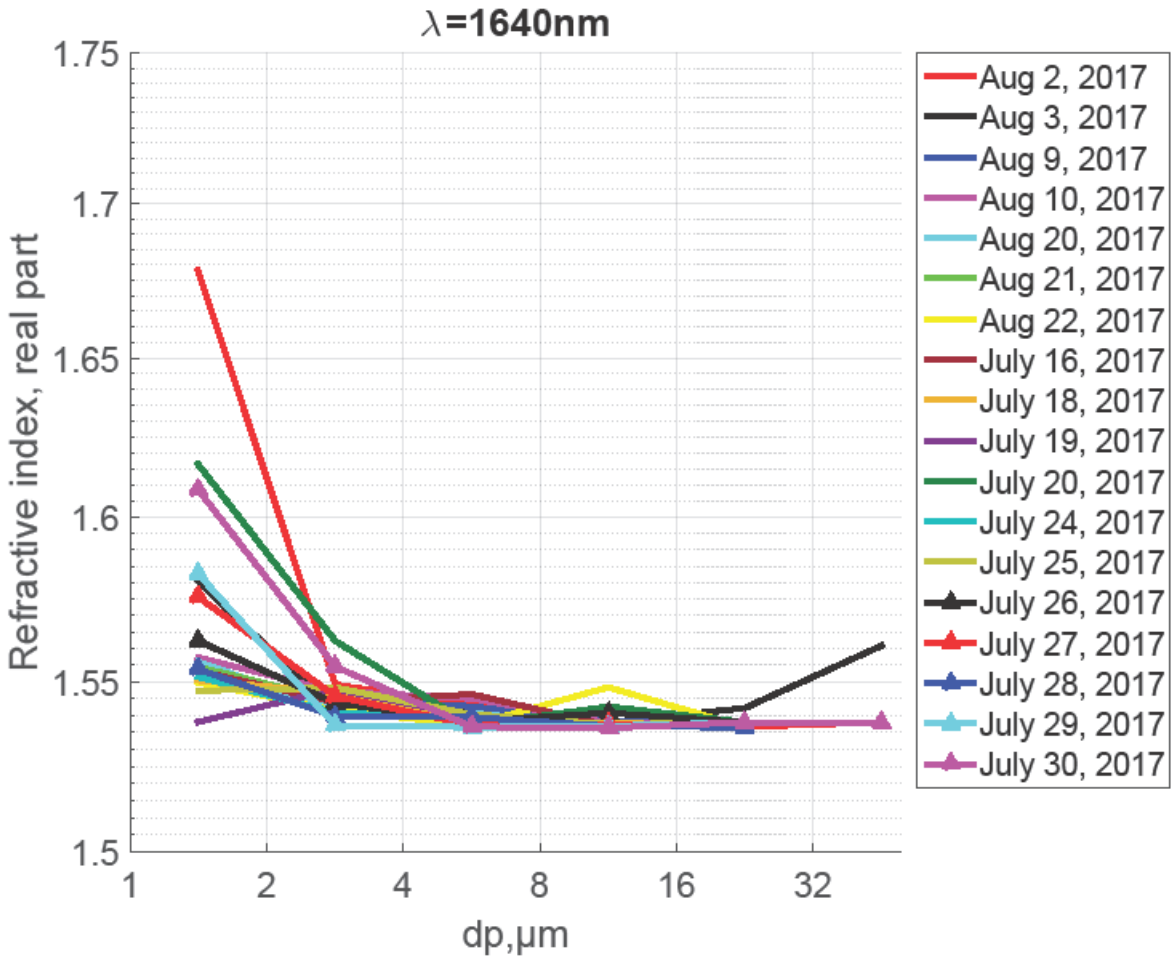

Figure A 2: Average complex refractive index (real part) analyzed over different days (at wavelength=1640 nm).

Refractive index (Imaginary parts)

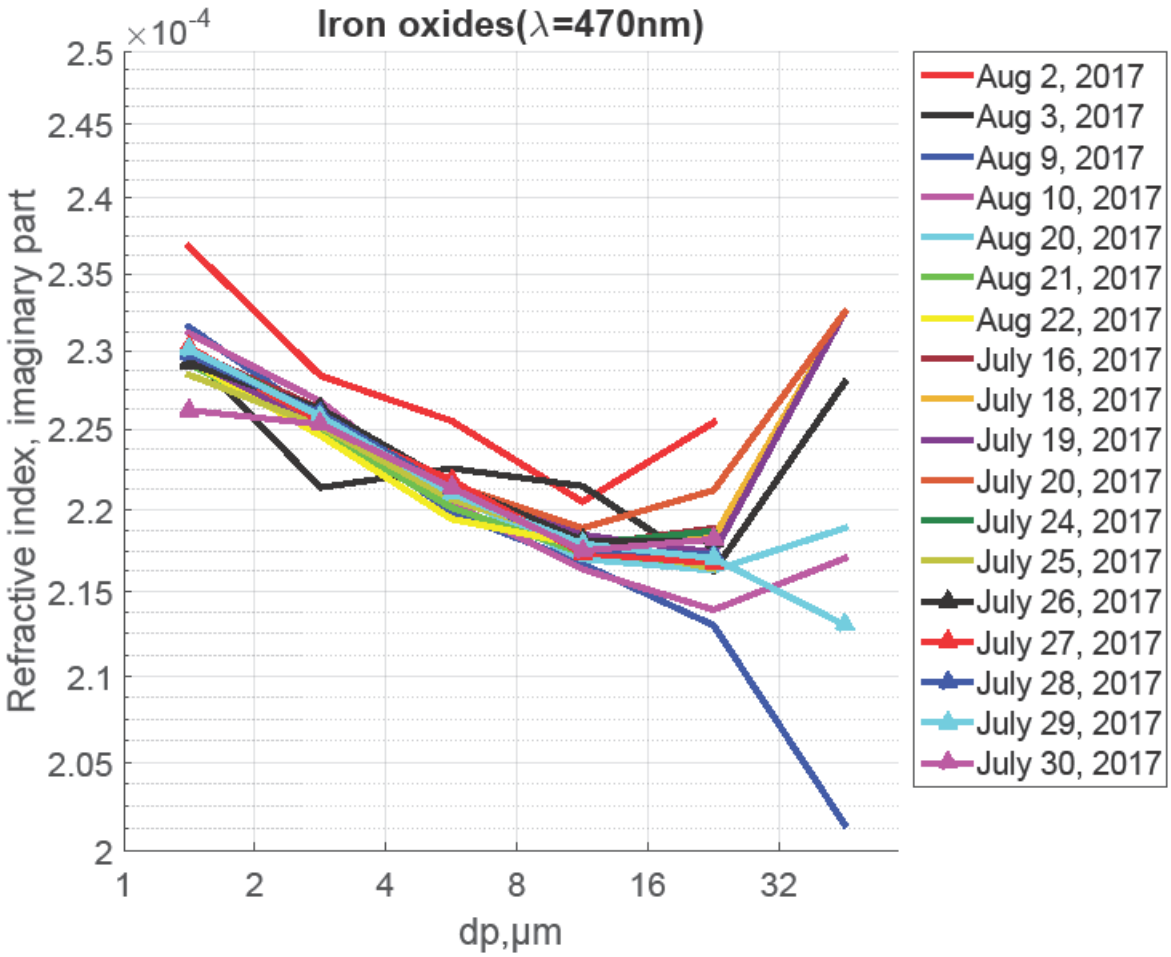

Figure A 3: Average complex refractive index (**imaginary part**) analyzed over different days (at wavelength=470 nm).

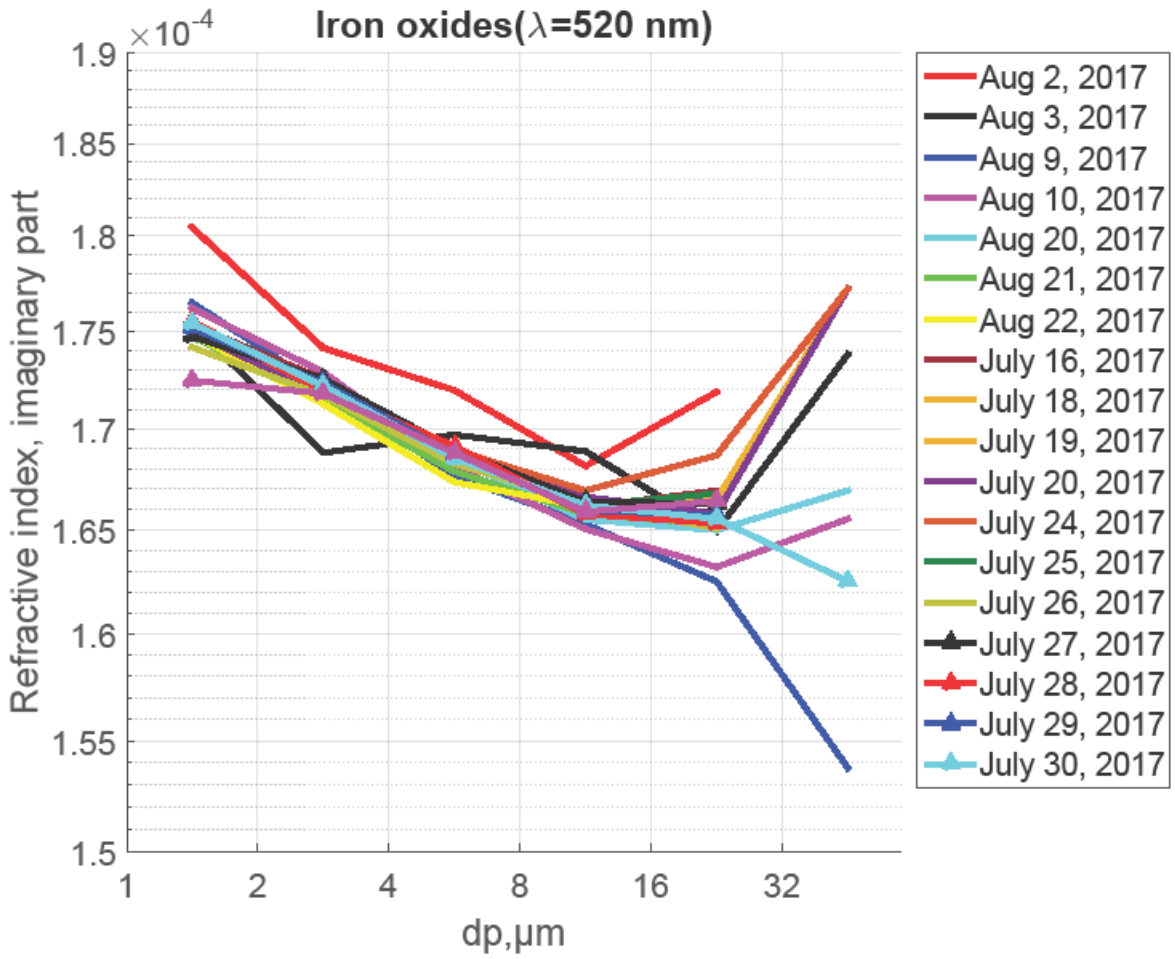

Figure A 4: Average complex refractive index (**imaginary part**) analyzed over different days (at wavelength=520 nm).

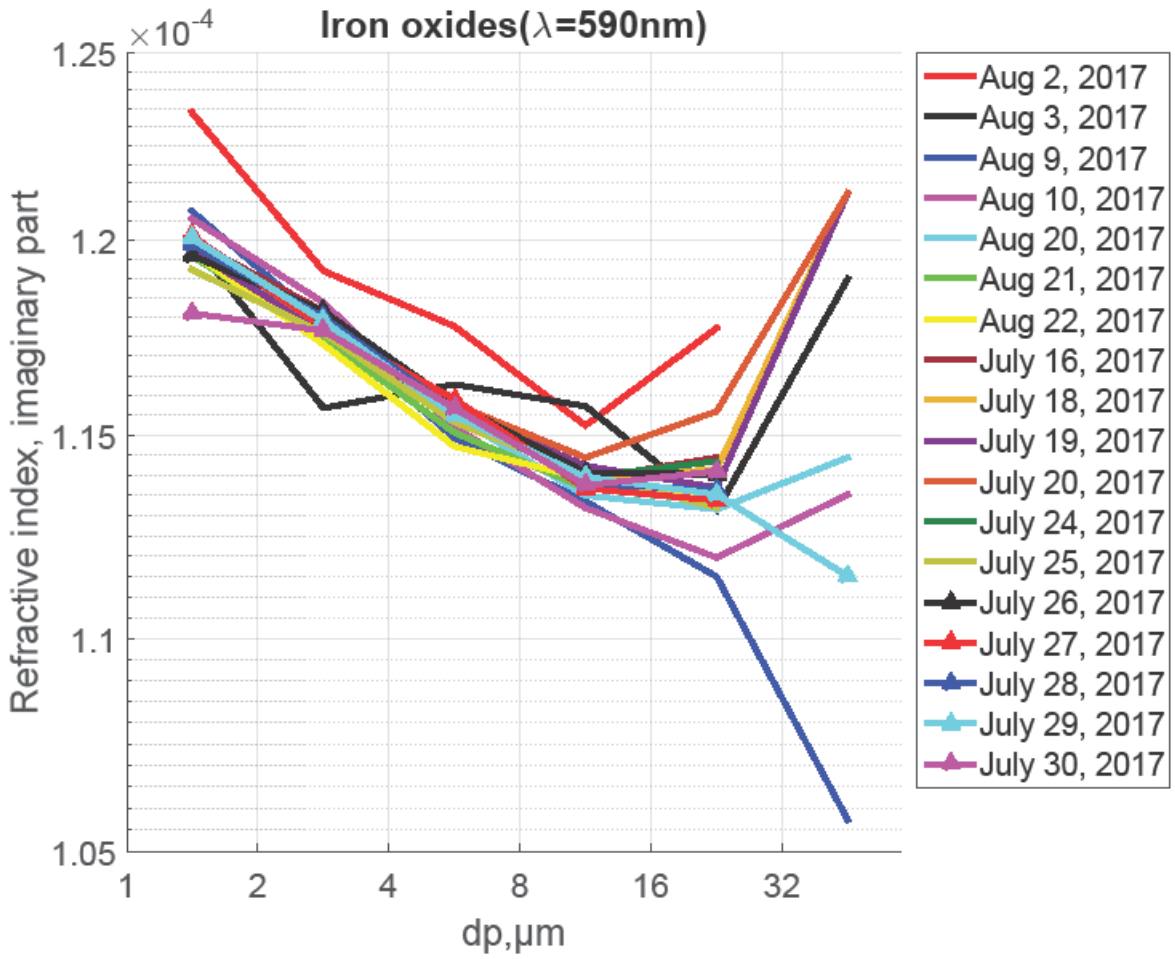

Figure A 5: Average complex refractive index (**imaginary part**) analyzed over different days (at wavelength=590 nm).

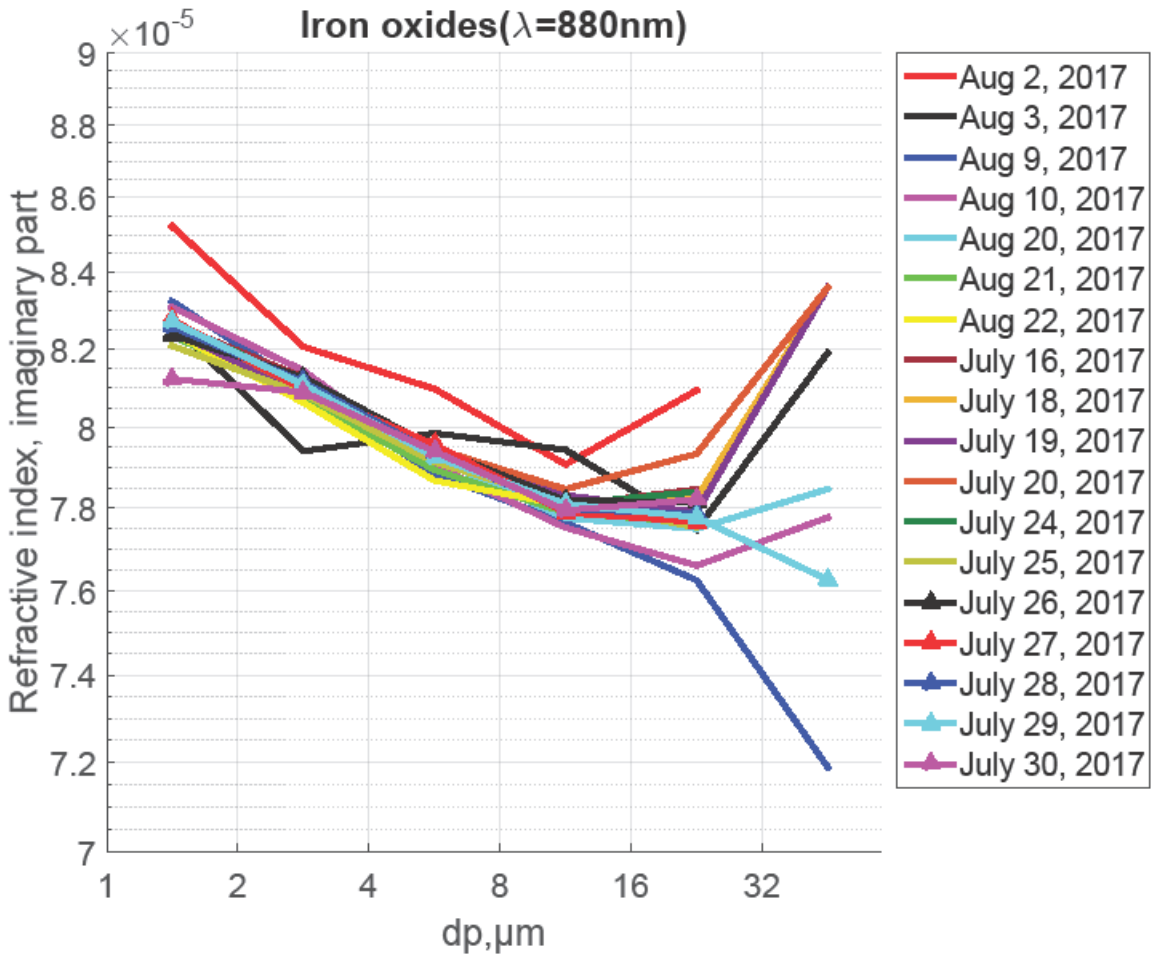

Figure A 6: Average complex refractive index (**imaginary part**) analyzed over different days (at wavelength=880 nm).

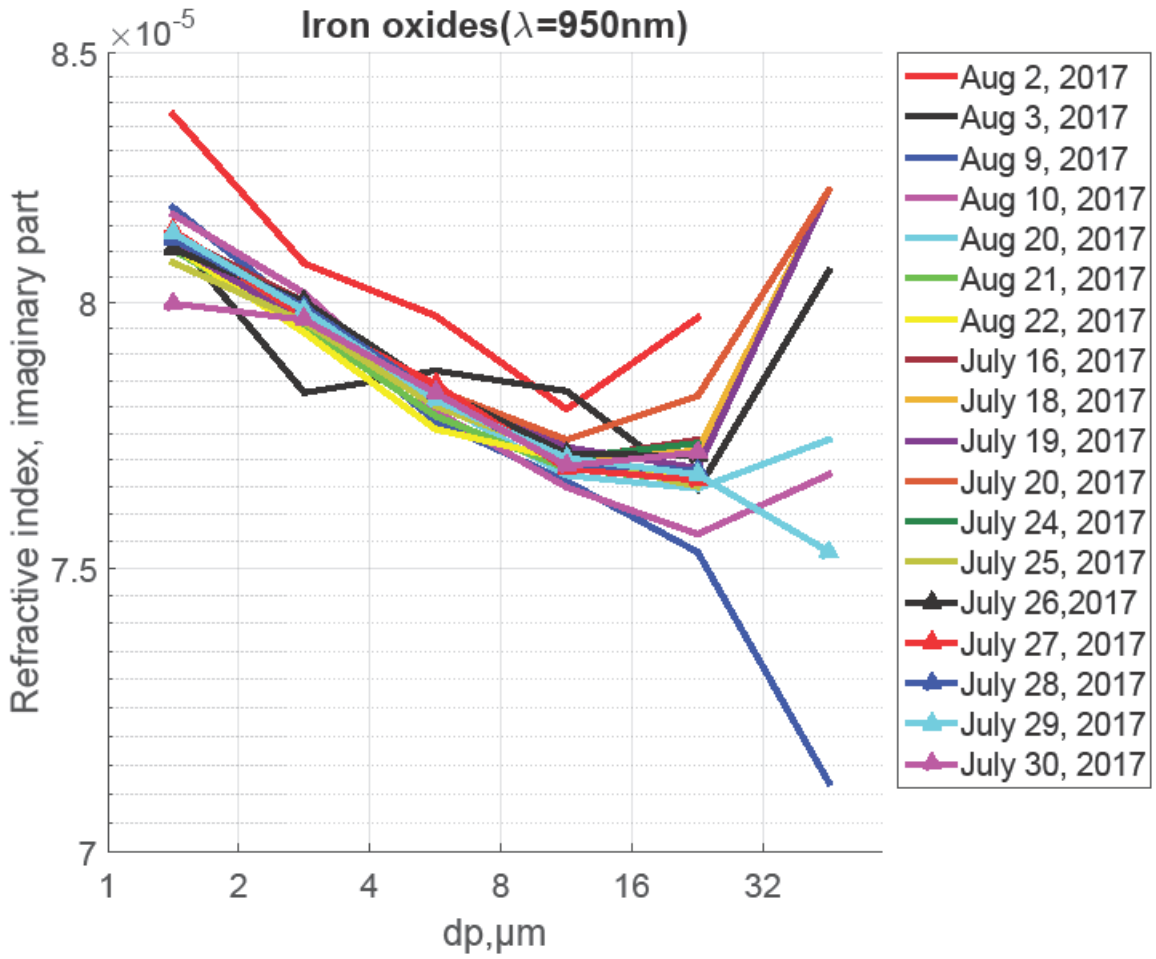

Figure A 7: Average complex refractive index (**imaginary part**) analyzed over different days (at wavelength=950 nm).

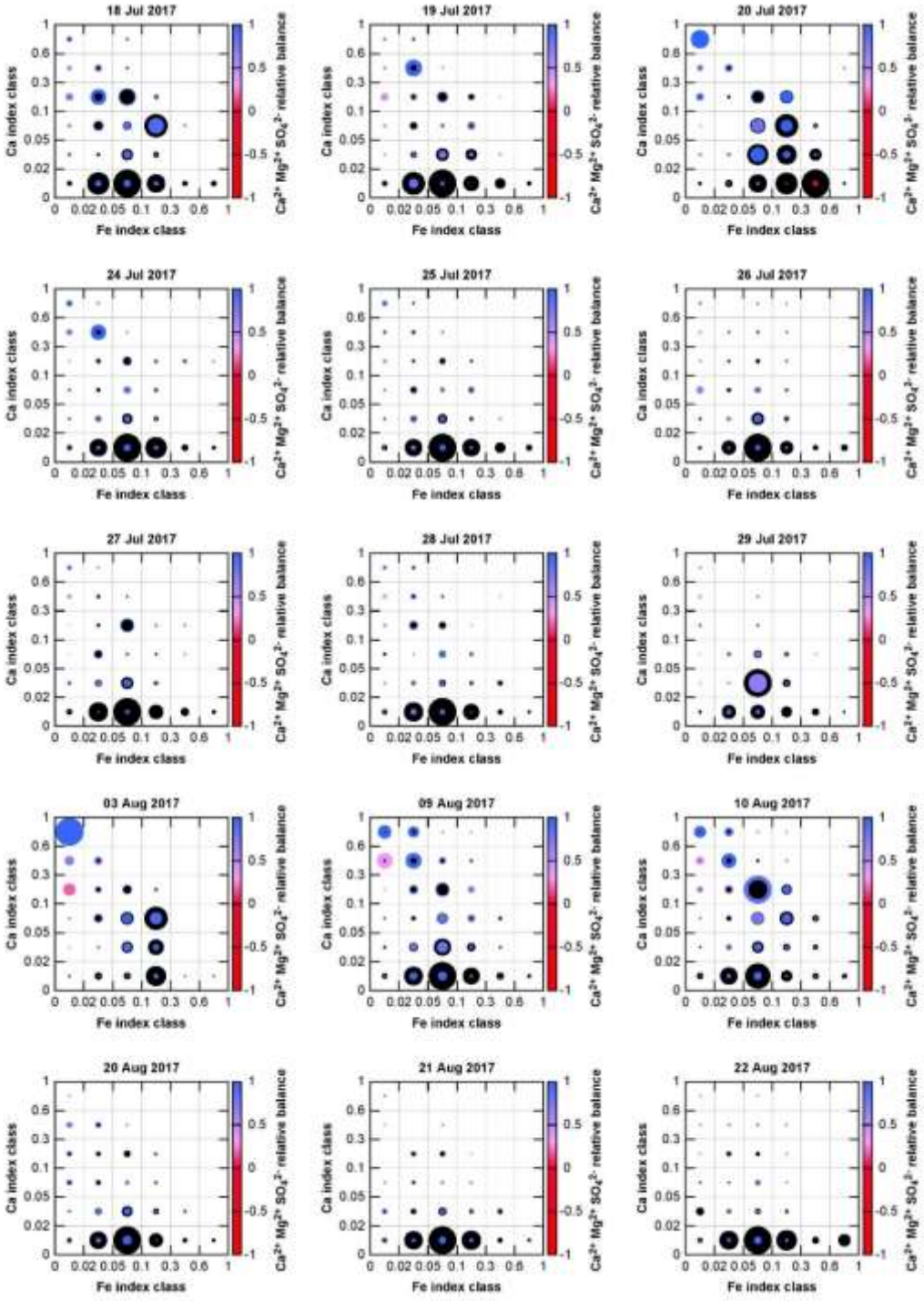

Figure A 8: Mixing state of iron (black circles) and calcium (colored circles) as functions of Ca and Fe indices (colored according to the aerosol Ca^{2+} Mg^{2+} SO_4^{2-} relative balance) shown for different sampling days. The circle area is proportional to total iron or calcium mass found in each class, normalized to the highest mass for each sampling location. The blue-red transition shows the average relative ion balance of Ca^{2+} + Mg^{2+} versus SO_4^{2-}, indicating an atmospheric processing.